Huazhong Normal University

Wuhan, CHINA

Transverse Azimuthal Anisotropy and Longitudinal Property of Charge Balance Function in Relativistic Heavy Ion Collisions

A dissertation submitted

for the degree of

Doctor of Physics in Institutee of Particle Physics

by

Na Li

Co-supervisors: Aihong Tang, Yuanfang Wu and Nu Xu

3

Table of Contents

CHAPTER 1

Introduction

Scientists always work on finding the most fundamental bricks building up the world. The Standard Model of particle physics is a theory of the fundamental interactions and the elementary particles that take part in these interactions. In the Standard Model, as shown in Figure 1.1, the quarks, leptons are elementary particles which make up all visible matter in the universe while particles transmit forces among each other by exchanging gauge bosons.

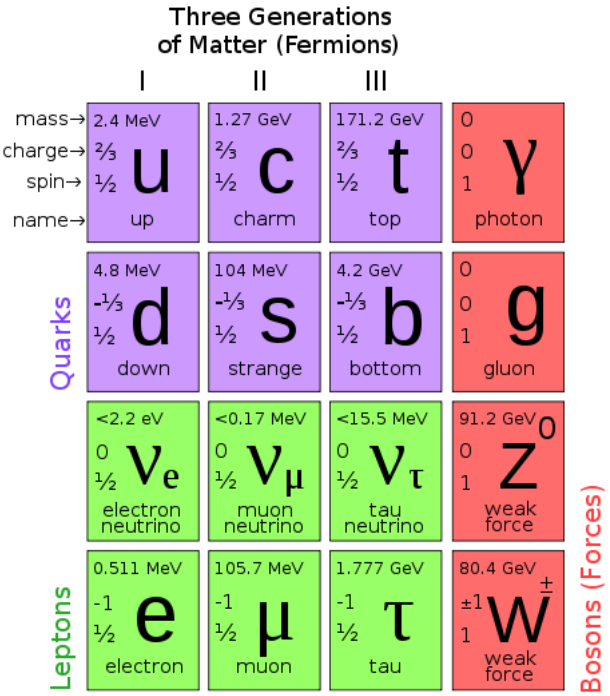

Figure 1.1: The Standard Model of elementary particles, with the gauge bosons in the rightmost column.

Quantum ChromoDynamics (QCD) [?] is an important part of the Standard Model of particle physics. It is a theory of the strong interaction (color force), a fundamental

force describing the interactions of the quarks and gluons making up hadrons. Different from Quantum ElectroDynamics (QED) - the gauge theory describing electromagnetic interaction, QCD is based on the non-Abelian gauge group SU(3), with gauge bosons (color octet gluons), and hence the gluons could have self-interacting. This results in a negative β-function and asymptotic freedom at high energies and strong interactions at low energies.

There are two peculiar properties in QCD theory: 1) asymptotic freedom and 2) confinement. Asymptotic freedom means in very high-energy reactions, quarks and gluons interact very weakly. We use the effective QCD coupling constant α_s to describe the strength of interaction. The $\alpha_s = g_s^2/4\pi$ is dependent on the renormalization scale [**?**], and can be written as:

$$\alpha_s(\mu) \approx \frac{4\pi}{\beta_0 \ln(\mu^2/\Lambda^2_{\rm QCD})}, \tag{1.1}$$

where β_0 is a constant dependent on the number of quarks with mass less than μ and $\Lambda_{\rm QCD}$ is one of the important QCD parameters.

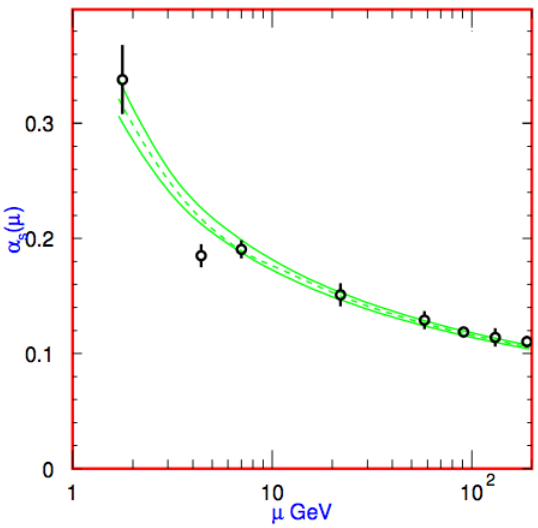

Figure 1.2: QCD effective coupling α_s as a function of momentum transfer scale μ. The figure is taken from [**?**].

Figure 1.2 shows α_s at different momentum transfer scale [**?**]. From the plot we can see that the coupling constant decreases with increasing energy which means that the strong force between quarks becomes weaker at larger distances when they are separated.

$\alpha_s \to 0$ as $\mu \to \infty$ and QCD becomes strongly coupled at $\mu \sim \Lambda_{\rm QCD}$. The α_s has to be determined from experiment. The world average α_s at common energy scale $\mu = M_Z$ is $\alpha_s(M_Z) = 0.1176 \pm 0.002$ [**?**], and the QCD scale $\Lambda_{\rm QCD} \sim 200$ MeV.

QCD is formulated in terms of quarks and gluons while the experimentally observed states are hadrons. As mentioned previously, the method of perturbation QCD (pQCD) theory is appropriate in the high-momentum scale, short-distance regime in principal. At the strong coupling case, pQCD is irrelevant and some other methods are needed, e.g., Lattice QCD [**?**].

Confinement means that there is force between quarks as they are separated. The confinement properties can be described by potential:

$$V_0(r) \sim \sigma r, \tag{1.2}$$

where r is the separation between quarks and the string tension σ measures the energy per unit separation distance. At sufficiently high density, we expect color screening to set in and the potential Eq. 1.2 becomes

$$V(r) \simeq \sigma r[\frac{1-\exp(-\mu r)}{\mu r}], \tag{1.3}$$

where μ is the color screening mass [**?**].

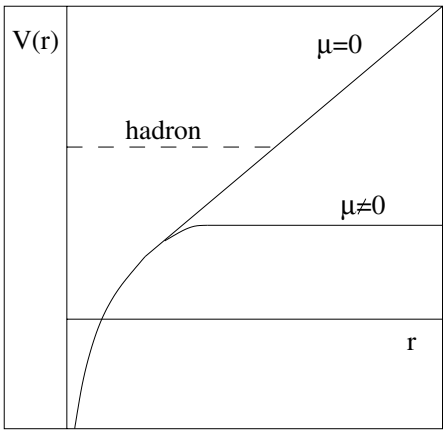

Figure 1.3: Color screening of confining potential. The calculations are from [**?**].

The potential between quarks is also depends on the temperature. The Figure 1.3 shows the potential as a function of r for different temperature. At low temperature,

the potential increases linearly with the distance between quarks, which means that the quarks are bounded within the hadrons. When the temperature is higher than the confined temperature, the confinement potential is "melted", then quarks are free. So far we have never observed a so called deconfined quark which means the quark can move in a volume much larger than the volume of a hadron.

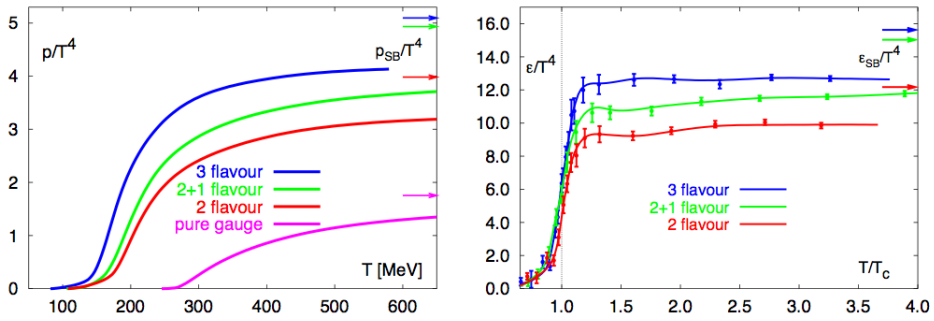

Figure 1.4: Lattice QCD calculation results for the pressure (left) and energy density (right) divided by T^4 of strongly interacting matter as a function of temperature. The calculations are from [**?**]

Recent advances in the formulation of thermodynamical lattice QCD at finite temperature and density however, suggests that when sufficiently high temperature and density are reached, quarks become effectively deconfined. Figure 1.4 shows the pressure and the energy density scaled by T^4 (where T is the system temperature). Both variables rise as T increases. The magnitude of ε/T^4 reflects the number of degrees of freedom in the thermodynamic system, and it quickly increases at a critical temperature T_c. The rise corresponds to a transition in the system to a state where the quarks and gluons have become relevant degrees of freedom. The pressure changes relatively slowly compared to the increase of the energy density, and it means that the pressure gradient in the system is significant reduced during the phase transition.

A Quark-Gluon Plasma (QGP) is a phase of QCD which exists at extremely high temperature and/or density. Figure 1.5 shows a schematic QCD phase diagram. The behavior of nuclear matter, as a function of temperature and baryon density, is governed by its equation of state (EOS). Conventional nuclear physics focuses on the lower left portion of the diagram at low temperature and near normal nuclear matter density. It is

predicted that a hadron-quark phase transition will occur if the temperature or baryon density is high enough. The QGP phase is believed to exist in the first few microseconds after the Big Bang (the high temperature case) and possibly exist in the cores of heavy neutron stars (the high density case).

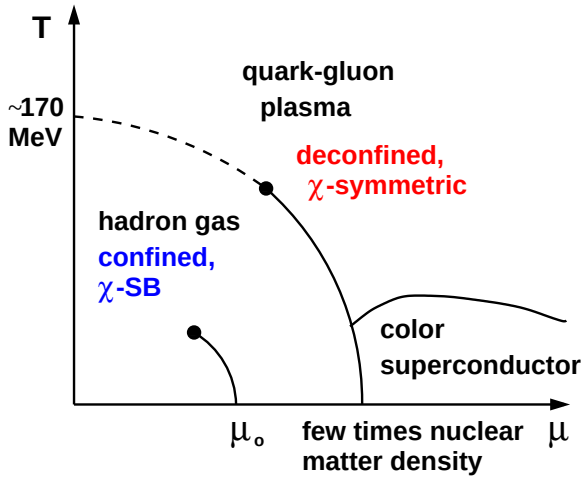

Figure 1.5: Sketch of the QCD phase diagram. The figure is from [**?**]

The goal of heavy ion physics is to create the condition which may lead to the formation of the QGP and study the property of the new kind of nuclear matter and also try to explore the phase transition and map the phase diagram.

CHAPTER 2

Relativistic Heavy Ion Collisions

The main goal of building the Relativistic Heavy Ion Collider (RHIC) in Brookhaven National Laboratory (BNL) is to create a condition with extreme high temperature and density which may lead to the matter of deconfined quarks and gluons. The new form of matter created in the laboratory is believed to exist at very early stage of universe evolution. Studying QGP formation will help us to understand the fundamental structure of the matter and evolution of our universe.

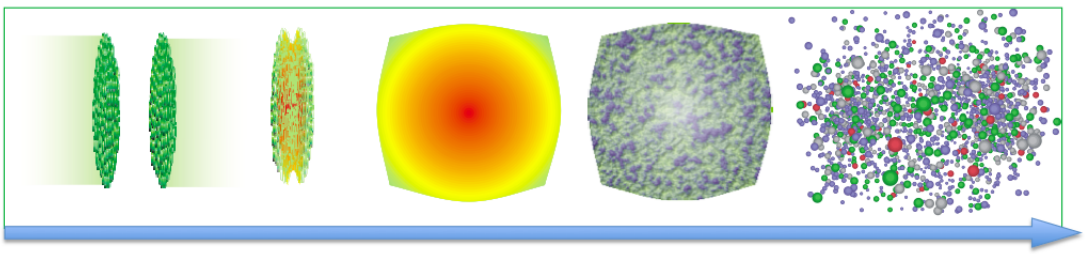

Figure 2.1: A schematic picture of the evolution of a relativistic heavy ion collision.

The evolution of a relativistic heavy-ion collision is shown schematically in Figure 2.1. The two nuclei can be described as two thin disks due to the Lorentz contraction when they are approaching each other at near the speed of light. At the collision, protons and neutrons in the overlapping region of two nuclei experience strong multiple scattering and the longitudinal kinetic energy is transformed into the local energy concentrated at the collision point with extremely high temperature. Nucleons will dissolve at such an high temperature and quarks and gluons are deconfined. The strong interactions between quarks and gluons are expected to be sufficient to lead to local thermal and chemical equilibrium after a very short time, and then the QGP is formed. At this stage the partonic scatterings with high momentum transfer are dominant and high

energy leptons and jets are created, such as $q\bar{q}$ pairs, gluons and direct photons. As the system expands rapidly and cools down, mesons and baryons start to be created by fragmentation and quark coalescence. The fireball then reaches chemical freeze-out, evolving into an strongly interacting hadronic gas. After that, the system reaches kinetic freeze-out and particles stop interacting with each other and the collision ends at this point. The freeze-out hadrons move freely till they reach the detectors.

It is hard to determine whether the QGP is produced directly since its lift time is too short. Experimentally it is studied by looking at the information provided by the particles that shower out from the collision.

2.1 Experimental observations

The QGP state formed in nuclear collisions is a transient rearrangement of the correlations among quarks and gluons. Heavy ion collisions at relativistic energies offer a unique environment for the creation and study of the QGP phase in laboratory. Lots of probes have been proposed [**?**, **?**] to study the novel state of matter for experimental aspects. QGP is taken to be a (locally) thermalized state of matter in which quarks and gluons are deconfined, so that color degrees of freedom become manifest over the nuclear, rather than merely nucleonic , volumes. The thermalization and deconfinement are the two experimental concentrations to claim QGP formation. In this section, we review some experimental probes and results.

2.1.1 Hard probes

In relativistic heavy ion collisions, the high p_T particles is believed produced from hard scattering processes, and by parton fragmentation. The interaction of the hard partons (jet) with the medium can provide a class of unique, penetrating probes. The hard partons (jets) will interact with the medium and thus suffer energy lose. The amount of the energy loss should reflect the gluon density of the medium. The softened partons fragmenting into hadrons will lead to the suppression of high p_T hadrons in the final

state compared to that of no medium effects ($p + p$ collisions). This effect is so called jet quenching.

Left panel in Fig. 2.2 shows the azimuthal distribution of hadrons with $p_T > 2$ GeV/c relative to a trigger hadron ($p_T^{\rm trigg} > 4$ GeV/c). A hadron pair from a single jet will generate the near-side correlation T ($\Delta\phi \approx 0$) as observed in $p + p$, d + Au and Au + Au collisions. A hadron pair from back-to-back di-jets will generate the away-side correlation ($\Delta\phi \approx \pi$) as observed in $p + p$ and d + Au collisions. The significant disappearance of back-to-back correlation is observed in central Au + Au collisions.

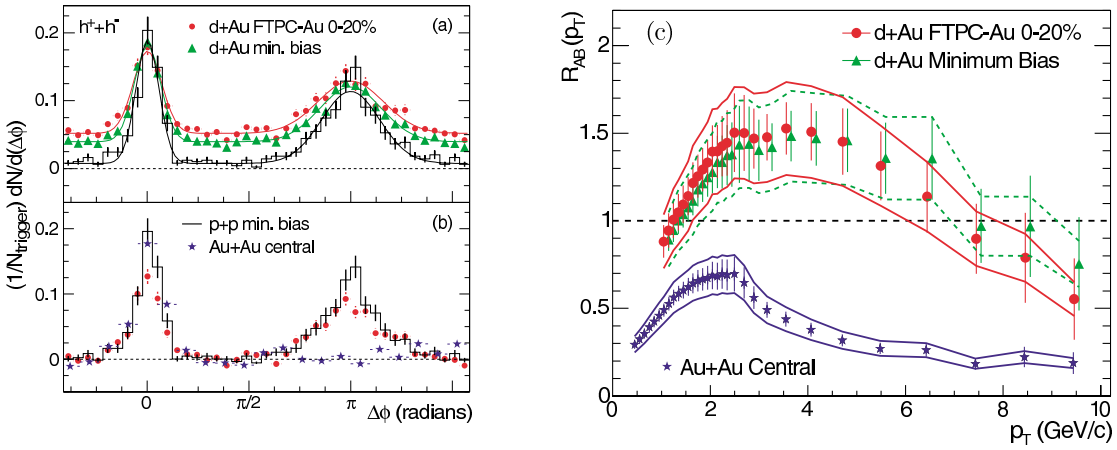

Figure 2.2: (a) Efficiency corrected two-particle azimuthal distributions for minimum bias and central d + Au collisions, and for $p + p$ collisions. (b) Comparison of two-particle azimuthal distributions for central d + Au collisions to those seen in $p + p$ and Au + Au collisions. The respective pedestals have been subtracted. (c) $R_{AB}(p_T)$ for minimum bias and central d+Au collisions, and central Au + Au collisions. The bands show the normalization uncertainties, which are highly correlated point-to-point and between the two d + Au distributions. The plot is from [**?**].

Modifications of high p_T particle production in nuclear collisions, A + B, with respect to p+p interactions are given by the nuclear modification factor defined by:

$$R_{AB}(p_T) = \frac{d^2\sigma_{AB}/dp_T d\eta}{< N_{\rm bin} > d^2\sigma_{pp}/dp_T d\eta}, \tag{2.1}$$

where $d^2\sigma_{pp}/dp_T d\eta$ is the inclusive cross section measured in p+p collisions and $< N_{\rm bin} >$ accounts for the geometrical scaling from $p + p$ to nuclear collisions as described by the Glauber model. If an Au + Au collision is an incoherent superposition of p+p collisions,

the ratio would be unity. Nuclear effects such as energy loss and shadowing will reduce the ratio below unity while anti-shadowing and the Cronin effect lead to a value about unity. The Cronin effect, an enhancement of the particle yield at intermediate p_T, is usually attributed to multiple soft parton scatterings before a hard interaction of the parton (p_T broadening). The shadowing of the structure function modifies the particle yield depending on the parton momentum fraction, $x_{\rm Bj}$, probed in the partonic scattering. An alternative model of the initial state of a nucleus is the gluon saturation or color glass condensate(CGC) in which the gluon population at low $x_{\rm Bj}$ is limited by non-linear gluon-gluon dynamics. Initial state and final state nuclear effects in Au + Au collisions can be isolated through studies of d + Au collisions. Figure 2.2 shows R_{AB} for charged particles in d + Au and central Au + Au collisions. An enhancement is observed in d + Au collisions instead of suppression. Therefore, the suppression in Au + Au is due to final state effect and indicates that a dense medium is created in central Au+Au collisions.

In addition to the nuclear modification factor, R_{AB}, dihadron azimuthal correlations can be used to study the effect of jet quenching. The azimuthal correlations of two high p_T particles from jets are expected to show a narrow near-side correlation and a broader away-side correlation. However, in the case of strong jet quenching the away-side jet would be suppressed by energy loss in the traversed medium. Figure 2.2(c) shows the azimuthal correlations of high p_T particles with 2 GeV/c $< p_T <$ $p_T^{\rm trig}$ relative to the trigger particle with $4 < p_T < 6$ GeV/c in p + p, d + Au and Au+Au collisions. The near-side and away-side peaks are clearly visible in p + p, minimum bias and central d+Au collisions. In central Au+Au collisions, a similar near-side peak appears while the away-side peak has disappeared. The suppression only occurs in Au+Au collisions and shows that this is a final state effect as expect from partonic energy loss mechanisms.

These results provide experimental evidence that the hot and dense medium has bee formed at RHIC.

2.1.2 Collective flow

The Flow refers to a collective expansion of the bulk matter, arising from the density gradient from the center to the boundary of the created fireball in nuclear collisions. Interactions among constituents push matter outwards; frequent interactions lead to a common constituent velocity distribution. This so-called collective flow is therefore sensitive to the strength of the interactions. Collective flow is additive and thus accumulated over the whole system evolution, making it potentially sensitive to the equation of state of the expanding matter [?, ?, ?, ?, ?, ?]. At lower energies, the collective flow reflects the properties of dense hadronic matter, while at RHIC energies, a large contribution from the pre-hadronic phase is anticipated.

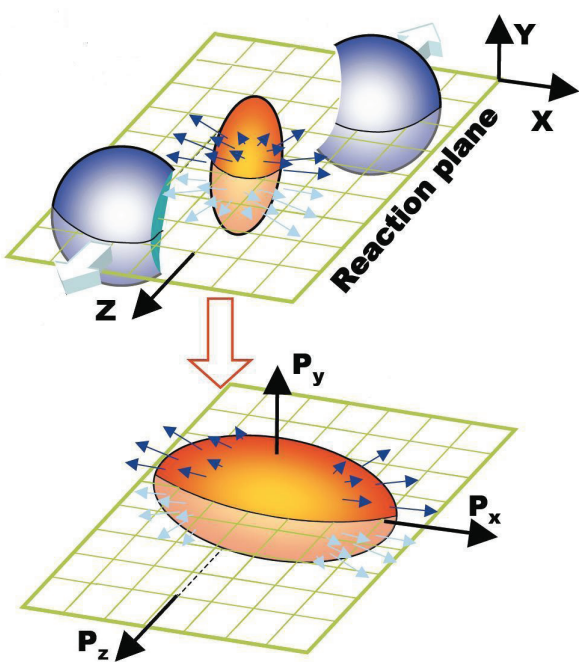

Figure 2.3: Sketch of an almond shaped fireball, where z direction is the beam direction and x is the direction of impact parameter b.

In heavy ion collisions, the size and the shape of the colliding region depend on the distance between the centers of the nuclei in the transverse plane (impact parameter b). The plane defined by the beam direction and the impact parameter is called the reaction plane ($x - z$ plane in Fig.2.4).

In non-central collisions, the overlapping reaction zone of two colliding nuclei is not spherical (shown in Fig.2.3). Their overlap area in the transverse plane has a short axis, parallel to the impact parameter, and a long axis perpendicular to it. This almond shape of the initial profile is converted by the pressure gradient into a momentum asymmetry, so that more particles are emitted along the short axis [**?**], see Figure 2.3. The spatial anisotropy is largest in the early evolution of the collision. As the system expands it becomes more spherical, thus this driving force quenches itself. Therefore the momentum anisotropy is particularly sensitive to the early stages of the system evolution [**?**]. In addition, because anisotropic flow depends on rescattering, it is sensitive to the degree of thermalization of the system at early time.

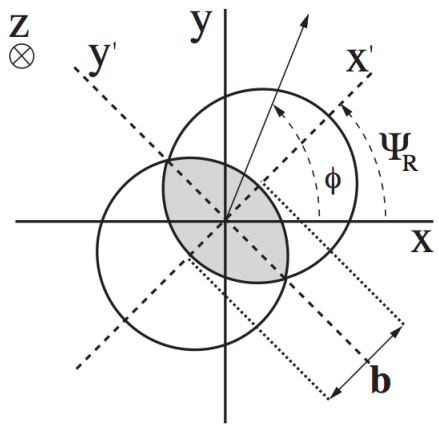

Figure 2.4: Sketch of an almond shaped fireball, where z direction is the beam direction and x is the direction of impact parameter b.

The initial spatial anisotropy in the reaction region can be characterized by the eccentricity defined as:

$$\varepsilon_{\mathrm{std}} = \frac{\langle y^2 - x^2 \rangle}{\langle y^2 + x^2 \rangle}, \tag{2.2}$$

where x and y are the spatial coordinates in overlapping region as shown in Figure 2.4. However even at fixed impact parameter, the number of individual nucleons participating in the collision as well as their positions in the transverse plane could fluctuate from event to event. As a consequence, the center of the overlap zone can be shifted and the orientation of the principal axes of the interaction zone can be rotated with respect to the conventional coordinate system. To correct this effect, the participant eccentricity

$\varepsilon_{\rm part}$ is defined as:

$$\varepsilon_{\rm part} = \frac{\langle y'^2 - x'^2 \rangle}{\langle y'^2 + x'^2 \rangle}, \tag{2.3}$$

where the eccentricity is calculated relative to the new coordinate system defined by the major axis of the initial system.

The average values of $\varepsilon_{\rm std}$ and $\varepsilon_{\rm part}$ are rather similar for all but the most peripheral collisions for interactions of heavy nuclei like Au + Au. For smaller systems, however, fluctuations in the nucleon positions become quite important for all centralities and the average eccentricity can vary significantly depending on how it is calculated [**?**].

The anisotropy in momentum space can be studied by the Fourier expansion of azimuthal angle distribution of produced particles with respect to the reaction plane [**?**, **?**, **?**]:

$$E\frac{d^3N}{d^3p} = \frac{1}{2\pi}\frac{d^2N}{p_T dp_T dy}(1 + \sum_{n=1}^{\infty} 2v_n \cos[n(\phi - \Psi_r)]), \tag{2.4}$$

where p_T and y are the transverse momentum and rapidity of a particle, ϕ is its azimuthal angle, v_n is the $n^{\rm th}$ harmonic coefficient and Ψ_r is the azimuthal angle of the reaction plane in the laboratory frame (see Fig. 2.4 for the definition of the coordinate system). The different harmonic coefficients represent different aspects of the global flow behavior. v_1 is so called directed flow and v_2 is so called elliptic flow since it is the largest component characterizing the ellipse shape of the azimuthal anisotropy, while v_4 is the $4^{\rm th}$ harmonic.

Elliptic flow, v_2, is the second harmonic coefficient in the description of particles azimuthal distribution w.r.t. the reaction plane by Fourier expansion. It is argued that the centrality dependence of v_2 can be used to probe local thermodynamic equilibrium [**?**] and might provide a indication of the phase transition [**?**]. It gains a lot of interests [**?**, **?**] in heavy ion collisions.

Figure 2.5 shows the measured v_2 distribution from minimum bias data as a function of p_T in Au + Au collisions at $\sqrt{s_{NN}}$ = 200 GeV from STAR and PHENIX experiments [**?**, **?**]. Identified particle v_2 are shown for $\pi^{\pm}$, K^0_S, p ($\bar{p}$) and Λ ($\bar{\Lambda}$). Up to 1.6 GeV/c, at a given p_T , the heavier particle has the smaller v_2 than the lighter particle. This characteristic mass-ordering is predicted by the hydrodynamic calculationi [**?**, **?**, **?**] represented by the dot-dashed lines. This indicates the collectivity has been developed

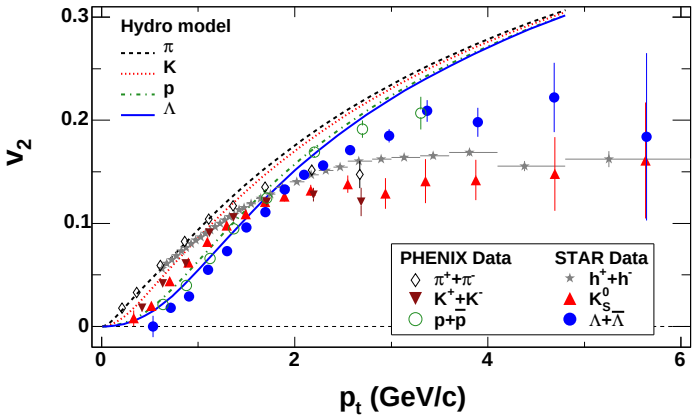

Figure 2.5: v_2 as a function of p_T for $h^{\pm}$ (stars), $\pi^{\pm}$ (diamonds), p ($\bar{p}$) (circles), K^0_S (triangles) and Λ ($\bar{\Lambda}$) (inverse triangles) in Au + Au minimum bias collisions at 200 GeV. Hydro calculations are shown as different curves. The figure is from [**?**].

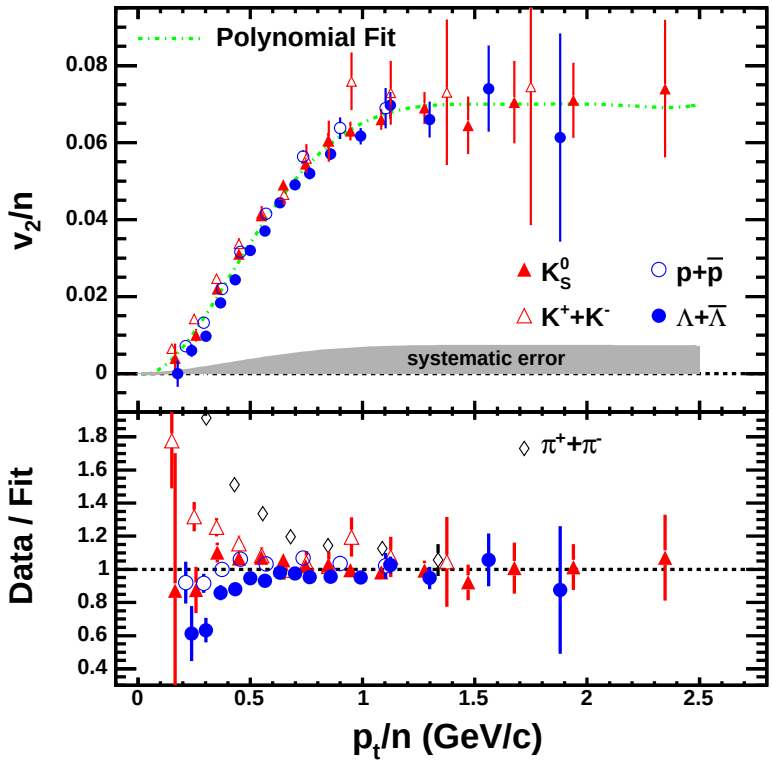

Figure 2.6: Number of quark (n_q) scaled v_2 as a function of scaled p_T for $\pi^{\pm}$ (diamonds), p ($\bar{p}$) (circles), K^0_S (triangles) and Λ ($\bar{\Lambda}$) (inverse triangles). All data are from 200 GeV Au+Au minimum bias collisions. The figure is from [**?**].

at RHIC. In this hydrodynamic calculation, the critical temperature is 165 MeV and the freeze-out temperature is 130 MeV. The absolute magnitude of v_2 is well produced as the parameters of the hydrodynamics calculations have been tuned to achieve good agreement with data. In particular, since the parameters are tuned for zero impact parameter while data is measured for minimum bias, the comparison for v_2 between the theory and the experiment should test hydrodynamical calculations as a function of centrality. This is especially a critical test in assessing QGP claims since the hydrodynamical calculations assume local thermalization while the system is most likely to reach thermalization in central collisions.

A particle type (baryon versus meson) difference in $v_2(p_T)$ was observed for $\pi^{\pm}$, p ($\bar{p}$), K^0_S and Λ ($\bar{\Lambda}$) at the intermediate p_T region. This particle type dependence of the $v_2(p_T)$ is naturally accounted for by quark coalescence or recombination models [**?**, **?**, **?**, **?**]. In these hadronization models, hadrons are formed dominantly by coalescing massive quarks from a partonic system with the underlying assumption of collectivity among these quarks. Should there be no difference in collectivity among u-, d-, and s-quarks near hadronization, these models predict a universal scaling of v_2 and the hadron transverse momentum p_T with the number of constituent quarks (n_q). This scaling has previously been observed to hold within experimental uncertainties for the K^0_S and the Λ when $p_T/n_q \geq 0.7$ GeV/c. Figure 2.6 (top panel) shows v_2 vs. p_T for the identified particle data of Figure 2.5, where v_2 and p_T have been scaled by the number of constituent quarks (n). A polynomial function has been fit to the shown scaled values. To investigate the quality of agreement between particle species, the data from the top panel are scaled by the fitted polynomial function and plotted in the bottom panel. For $p_T/n > 0.6$ GeV/c, the scaled v_2 of $\pi^{\pm}$, p ($\bar{p}$), K^0_S, Λ ($\bar{\Lambda}$) lie on a universal curve within statistical errors. The pion points, however, deviate significantly from this curve even above 0.6 GeV/c. This deviation may be caused by the contribution of pions from resonance decays. Alternatively, it may reflect the difficulty of a constituent-quark-coalescence model to describe the production of pions whose masses are significantly smaller than the assumed constituent-quark masses.

In the low density limit, the mean free path λ is comparable or larger than the

system size, and the integrated elliptic flow is proportional to the spatial anisotropy and the number of rescatterings in the transverse plane:

$$v_2 \propto \varepsilon \frac{1}{S}\frac{dN}{dy}, \tag{2.5}$$

where dN/dy is the multiplicity density and $S = \pi\sqrt{\langle x^2\rangle\langle y^2\rangle}$ is a measure of the initial transverse size of the collision region. The brackets $\langle\cdots\rangle$ denotes an average weighted with the initial density. Since in the hydro limit, where complete thermalization is expected, the centrality dependence of v_2 is mostly defined by the elliptic anisotropy of the overlapping region of the colliding nuclei, e.g., eccentricity, while v_2 is proportional to eccentricity and the multiplicity in the low density limit. The eccentricity increases while the multiplicity decreases with increasing impact parameter respectively, thus the integrated elliptic flow has its maximum at an intermediate impact parameter.

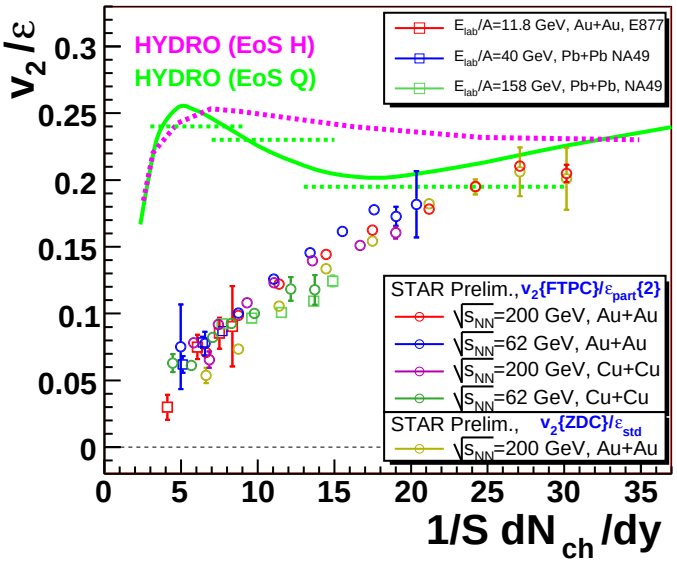

Figure 2.7: Charge particle v_2/ε versus $\frac{1}{S}dN_{\rm ch}/dy$ from AGS, SPS to RHIC energies. The figure is from [**?**].

The elliptic flow increases with the increase of particle density. Eventually, it saturates at the hydrodynamical limit, where the mean free path is much less than the geometrical size of the system and complete thermalization is reached. Therefore v_2/ε is approximately constant though the magnitude does depend on the velocity of sound in

the fluid (and thus on the different contributions from the different phases and the phase transition) [**?**]. Figure 2.7 shows charge particle v_2/ε as a function of $\frac{1}{S}dN_{\rm ch}/dy$, and $\frac{1}{S}dN_{\rm ch}/dy$ is the measured charged particle density in midrapidity. At RHIC energies, STAR measurements are presented for Au+Au and Cu+Cu collisions at both 62.4 GeV and 200 GeV. At SPS energies, NA49 measurements are presented for Pb+Pb collisions at 40A GeV and 158A GeV. At AGS energies, E877 measurements is shown for Au+Au collisions at 11.8A GeV. By dividing v_2 with ε, a correction for the initial geometry of the different centralities is applied. The particle density increases with centrality and increasing beam energy. The values of v_2/ε fall approximately on a single curve, independent of beam energy or impact parameter. The v_2/ε data shown at the full RHIC energy for near central collisions is close to ideal hydro calculations, and it indicates that the system created in heavy ion collisions evolves towards the thermalization.

If, on the other hand, equilibration is incomplete, then eccentricity scaling is broken and v_2/ε also depends on the Knudsen number $K = \lambda/R$, where λ is the length scale over which a parton is deflected by a large angle and R is its transverse size. The centrality dependence of v_2/ε can be described by:

$$\frac{v_2}{\varepsilon} = \frac{v_2^{\rm hydro}}{\varepsilon}\frac{1}{1+K/K_0}, \tag{2.6}$$

v_2/ε is largest in the hydrodynamic limit $K \to 0$. The first order corrections to this limit, corresponding to viscous effects, are linear in K. For a large mean-free path, far from the hydrodynamic limit, $v_2/\varepsilon \sim 1/K$ vanishes like the number of collisions per particle.

Elliptic flow develops gradually during the early stages of the collision. Because of the strong longitudinal expansion, the thermodynamic properties of the medium depend on the time τ. The average particle density, for instance, decreases like $1/\tau$ [**?**].

$$\rho(\tau) = \frac{1}{\tau S}\frac{dN}{dy}, \tag{2.7}$$

where dN/dy denotes the total (charged + neutral) multiplicity per unit rapidity, and S is the transverse overlap area between the two nuclei. The Knudsen number K is defined by evaluating the mean-free path $\lambda = 1/\sigma\rho$ (σ is a partonic cross section) at $\tau = R/c_s$.

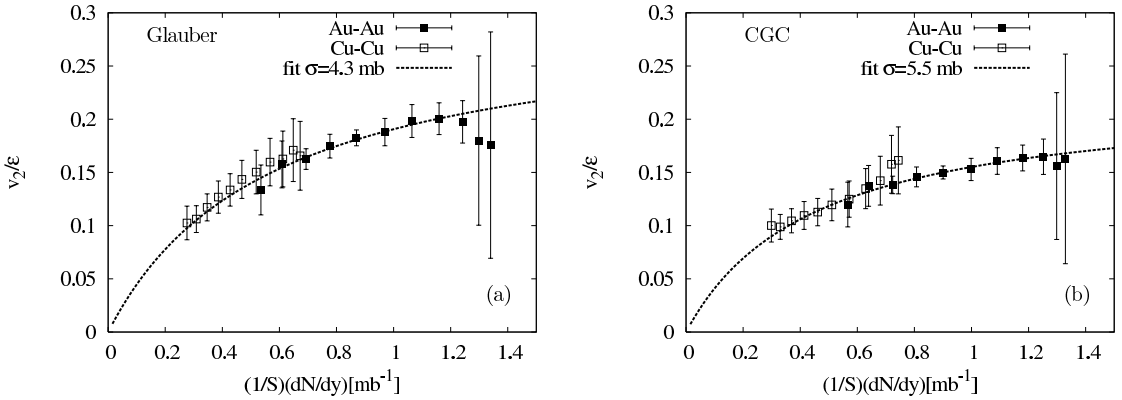

Figure 2.8: Variation of the scaled elliptic flow with the density, assuming initial condition from the (a) Glauber [**?**] model and (b) CGC model. The line is a two-parameter fit using Eq. 2.6 and Eq. 2.8. The figure is from [**?**].

Thus,

$$\frac{1}{K} = \frac{\sigma}{S}\frac{dN}{dy}c_s. \tag{2.8}$$

Figure 2.8 displays v_2/ε as a function of $\frac{1}{S}\frac{dN}{dy}$ for Au+Au and Cu+Cu collisions at various centralities, within the Glauber and CGC approaches, respectively. For both types of initial conditions, the values of the fit parameters clearly depend on the initial conditions, which has important consequences for the physics. The data for the scaled flow shows a saturate trend at high densities to a hydrodynamic limit, the elliptic flow is at least 25% below the (ideal) "hydrodynamic limit", even for the most central Au+Au collisions.

v_4 is the fourth harmonic coefficient in the description of particles azimuthal distribution w.r.t. the reaction plane by Fourier expansion.

It is argued that the azimuthal shape in momentum space is no longer elliptic, but becomes "peanut" shaped with large v_2 value [**?**]. Using STAR high p_T plateau experimental values, this is shown in Figure 2.9. Experimentally we measured the amplitude of v_4 as shown in Figure 2.10 in Au+Au collisions at 200 GeV. v_4 is shown as a function of p_T and the scaled v_2 is also shown for comparison. The experimental v_4 values shown in Fig. 2.10 considerably exceed the value which is predicted in [**?**] to eliminate the peanut waist.

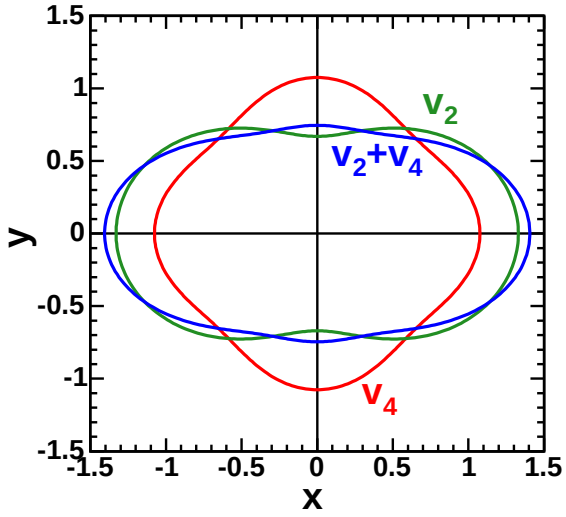

Figure 2.9: A polar graph of the distribution $1 + 2v_2\cos(2\phi) + 2v_4\cos(4\phi)$ where ϕ is the azimuthal angle relative to the positive x axis. Plotted are the distributions for $v_2 = 16.5\%$ showing the waist, $v_4 = 3.8\%$ having a diamond shape, and both coefficients together. The figure is from [**?**].

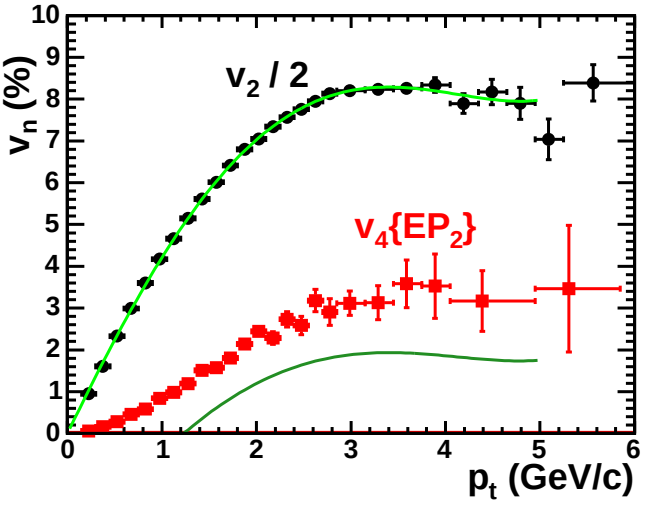

Figure 2.10: v_2 scaled down by a factor of 2, and $v_4\{EP_2\}$ vs. p_T for charged hadrons from minimum bias events. Using a fit to the v_2 values, the lower solid line is the predicted v_4 needed to just remove the "peanut" waist (see text). The figure is from [**?**].

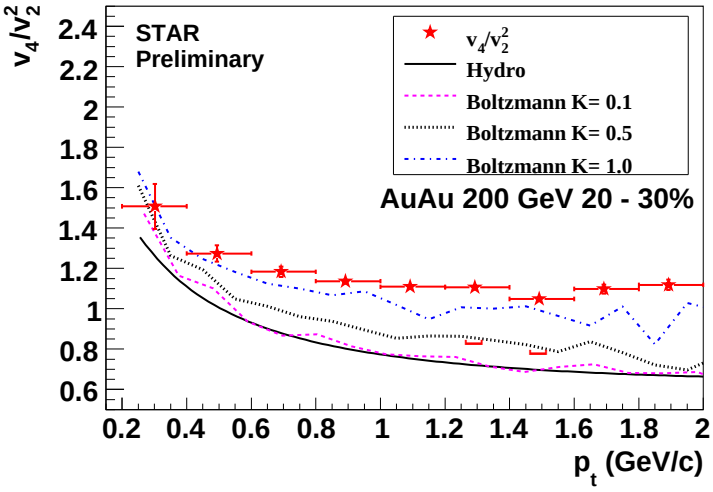

Figure 2.11: The ratio of v_4/v_2^2 versus p_T for charged particles at $|\eta| < 1.3$ in Au+Au collisions at $\sqrt{s_{NN}} = 200$ GeV. The brackets indicate the systematic uncertainty. The curves correspond to two hydrodynamic calculations. The figure is from [**?**].

It's is argued that if the system behaves like ideal hydro, the ratio v_4/v_2^2 will approach to 0.5 at high p_T [**?**]. Figure 2.11 shows the result of STAR data and ideal hydro calculation as a function of transverse momentum. The dashed lines are ratio come out of calculations by solving Boltzmann equations with Monte Carlo simulation, with different Knudsen number K. When the Knudsen number is small, it recovers the hydrodynamic limit as indicated the solid line. The plot shows that the system exhibits significant deviation from ideal hydrodynamic limit ($K \ll 1$), and the data is consistent with a incomplete thermalized system with $K > 0.5$.

2.1.3 Correlations

The observables related to correlations [**?**, **?**, **?**] are considered sensitive to QGP state. The study of correlations is expected to provide us additional information on particle production mechanism in high energy nuclear collisions.

The electric charge balance function (BF) is sensitive to whether the transition to a hadronic phase was delayed, as expected if the quark-gluon phase were to persist for a substantial time [**?**]. It is defined in terms of a combination of four different

conditional densities of charged hadrons. It measures how the net charge at any point of the phase space is rearranged if the charge at a selected point changes. Projected on to the pseudorapidity difference $\delta\eta = \eta_1 - \eta_2$ of two charged particles in a given pseudorapidity window η_w, the BF becomes

$$B(\delta\eta|\eta_{\rm w}) = \frac{1}{2}\left[\frac{n_{+-}(\delta\eta,\eta_{\rm w}) - n_{++}(\delta\eta,\eta_{\rm w})}{< n_{+}(\eta_{\rm w}) >} + \frac{n_{-+}(\delta\eta,\eta_{\rm w}) - n_{--}(\delta\eta,\eta_{\rm w})}{< n_{-}(\eta_{\rm w}) >}\right] \tag{2.9}$$

where $n_{+}(\eta_{\rm w})$ and $n_{-}(\eta_{\rm w})$ are respectively the number of measured positively and negatively charged particles. $n_{+-}(\delta\eta,\eta_{\rm w})$ is the number of pairs of particles with opposite charges separated by pseudorapidity $\delta\eta$.

And the widths of balance function is defined as:

$$< \delta\eta >= \frac{\sum_i B_s(\delta\eta_i)\delta\eta_i}{\sum_i B_s(\delta\eta_i)} \tag{2.10}$$

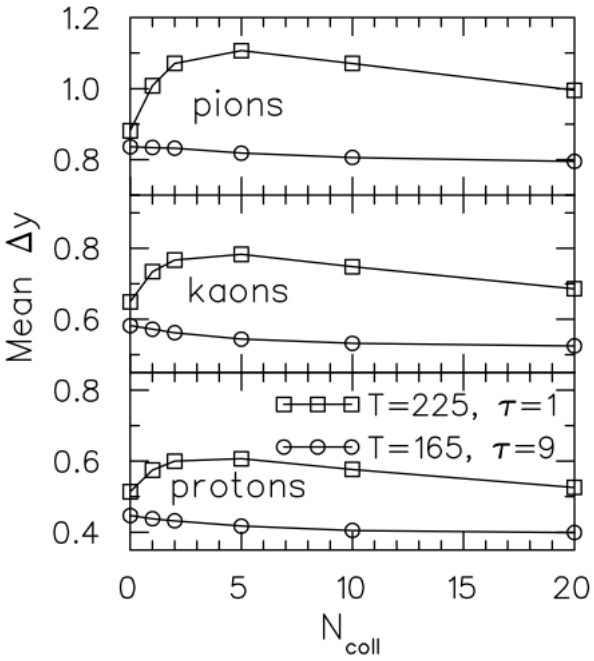

Figure 2.12: The mean width of the balance function displayed as a function of the number of collisions, both for the case where particles are created early ($\tau = 1$ fm/c, $T = 255$ MeV) and late ($\tau = 9$ fm/c, $T = 165$ MeV). The figure is from [**?**].

Due to local charge conservation, when particles and their antiparticles are pair produced, they are correlated initially in coordinate space. If hadronization occurs early,

the members of a charge/anticharge pair would be expected to separate in rapidity due to expansion and rescattering in the strongly interacting medium. Alternatively, delayed hadronization would lead to a stronger correlation in rapidity between the particles of charge/anticharge pairs in the final state. Measuring this correlation involves subtracting uncorrelated charge/anticharge pairs on an event-by-event basis as shown in the Eq. 2.9. The remaining charge/anticharge particle pairs are examined to determine the correlation as a function of the relative rapidity, Δy, between the members of the pairs. Figure 2.12 shows the widths of balance function for the case where particles are created early (squares) and late (circles). It is clear that the balance function is narrower for a scenario with delayed hadronization, and is therefore sensitive to the conjecture that a quark-gluon plasma may be produced.

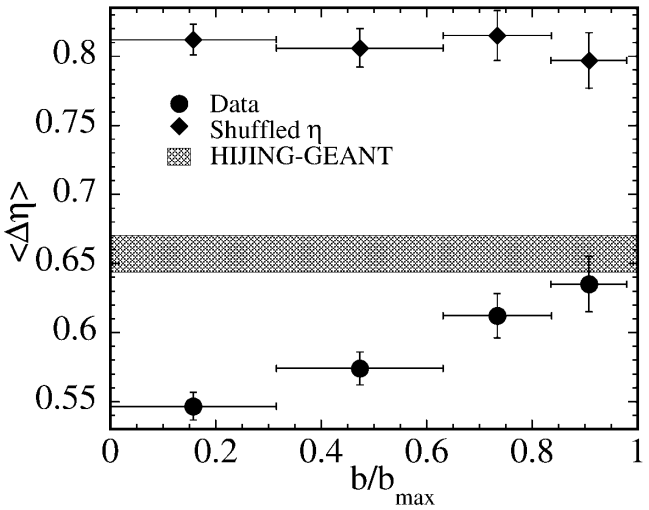

Figure 2.13: The width of balance function for charged particles, $< \Delta\eta >$, as a function of normalized impact parameter ($b/b_{\rm max}$). Error bars shown are statistical. The width of the balance function from HIJING events is shown as a band whose height reflects the statistical uncertainty. Also shown are the widths from the shuffled pseudorapidity events.

The widths of balance function was measured in Au+Au collisions at $\sqrt{s_{NN}}$ =200 GeV from STAR experiment [**?**]. Figure 2.13 shows the measured widths of balance function as a function of the impact parameter fraction $b/b_{\rm max}$, which is determined using a simple geometrical picture to relate impact parameter to fractions of the total cross section. From the plot we can see that the width of the balance function measured

for central collisions is significantly smaller than that for peripheral collisions. The results for the mid-peripheral and mid-central centrality classes decrease smoothly and monotonically from the peripheral collision value. Fig. 2.13 indicates that while the width observed in peripheral collisions is consistent with the HIJING prediction, the balance function for central collisions is significantly narrower, suggesting a variation in the underlying particle production dynamics between these two classes of events. In Fig. 2.13 the widths from the shuffled pseudorapidity events are also shown. These widths show little centrality dependence and are wider than those of the data or HIJING. The widths from shuffled pseudorapidity events represent the maximum possible width of a balance function measured with the STAR detector.

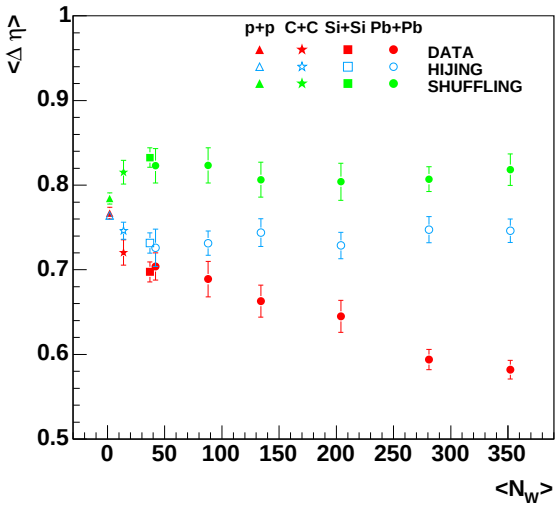

Figure 2.14: The dependence of the width of balance function on the number of wounded nucleons for $p + p$, $C + C$, Si + Si and Pb + Pb collisions at $\sqrt{s_{NN}}$ =17.2 GeV. The figure is taken from the NA49 paper [**?**].

The same kind of phenomenon have also been observed in different colliding system at low energy by in NA49 experiment [**?**]. Figure 2.14 shows the widths of balance function as a function of wounded nucleons for $p + p$, $C + C$, Si + Si and Pb + Pb collisions at $\sqrt{s_{NN}}$ =17.2 GeV. The narrowing effect is shown in data, while the HJING model failed to described the trend of data.

Since both STAR and NA49 experiments cover limited acceptance, it is important to study the influence of acceptance on the width of balance function. In Ref. [**?**], based

on the assumption of longitudinal boost invariance, Jeon and Pratt proposed a relation between the balance function in a rapidity window $B(\delta y|Y_{\rm w})$ and in the full rapidity range $B(\delta y|Y=\infty)$,

$$B(\delta y|Y_{\rm w}) = B(\delta y|\infty)(1-\delta y) \tag{2.11}$$

where $Y_{\rm w}$ is the size of the rapidity window.

The charge balance function is a differential combination of all possible charge correlations, and its integral over rapidity space is related to measures of charge fluctuation [**?**]. The charge fluctuation $D(Q)$ is defined as

$$D(Q) = \frac{4\langle(Q-\langle Q\rangle)^2\rangle}{\langle N_{\rm ch}\rangle} \tag{2.12}$$

where $Q = n_+ - n_-$ and $n_{\rm ch} = n_+ + n_-$. The charge fluctuation is approximately related to the BF by

$$\frac{D(Q)}{4} = 1 - \int_0^{Y_{\rm w}} B(\delta y|Y_{\rm w}){\rm d}\delta y + \mathcal{O}\left(\frac{\langle Q\rangle}{\langle n_{\rm ch}\rangle}\right), \tag{2.13}$$

2.2 Models

In this section we give a brief description of theory and phenomenological models used in comparison with the measurements.

Hydrodynamics

Hydrodynamics is a macroscopic approach to study the dynamical evolution of heavy ion collisions. In the model, the central assumption is that the strong interactions happen among the matter constituents, and shortly after that, the system reaches local thermalization. Only when the system is close to local thermal equilibrium, the hydrodynamic properties, i.e., its pressure, entropy density and temperature, are well defined. And only under these conditions, the equation of state of strongly interacting matter at high temperatures can be estimated.

At relativistic heavy ion collisions, the approximate longitudinal boost invariant boundary conditions in central phase space simplify hydrodynamic equations greatly [**?**].

Based on the local conservation law for energy, momentum and other conserved currents (e.g., baryon number):

$$\begin{aligned} \partial_\mu T^{\mu\nu}(x) &= 0 \\ \partial_\mu j^\mu(x) &= 0, \end{aligned} \tag{2.14}$$

the ideal fluid decompositions can be written as [?]

$$T^{\mu\nu}(x) = (e(x) + p(x))u^\mu(x)u^\nu(x) - g^{\mu\nu}p(x) \tag{2.15}$$

$$j^\mu(x) = n(x)u^\mu(x). \tag{2.16}$$

where $e(x)$ is the energy density, $p(x)$ the pressure and $n(x)$ the conserved number density at point $x^\mu = (t, x, y, z)$; $u^\mu(x) = \gamma(1, \upsilon_x, \upsilon_y, \upsilon_z)$ with $\gamma = 1/\sqrt{1 - \upsilon_x^2 - \upsilon_y^2 - \upsilon_z^2}$ is the local four velocity of the fluid. The great advantage of hydrodynamics is that it provides a covariant dynamics only depending on the equation of state (EOS) which is directly related to the lattice QCD calculations. While the disadvantage of hydrodynamics is that it can not describe the initial condition and the final freeze-out hypersurfaces, and all of these need to be modified by other models/assumptions.

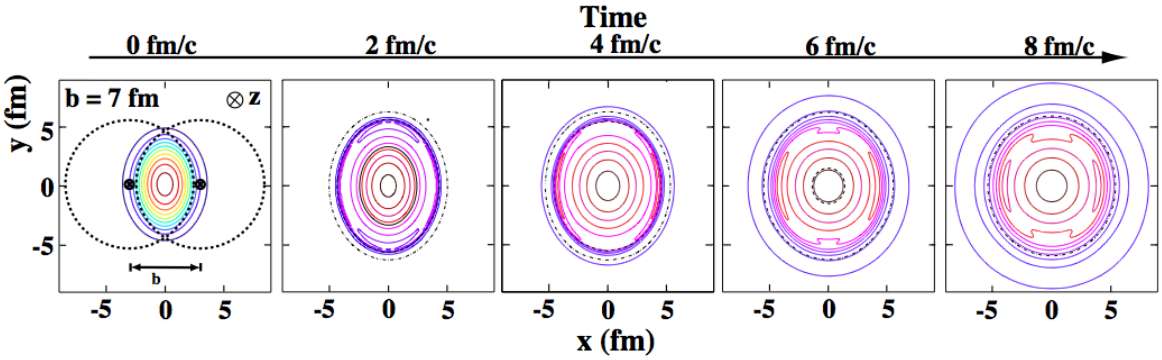

Figure 2.15: The time evolution of initial transverse energy density in coordinate space for non-central heavy ion collisions.

A phase transition from the QGP phase to a hadron gas causes a softening of the EOS: as the temperature crosses the critical temperature, the energy and entropy densities increase rapidly while the pressure rises slowly. The derivative of pressure to energy density has a minimum at the end of the mixed phase, known as the softest point. The diminishing driving force slow down the build-up of flow. Figure 2.15 shows the

contours of constant energy density in initial condition and times 2, 4, 6 and 8 fm/c after thermalization. The azimuthal anisotropy is introduced through the spatial deformation of the nuclear overlap zone at non-central collisions (see Fig.2.3). The system, which is driven by its internal pressure gradients, expands more strongly in its short direction (i.e. into the direction of the impact parameter) than perpendicular to the reaction plane where the pressure gradient is smaller. And it is clear that the anisotropy becomes less and less as system evolves.

Transport models

There are several transport Monte Carlo models trying to study the process of heavy ion collisions. The goals of those hadronic transport models, such as the Hadron-String Dynamics (HSD), Relativistic Quantum Molecular Dynamics (RQMD) and Ultrarelativistic Quantum Molecular Dynamics model (uRQMD) are to gain understanding of physical phenomena, i.e., creation of dense hadronic matter at high temperatures, properties of nuclear matter, creation and transport of rare particles in hadronic matter, *etc.*

Among them, a multiphase transport (AMPT) model is a model with both partonic phase and hadronic phase [**?**]. There are four main components in the model: the initial conditions, partonic interactions, conversion from the partonic to the hadronic matter, and hadronic interactions. The initial conditions, which include the spatial and momentum distributions of mini-jet partons and soft string excitations, are obtained from the heavy ion jet interaction generator (HIJING) model. Zhang's parton cascade (ZPC) is then used to describe scatterings among partons. There are two versions of AMPT model: the default AMPT model (version 1.11) which has a hadronization process based on the Lund string fragmentation model and the AMPT model with string melting (version 2.11) which uses a quark coalescence model instead. In the AMPT model with string melting, hadrons, which would have been produced from string fragmentation, are converted instead to their valence quarks and antiquarks. Scatterings among the resulting hadrons are described by a relativistic transport (ART) model. It is found that the default AMPT model gives a reasonable description of rapidity distributions and

transverse momentum spectra, while the AMPT model with string melting describes both the magnitude of the elliptic flow at mid-rapidity and the pion correlation function with a parton cross section of about 6 mb.

PYTHIA

PYTHIA [**?**] is a model for the generation of high-energy physics events, i.e. for the description of collisions at high energies between elementary particles such as $e^{\pm}$ and p ($\bar{p}$) in various combinations. It contains theory and models for a number of physics aspects, including hard and soft interactions, parton distributions, initial- and final-state parton showers, multiple interactions, fragmentation and decay.

CHAPTER 3

Experimental Set-up

The analysis of heavy ion collisions described in this thesis is performed on data taken with the STAR experiment at Relativistic Heavy-Ion Collider (RHIC). In this chapter, we introduce the experimental setup, the track reconstruction, the trigger configuration, the centrality definition and the particle identification.

3.1 RHIC

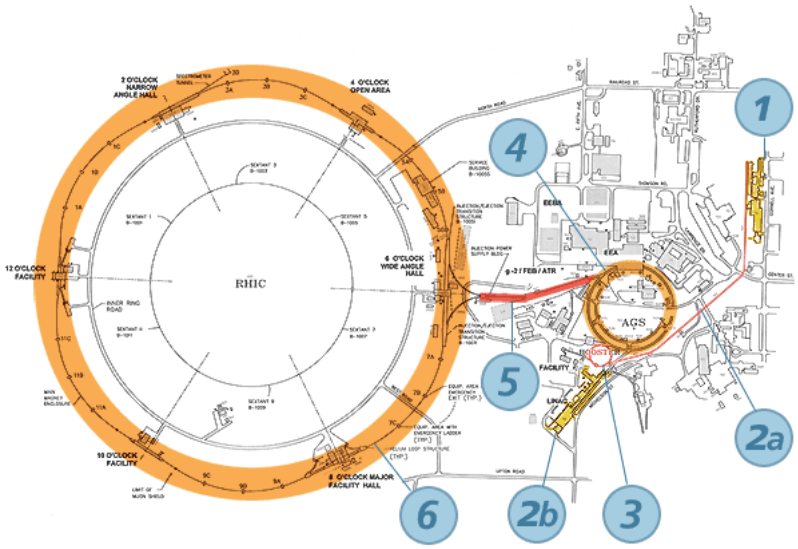

Figure 3.1: RHIC complex.

The Relativistic Heavy-Ion Collider (RHIC) at Brookhaven National Laboratory (BNL) is the first machine in the world capable of colliding heavy ions [**?**]. It is built tu investigate the strongly interacting matter created in heavy ion collisions [**?**]. The center-of-mass energy in a collision can be up to 200 GeV per nucleon pair which is

about a factor of ten larger than the highest energies reached at previous fixed target experiments, and as high as 500 GeV center-of-mass energy for polarized proton-proton collisions to study spin physics.

The Relativistic Heavy Ion Collider complex is composed of a group of particle accelerators as shown in Figure 3.1. Atoms are accelerated firstly to 15 MeV per nucleon in the Tandem Van de Graaff accelerator to remove some of their electrons using static electricity. Then the ions are sent towards the circular Booster (3) through a transfer line (2a). The Booster synchrotron accelerates the ions to 95 MeV per nucleon and then feeds the beam into the Alternating Gradient Synchrotron (AGS) where the ions are accelerated to 10.8 GeV per nucleon. Finally the ions injected to the beams via another AGS-to-RHIC Line (5) into the two rings of RHIC (6), and accelerated to the colliding energy 100 GeV per nucleon.

RHIC's 3.8 kilometer ring has six intersection points where its two rings of accelerating magnets cross, allowing the particle beams to collide. Six interaction points with four of them occupied by experiments: BRAHMS collaboration located at 2 o'clock position, STAR collaboration located at 6 o'clock position, PHENIX collaboration located at 8 o'clock position and PHOBOS collaboration located at 10 o'clock position.

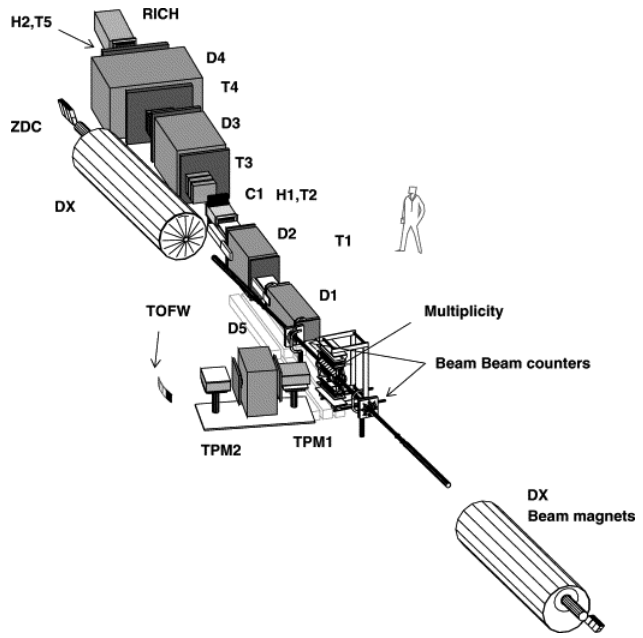

Figure 3.2: Schematic layout of the BRAHMS detector.

BRAHMS, as shown in Fig .3.2, employs two independently moveable spectrometer arms to measure the rapidity dependence of particle production with good particle identification capabilities [**?**]. Although the azimuthal coverage of each of the two arms is small, it is possible to cover the entire rapidity interval of $0 < |y| < 4$. The experiment has concluded its experimental program and stopped data taking in June 2006.

PHENIX, shown in Fig. 3.3, is designed specifically to measure direct probes such as electrons, muons and photons [**?**]. Aside from the global detectors for the event characterization, the detectors are grouped into two central arms and two forward muon arms. The central arms, covering the pseudo-rapidity region $|\eta| < 0.35$, consist of tracking subsystems for charged particles and electromagnetic calorimetry. Three sets of Pad Chambers (PC) and the Drift Chambers (DC) are used for the tracking. A Time Expansion Chamber (TEC), a ToF and RICH detectors provide particle identification. A lead-scintillator (PbSc) calorimeter and a lead-glass (PbGl) calorimeter measure the photons and electrons. Two muon spectrometers cover the pseudo-rapidity region $1.1 < |\eta| < 2.4$ and azimuth angle $0 < \phi < 2\pi$.

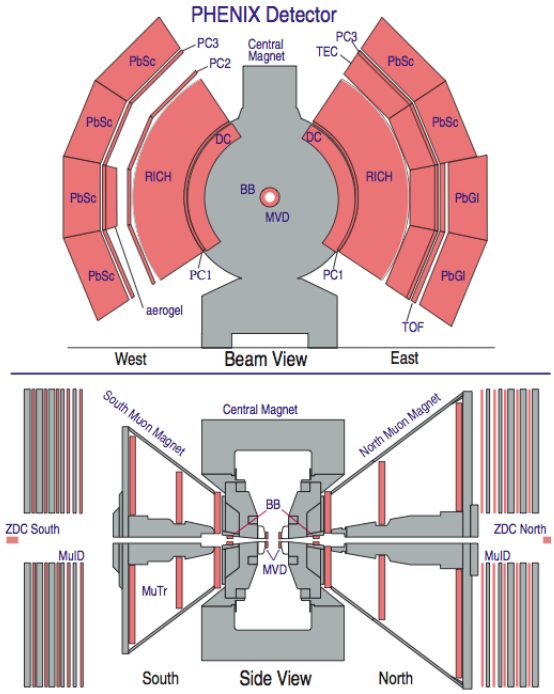

Figure 3.3: Layout of the PHENIX detector.

PHOBOS experiment is designed to detect charge particles using a multiplicity detec-

tor and two spectrometers arms cover a large rapidity interval [?] as shown in Figure 3.4. Its multiplicity array allow the measurement of charged particle multiplicities in the rapidity region $|\eta| \leq 5.4$. Two spectrometer arms allow the examination of identified charged particles for rapidities $0 \leq \eta \leq 2$ in greater detail.

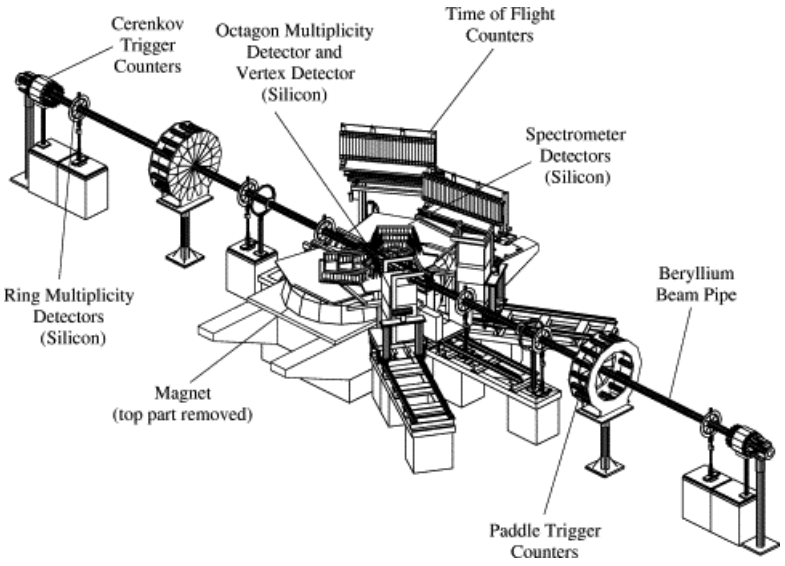

Figure 3.4: Schematic layout of the PHOBOS detector.

3.2 The STAR Experiment

STAR was constructed to investigate the behavior of strongly interacting matter at high energy density and to search for signatures of QGP formation. Key features of the nuclear environment at RHIC are a large number of produced particles (up to approximately one thousand per unit pseudorapidity) and high momentum particles from hard parton-parton scattering. STAR was designed primarily for measurements of hadron production over a large solid angle, featuring detector systems for high precise tracking, momentum analysis and particle identification at the center of mass rapidity. The large acceptance of STAR makes it particularly well suited for event-by-event characterization of heavy ion collisions and for the detection of hadron jets [?].

Figure 3.5 shows the Perspective view of the STAR detector, and a cutaway side view as configured for the RHIC 2004 run is displayed in Figure 3.6. The STAR detector

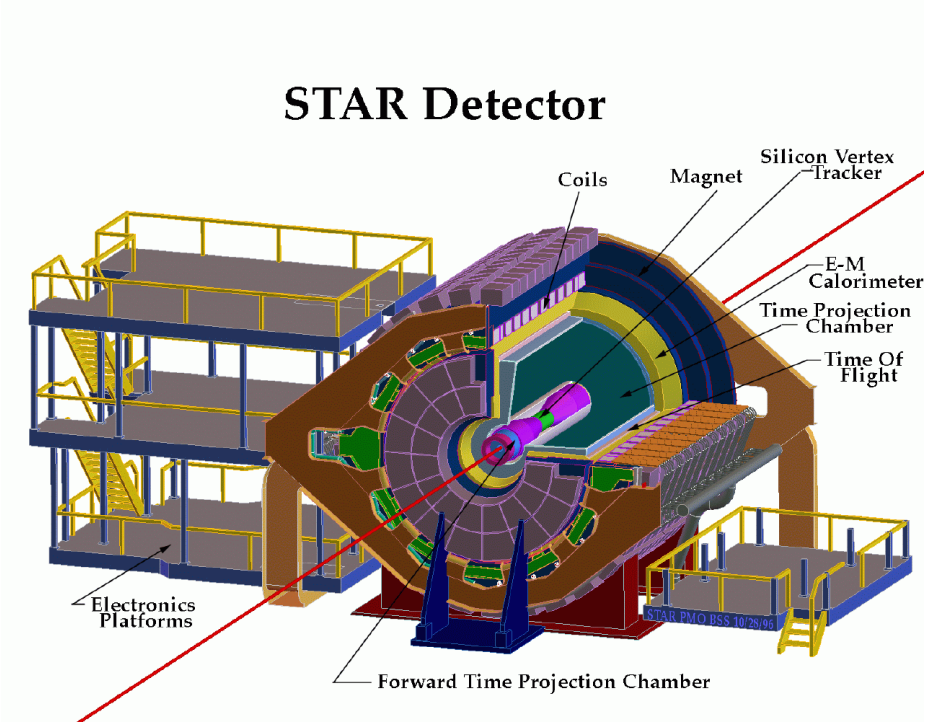

Figure 3.5: Perspective view of the STAR detector. Figure is taken from [**?**].

consists of several subsystems, which integrate to the whole functionality of the detector. It sits in a solenoidal magnet with an maximum magnitude field strength of 0.5 Tesla. The beam is surrounded by the beam pipe [**?**]. Its material, Berillium with low density and low nuclear charge is chosen to minimize the number of photon conversions and multiple scattering of particles traversing the beam pipe.

The primary tracking device of STAR is the Time Projection Chamber (TPC) [**?**]. A Barrel Electromagnetic Calorimeters (BEMC) [**?**] and an End-cap Electromagnetic calorimeter (EEMC) [**?**] are used to measure the transverse energy deposited by electrons and photons. The BEMC and EEMC are also used for triggering on events with high transverse energy or rare processes. In addition to the sub detectors used in event reconstruction, two Zero-Degree Calorimeters (ZDCs), two Beam Beam Counters (BBCs) and a Central Trigger Barrel (CTB) are used for event triggering. The Time-of-Flight (TOF) detector [**?**] measures the flying time of charged particles in TPC, which significantly improve the particle identification (PID) capability of TPC. It will allow STAR to extract the maximum amount of information available from soft physics measures on

an event-by-event basis. The Silicon Vertex Tracker (SVT) [**?**] was added to enhance physics capabilities of TPC. It can improve the primary vertexing, e.g., the two track separation resolution and the energy-loss measurement for particle identification. The SVT also expands the kinematical acceptance to very low momentum for charged particles which do not reach the active volume of the TPC due to the applied magnetic field by using independent tracking in the SVT alone. The Silicon Strip Detector (SSD) [**?**] constitutes the fourth layer of the inner tracking system. Installed between the SVT and the TPC, the SSD enhances the tracking capabilities of the STAR experiment by measuring accurately the two dimensional hit position and energy loss of the charged particles. Two cylindrical Forward Time Projection Chamber detectors (FTPCs) were constructed to extend the phase space coverage to the region $2.5 < |\eta| < 4.0$.

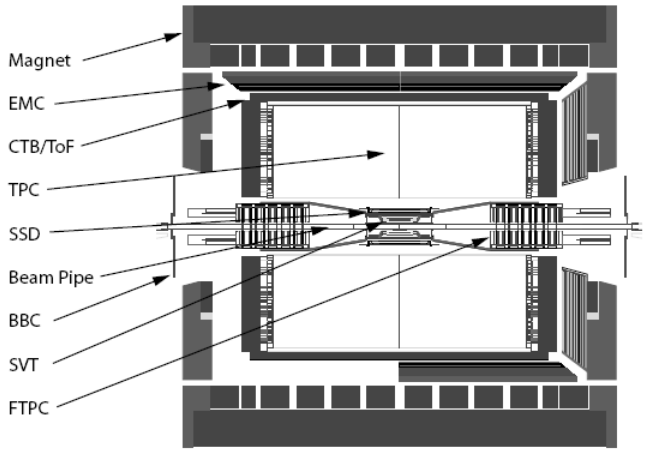

Figure 3.6: Cutaway side view of the STAR detector as configured in 2004.

3.2.1 STAR TPC

The Time Projection Chamber (TPC) is STAR's primary tracking device [**?**]. It records the tracks of particles, measures their momenta, and identifies the particles by measuring their ionization energy loss (dE/dx). Its acceptance covers ± 1.8 units of pseudorapidity through the full azimuthal angle and over the full range of multiplicities. Particles are identified over a momentum range from 100 MeV/c to greater than 1 GeV/c and momenta are measured over a range of 100 MeV/c to 30 GeV/c.

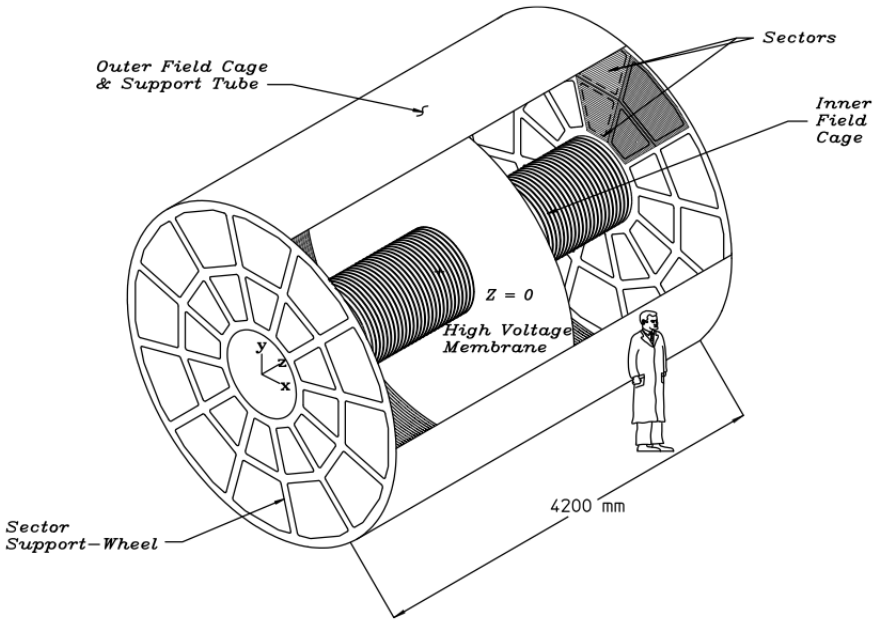

Figure 3.7: Perspective view of the STAR TPC.

The STAR TPC is shown schematically in Fig. 3.7. The TPC is 4.2 m long and 4 m in diameter and sits in a large solenoidal magnet [**?**] that operates at 0.5 T. It is an empty volume of gas in a uniform electric field of about 135 $V/$cm. The high-voltage Central Membrane (CM) is at the center of the TPC and Multi-Wire Proportional Chambers (MWPC) are at both end-caps. Charged particles are detected in drift chambers as they ionize the gas when passing through the volume. Electrons created from track ionization will drift in the longitudinal direction to the readout end-cap of the chamber along the TPC electric field lines.

The readout system locating on the ends of the TPC is based on MWPC with readout pads. The readout MWPC (Multi Wire Proportional Counter) have 3 wire planes: a gating grid, ground plane, and anode wires. The gating grid is the outermost wire plane on to separate the drift region from the amplification region. This grid controls the entry of electrons from the TPC drift volume into the MWPC. The drift electrons are allowed to pass through when a trigger is received and the event is recorded. Electrons initiate avalanches when they pass the gating grid and drift to the anode wires. The ground grid is used to terminate the field in the avalanche region as well as calibrate the pad electronics. The anode wires are held at a high voltage and provide the necessary electric

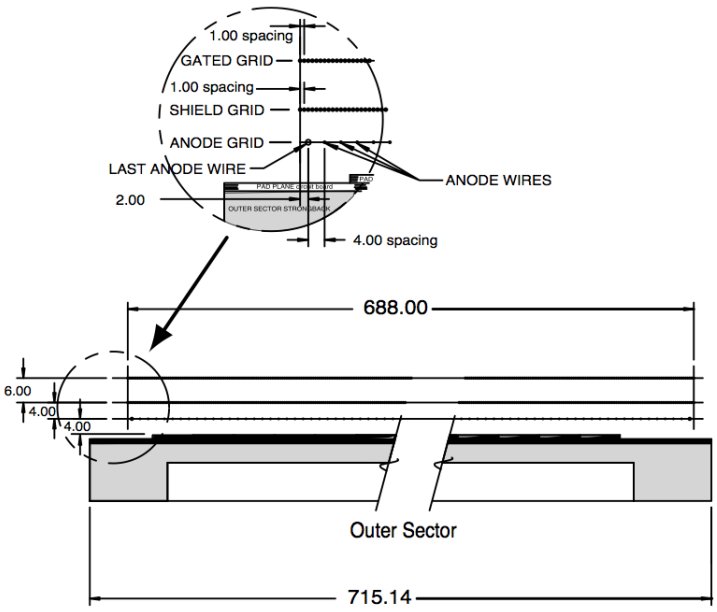

Figure 3.8: A cut-away view of an outer subsector pad plane. The cut is taken along a radial line from the center of the TPC to the outer field cage so the center of the detector is to the right. All dimensions are in millimeters. The figure is from [**?**].

field to avalanche the electrons from the track ionization. The avalanche leaves a cloud of positive ions, and the readout pads image their charge. The signal measured on the pads is then amplified, integrated and digitalized by the front-end electronics. These circuits can sample the arrival of electrons into at most 512 time buckets as well. The position of the ionizing particle along the drift direction (z coordinate) is reconstructed by the time bucket and the drift velocity. The x and y coordinates are determined by the location of the readout pad.

Each end-cap is instrumented with 72,000 pads which give xy coordinate information. The TPC is divided into 24 super sectors, each subsequently divided into an inner and outer sector, Figure 3.8 shows a cutaway view of the readout pad planes of an outer sector. The anode wires are held at a high voltage and provide the necessary electric field to avalanche the electrons from the track ionization. The avalanche leaves a cloud of positive ions, and the readout pads image their charge. The signal measured on the pads is then amplified, integrated and digitalized by the front-end electronics. These circuits can sample the arrival of electrons into at most 512 time buckets as well. The

position of the ionizing particle along the drift direction (z coordinate) is reconstructed by the time bucket and the drift velocity.

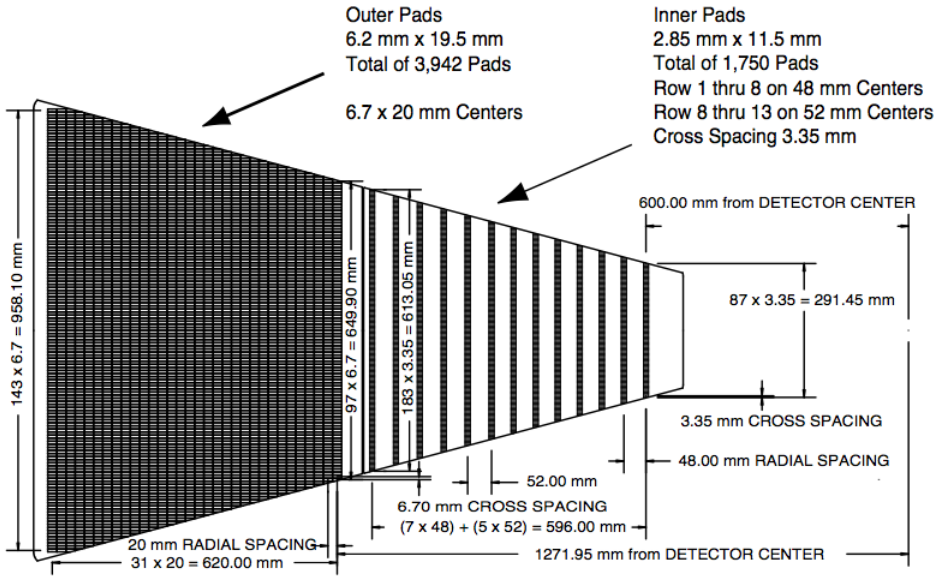

Figure 3.9: The anode pad plane with one full sector shown. The inner subsector is on the right and it has small pads arranged in widely spaced rows. The outer subsector is on the left and it is densely packed with larger pads. The figure is from [**?**].

The anode pad plane with one full sector is shown in Figure 3.9. The inner sector are grouped into 13 pad rows, with a total of 1750 small pads (2.85 mm $\times$11.5 mm). The outer sector are grouped into 32 pad rows, with a total of 3940 smaller pads (6.20 mm $\times$19.5 mm). The small pads in the inner sector are arranged in widely spaced rows to extend the position measurements along the track to small radii in a high track density environment. Whereas the outer sector has densely packed to improve the dE/dx resolution. Full track ionization signal is collected and more ionized electrons improve statistics on the dE/dx resolution with larger pads in the outer sector.

3.2.2 STAR FTPCs

The Forward Time Projection Chambers (FTPC) were constructed to extend the acceptance of the STAR experiment [**?**]. They cover the pseudorapidity range of $2.5 < |\eta| < 4.0$ on both sides of STAR and measure momenta and production rates of positively and

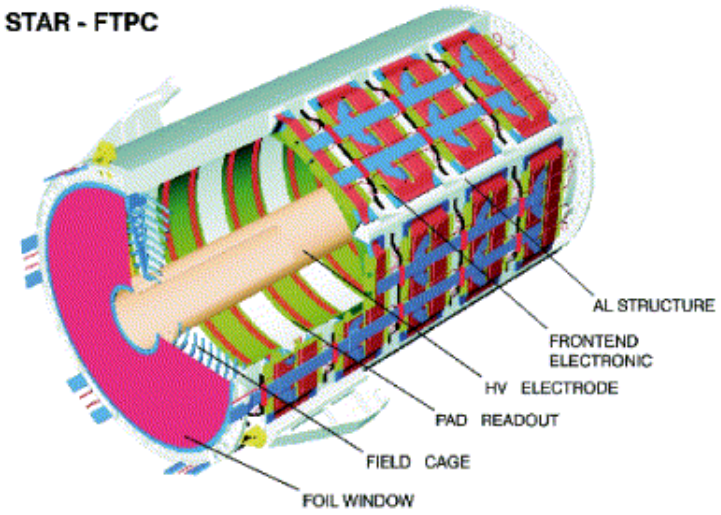

Figure 3.10: Schematic diagram of an FTPC.

negatively charged particles as well as neutral strange particles. Also, due to the high multiplicity, approximately 1000 charged particles in a central Au + Au collision, event-by-event observables like $\langle p_T \rangle$, fluctuations of charged particle multiplicity and collective flow anisotropies can be studied. The increased acceptance improves the general event characterization in STAR and allows the study of asymmetric systems such as p +A collisions.

Figure 3.10 shows the schematic diagram of an FTPC. It is a cylindrical structure with 75 cm in diameter and 120 cm long. Its radial drift field and readout chambers located in five rings on the outer cylinder surface. Each ring has two pad rows and is subdivided azimuthally into six readout chambers. In the region close to the beam pipe where the particle density is highest, the radial drift configuration was chosen to improve the two-track separation. The field cage is formed by the inner HV-electrode and the outer cylinder wall at ground potential. The field region at both ends is closed by a planar structure of concentric rings, made of thin aluminum pipes. The front end electronics (FEE) mounted on the back of the readout chambers are used to amplify, shape, and digitize the signals. Each particle trajectory is sampled up to 10 times. The ionization electrons are drifted to the anode sense wires and induced signals on the adjacent cathode surface are read out by 9600 pads (each $1.6 \times 20\text{mm}^2$).

CHAPTER 4

Analysis Method

In this chapter, we discussed the dataset and the cuts used for analysis. The particle identification for charged particles $\pi^{\pm}$, p ($\bar{p}$) and the reconstructed particles K^0_S, Λ ($\bar{\Lambda}$) are also presented. Event plane method and cumulant method have been developed to accurate measurements of anisotropic flow.

4.1 Event and track selection

The STAR experiment collects about 25 million and 60 million minimum bias events during RHIC Run IV and VII for Au + Au collisions at $\sqrt{s_{NN}}$ = 200 GeV, separately. The trigger and event selection are summarized in Table 4.2. Events with Primary Vertex z (V_z) further than 30 cm from the main TPC center were discarded. Events useful for our analysis are listed in the most right column.

Trigger Setup Name	Production	Vertex Cut	Trigger ID	Events No.
productionMinBias	P05ic	$\|V_z\| < 30$ cm	15007	13.4 M
productionMinBias	P05ic	$-10 < V_z < 50$cm	15003	6.2 M
productionLowMidHigh	P05ic	$\|V_z\| < 30$cm	15007	6.3 M

Table 4.1: Run IV trigger and events selection for minimum bias in Au + Au collisions at $\sqrt{s_{NN}}$ = 200 GeV.

There are two kind of reconstructed tracks. One is called the global track, the other is called the primary track. After fitting all the hit points in TPC by helix, we can reconstruct the global tracks. With all of the global tracks from one event reconstructed,

Trigger Setup Name	Production	Vertex Cut	Trigger ID	Events No.
2007ProductionMinBias	P08ic	$\|V_z\| < 30$ cm	200001, 200003	50 M
2007Production2	P08ic	$\|V_z\| < 30$ cm	200013	10 M

Table 4.2: Run VII trigger and events selection for minimum bias in Au + Au collisions at $\sqrt{s_{NN}} = 200$ GeV.

the collision vertex can be found by extrapolating tracks back to the origin. The primary track is defined by the helix fit to the TPC points along with the vertex.

The centrality is defined by the so-called TPC reference multiplicity. The TPC reference multiplicity is the number of the primary tracks in the TPC with the 15 or more fit points having the pseudo-rapidity from -0.5 to 0.5 and a distance of closet approach (DCA) to the primary vertex less than 3 cm. A part of low multiplicity events are rejected due to a lower cut on CTB to reject the non-hadronic events. The total number of events should be corrected by the Glauber model. The nine centrality bins and the corresponding geometric cross section are listed in Table 4.3.

Centrality Bin	Reference Multiplicity	Geometric Cross Section
1	14-31	70%-80%
2	31-57	60%-70%
3	57-96	50%-60%
4	96-150	40%-50%
5	150-222	30%-40%
6	222-319	20%-30%
7	319-441	10%-20%
8	441-520	5%-10%
9	$\geq$520	0%-5%

Table 4.3: Run IV centrality bins in Au + Au collisions at $\sqrt{s_{NN}} = 200$ GeV.

Figure 4.1 shows charged particle multiplicity distribution without the Glauber correction. $0-80\%$ centrality is so-called minbias data in the analysis. Sometimes we need to use wide centrality bins to get better statistic, thus the three combined centrality

bins, $0-10\%$ (central), $10\%-40\%$ (mid-central) and $40\%-80\%$ (peripheral) are used as indicated in the Fig. 4.1.

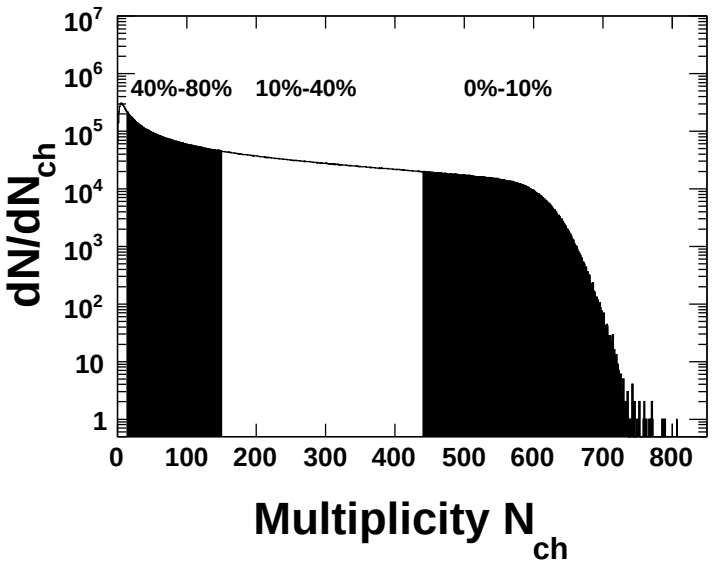

Figure 4.1: The TPC reference multiplicity distribution in Au + Au collisions at $\sqrt{s_{NN}}$ = 200 GeV of Run IV.

The inclusion of inner tracking for the Run VII Au + Au 200 GeV data rendered reference multiplicity a poor method to determine centrality. It's shown there is a dependence on the primary vertex position for the reconstruction efficiency in the $|V_z| < 30$ cm region. The dependence was generally absent for TPC only tracking used in many of the previous productions, and is undesirable since it requires the centrality cuts to change as a function of V_z. To this end, another variable was proposed called global reference multiplicity is used for centrality definition.

Global reference multiplicity is the number of global tracks in the TPC with the 10 or more fit points having the pseudo-rapidity from -0.5 to 0.5 and a distance of closet approach (DCA) to the primary vertex less than 3 cm. The nine centrality bins and the corresponding geometric cross section for Au + Au collisions are listed in Table 4.4 .

The remaining issues are biases on multiplicity distribution introduced by the main online Vertex Position Detector (VPD) trigger-setup (200013). The biases come from

Centrality Bin	Global Reference Multiplicity	Geometric Cross Section
1	10-20	70%-80%
2	21-38	60%-70%
3	39-68	50%-60%
4	69-113	40%-50%
5	114-177	30%-40%
6	178-268	20%-30%
7	269-398	10%-20%
8	399-484	5%-10%
9	$\geq$485	0%-5%

Table 4.4: Run VII centrality bins in Au + Au collisions at $\sqrt{s_{NN}} = 200$ GeV.

two sources. Firstly, over the full range in V_z, the VPD is more efficient at triggering on central events relative to peripheral. This leads to a general deficit in peripheral events for a given data sample. The second comes from a centrality dependence of the VPD's online V_z resolution which is worse for peripheral events relative to central as shown in this link. Since the trigger-setup (200013) insisted events events fall within the inner tracking acceptance, i.e., with an online cut of $|V_z| < 5$ centimeter, the resolution issue means that events at the higher $|V_z|$ are more likely to peripheral whereas the events at lower $|V_z|$ are more likely to be central.

The V_z dependent biases in multiplicity distribution require a re-weighting correction to be applied for all analysis. For any analysis with a "signal" summed up over a range of global reference multiplicity, events at $|V_z| \sim 0$ will have their peripheral contribution scaled up in order to restore the unbiased case via the correction. The opposite will be true for events at higher $|V_z|$ where the peripheral contribution will be scaled down - again to the restore the the unbiased case. The correction has to be applied as function of V_z in 2 centimeter bins for acceptance reasons.

In a given V_z bin, firstly the weights have to be determined. This is done by normalizing the global reference multiplicity distribution by the number of events with global reference multiplicity larger than 500. The MC Glauber histogram then has be divided

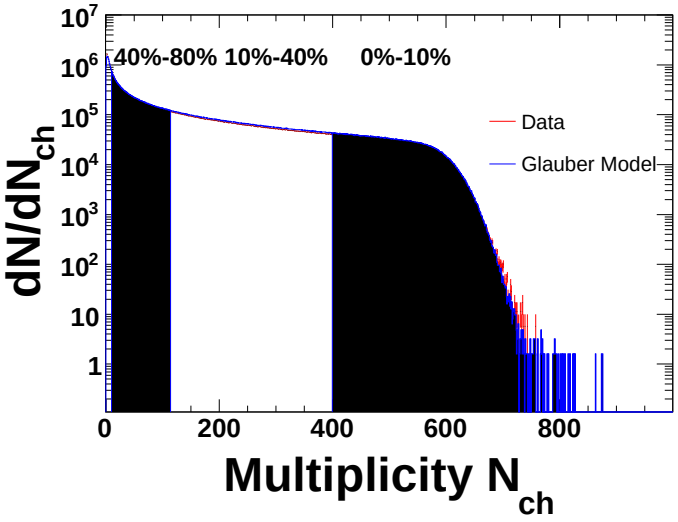

Figure 4.2: The TPC global reference multiplicity distribution in Au + Au collisions at $\sqrt{s_{NN}}$ = 200 GeV of Run VII.

by the normalized global reference multiplicity distribution to calculate the weights. Finally in each event, we multiply the event quantities by its weight which is got according to V_z and global reference multiplicity in this event. Figure 4.2 shows global reference multiplicity distribution after the correction and the comparison with Glauber Monte-Carlo calculation.

4.2 Particle Identification

Charge particles passing through the TPC will lose energy via ionization. The charge collected for each hit on a track is proportional to the energy loss of the particle. For a particle with charge Z (in units of e) and speed $\beta = v/c$ transversing a medium with density ρ, the mean energy loss is described by the Bethe-Bloch formula

$$\langle \frac{dE}{dx} \rangle = 2\pi N_0 r_e^2 m_e c^2 \rho \frac{Z z^2}{A\rho^2} [\ln \frac{2m_e\gamma^2 v^2 E_M}{I^2} - 2\gamma^2], \tag{4.1}$$

where N_0 is Avogadro's number, m_e is the electron mass, $r_e(= e^2/m_e)$ is the classical electron radius, c is the speed of light, z is the atomic number of the absorbing material, A is the atomic weight of the absorbing material, $\gamma = 1/\sqrt{(1-\beta^2)}$, I is the mean

excitation energy, and $E_M(= 2m_e c^2\beta^2/(1-\beta^2))$ is the maximum transferable energy in a single collision.

It's clear from the equation that different particle species with the same momentum p have different amounts of mean energy loss, so we can identify charge particles by their specific energy loss in TPC. Fig. 4.3 shows the energy loss for particles in the TPC as a function of momentum.

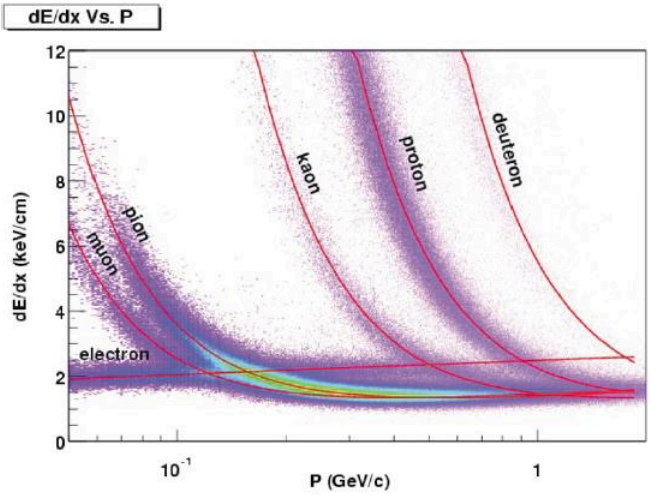

Figure 4.3: The energy loss distribution as a function of p_T in TPC.

In order to quantitatively describe the particle identification, a variable is defined (in the case of charged pion identification) as

$$n\sigma_\pi = \ln[\frac{dE}{dx}_{meas} - \langle\frac{dE}{dx}\rangle_\pi]/\sigma_{dE/dx}, \tag{4.2}$$

in which $\frac{dE}{dx}_{meas}$ is the measured energy loss of a track and $\langle\frac{dE}{dx}\rangle_\pi$ is the expected mean energy loss for charged pion. $\sigma_{dE/dx}$ denotes the resolution of specific ionization in the TPC. For the identification of charged kaon, proton and anti-proton, a similar definition can be given by $n\sigma_K$, $n\sigma_p$ and $n\sigma_{\bar{p}}$. The different particle species can be selected by applying the cuts on the variables.

The typical resolution of dE/dx in Au + Au collisions is $\sim 8\%$, which allows for the π/K separation up to $p \sim 0.7$ GeV/c and p/π separation up to $p \sim 1.1$ GeV/c.

In high momentum region ($p_T > 2.5$ GeV/c), we can extend the pion and (anti)proton identification. This method is based on the clear separation of the mean dE/dx for

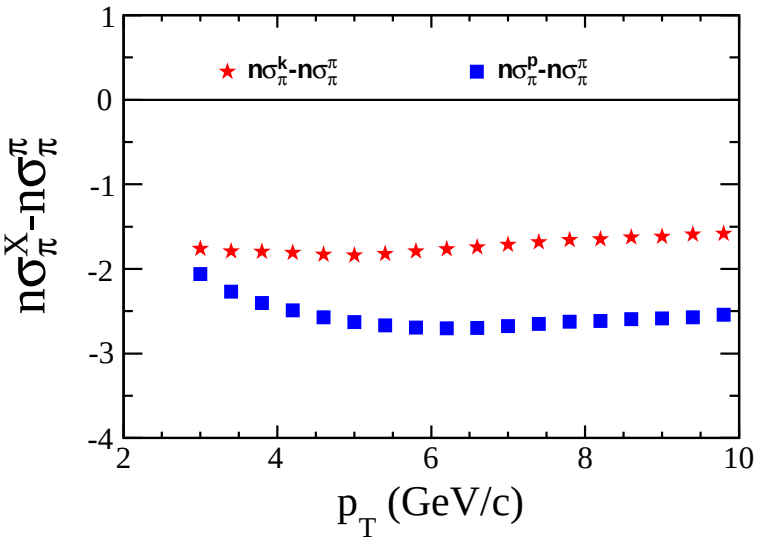

Figure 4.4: The relative dE/dx peak positions of $n\sigma_\pi^p$ and $n\sigma_\pi^K$ as a function of p_T.

different particles in the relativistic rise region of dE/dx as shown in Fig. 4.4. The differences of dE/dx between pion and other charged particles ($n\sigma_\pi^p$ and $n\sigma_\pi^K$) are shown in Fig. 4.4. The kaon band is about 1.8σ away from the pion band with little p_T dependence in $p_T > 2.5$ GeV/c region, while the proton band is about 2σ away from the pion band and leaver further in $3 < p_T < 5$ GeV/c region.

Pions and protons are identified with a cut of $n\sigma_\pi > 0$ and $n\sigma_p < 0$ respectively. The corresponding purities are 95% for pion and 67% fro proton, respectively. The purity of proton increase since the proton band separates further from the kaon band and pion band as p_T increases. The contamination to pion will decrease pions v_2 by less than 1% for the high purity of pions. The contamination to proton s arise from kaon (28%) and pions (5%) using at $3.0 < p_T < 3.5$ GeV/c region. Figure 4.5 shows an example of $n\sigma_p$ distribution with 3-Gaussian fit.

This method is confirmed by the STAR TOF measurements.

4.3 K_S^0 and Λ Reconstruction

We reconstruct K_S^0 and Λ through their weak decay channel. The properties of these decays are summarized in Table 4.5.

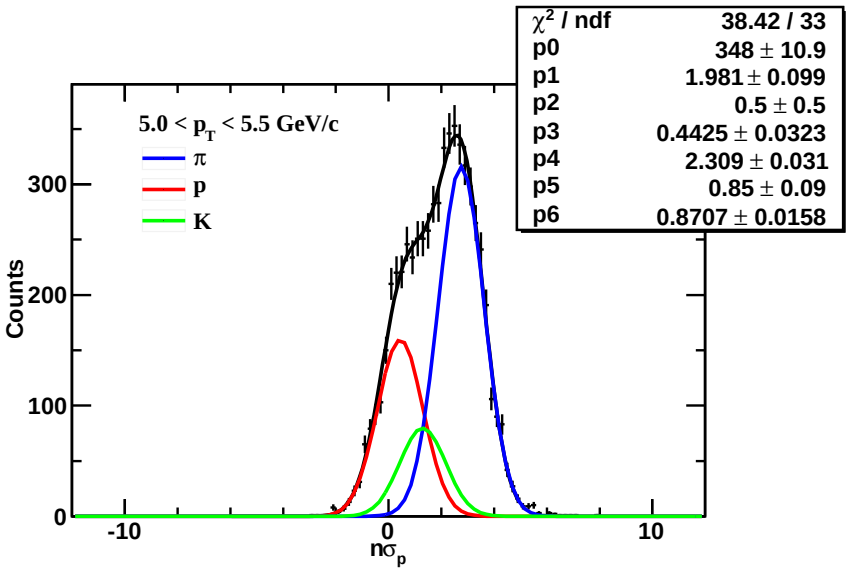

Figure 4.5: $n\sigma_p$ distribution at $5.0 < p_T < 5.5$ GeV/c. The black curve is the 3-Gaussian fit.

Particle Type	Decay Channel	Branching Ratio (%)	$c\tau$ (cm)	Mass (GeV/c^2)
K^0_S	$\pi^+ + \pi^-$	68.95 ± 0.14	2.68	0.497
Λ $\bar{\Lambda}$	$p + \pi^-$ $(\bar{p} + \pi^+)$	63.9 ± 0.5	7.89	1.115

Table 4.5: K^0_S and Λ $\bar{\Lambda}$ weak decay properties

The identification of K^0_S and Λ is based on statistics-wise invariant mass distribution. The charged $\pi^{\pm}$ and p ($\bar{p}$) tracks are identified by the energy loss in TPC. We can get the four-momentum of $\pi^{\pm}$ and p ($\bar{p}$) by assigning their mass and momentum measured from the helix in TPC and then calculate the invariant mass of all possible pairs of positive and negative charged particles.

There are some reasons that could lead to the combinatorial background, e.g., the misidentification of daughter track, the decay vertex close to the primary vertex and daughter tracks of a pair from different $V0$. We utilize decay geometry to reject those fake decay vertexes. $c\tau$ of K^0_S and Λ is 2.68 centimeter and 7.89 centimeter. Most of them will decay in the TPC of 2 m radius. In the laboratory frame, the decay vertex is in the order of a few centimeter further than primary vertex with several hundreds microns. So the decay vertex is well separated from the primary vertex. The decay topology is shown in Figure 4.6. The $V0$ is named after the "V" topology with the "0" net charge. The dca (distance of closet approach) between two daughter tracks is the parameter to determine the point of the decay vertex. The real decay vertex should distribute at smaller dca than fake decay vertex. dca1 (dca2) is the dca of the daughter to the primary vertex. The decay daughters should distribute at larger values than primary tracks. b is the dca from the primary vertex to the direction of $V0$ momentum. Ideally, b is equal to zero. rv is the distance which $V0$ travels in TPC (decay length).

p_T (GeV/c)	< 0.8	0.8-3.6	> 3.6
π dca to primary vertex (cm)	> 1.5	> 1.0	> 0.5
dca between daughters (cm)	< 0.7	< 0.75	< 0.5
dca from primary vertex to V0	< 0.7	< 0.75	< 0.5
decay length (cm)	4-150	4-150	10-120

Table 4.6: Cuts selection criteria for K^0_S in Au + Au collisions at $\sqrt{s_{NN}} = 200$ GeV.

Table 4.6 and Table 4.7 list the $V0$ optimized cuts for K^0_S and Λ in Au + Au collisions at $\sqrt{s_{NN}} = 200$ GeV, respectively. These cuts are used for this v_2 analysis. Applying

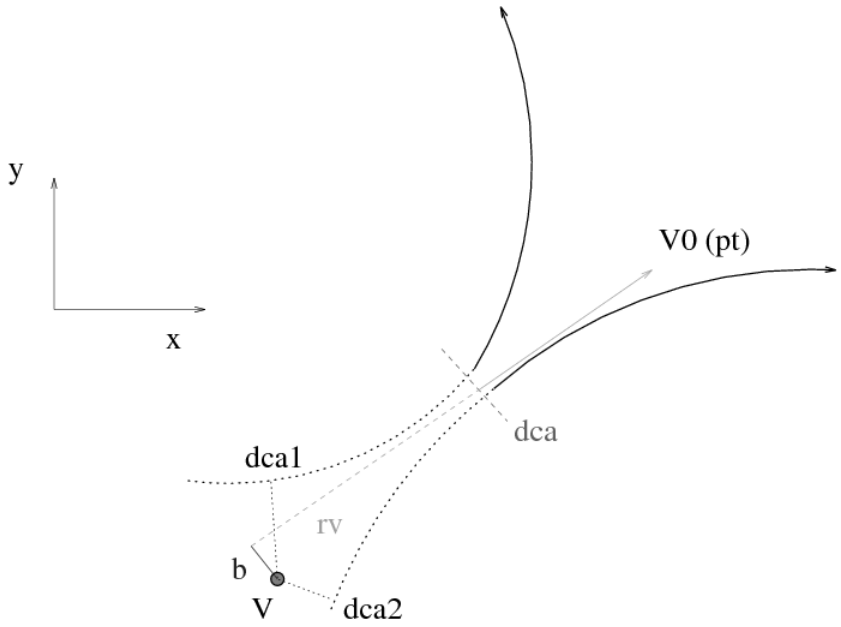

Figure 4.6: $V0$ decay topology, Figure from [**?**]

p_T (GeV/c)	< 0.8	0.8-3.6	> 3.6
π dca to primary vertex (cm)	> 2.5	> 2.0	> 1.0
p dca to primary vertex (cm)	> 1.0	> 0.75	> 0
dca between daughters (cm)	< 0.7	< 0.75	< 0.4
dca from primary vertex to V0	< 0.7	< 0.75	< 0.75
decay length (cm)	4-150	4-150	10-125

Table 4.7: Cuts selection criteria for Λ in Au + Au collisions at $\sqrt{s_{NN}} = 200$ GeV.

these cuts, the signal over background ratio will be significantly enhanced.

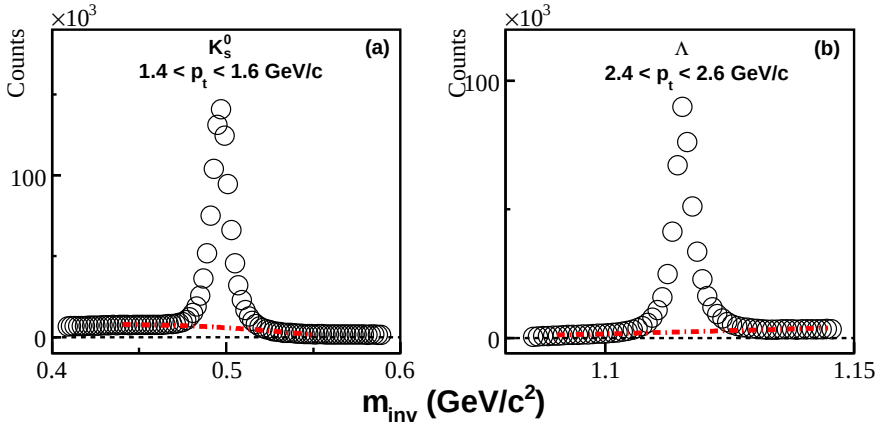

Figure 4.7: The invariant mass distributions of (a) K^0_S at $1.4 < p_T < 1.6$ GeV/c and (b) Λ at $2.4 < p_T < 2.6$ GeV/c at Au + Au collisions minbias (0-80%) are shown. The rad dash lines are polynomial fit of the backgrounds.

For K^0_S and Λ , the remaining backgrounds are estimated from the fit to the invariant mass distribution with functions describing signals and backgrounds. The fit function is two gaussian plus a polynomial. We use two gaussian functions with the same mass peak parameter to describe signal and use a polynomial function to describe the backgrounds. The fourth and second order polynomial functions are used in order to estimate the systematic errors from background uncertainties. The systematic error is a few percent, we will discuss in details later. The background distribution is estimated from the polynomial in the fit. The signal distribution is estimated by data minus polynomial. The signal over total ratio distribution and background over total ratio distribution (fit over data) will be used to extract K^0_S and Λ signal v_2.

4.4 Event plane method

In this section, we introduce the Fourier expansion of azimuthal particle distribution and its properties with respect to the reaction plane. And we also introduce event plane which is the estimate of the true reaction plane determined by using the signal of flow itself.

4.4.1 Fourier expansion

The quantity under study in the most general case is the triple differential distribution. In this, the dependence on the particle emission azimuthal angle measured with respect to the reaction plane can be written in a form of Fourier series

$$E\frac{d^3N}{d^3p} = \frac{1}{2\pi}\frac{d^2N}{p_T dp_T dy}(1 + \sum_{n=1}^{\infty} 2v_n \cos[n(\phi - \Psi_r)]), \tag{4.3}$$

where Ψ_r denotes the (true) reaction plane angle, and the sine terms vanish due to the reflection symmetry with respect to the reaction plane. The main advantage of the Fourier method is that the Fourier coefficients, evaluated using observed event planes, can be corrected for the event plane resolution caused by the finite multiplicity of the events. The great importance of this is that then the results for particles in a certain phase space region may be compared directly to theoretical predictions, or the simulations unfiltered for the detector acceptance, and for which the reaction plane has been taken to be the plane containing the theoretical impact parameter.

4.4.2 Event plane determination

The Fourier coefficients in the expansion of the azimuthal distribution of particles with respect to event plane are evaluated to study the anisotropy of the event. The standard event plane method is proposed to study flow by reconstructing the reaction plane Ψ_r. The estimated reaction plane is called the event plane.

Starting from the n^{th} harmonic event flow vector Q_n whose x and y components are given by

$$Q_n \cos(n\Psi_n) = X_n = \sum_i w_i \cos(n\phi_i) \tag{4.4}$$

$$Q_n \sin(n\Psi_n) = Y_n = \sum_i w_i \sin(n\phi_i) \tag{4.5}$$

The n^{th} harmonic event plane can be obtained by

$$\Psi_n = \left(\tan^{-1} \frac{\sum_i w_i \sin(n\phi_i)}{\sum_i w_i \cos(n\phi_i)} \right) / n, \tag{4.6}$$

where ϕ is the azimuthal angle of a particle. The sum goes over the particles used in the event plane determination, and w_i is the weight to optimize the event plane resolution. Usually the weights are assigned with the transverse momentum. This choice of weights is to make the event plane resolution the best by maximizing the flow contributions to the flow vector. The tracks selection criteria to reconstruct the event plane is listed in Table 4.8.

Flow track selection criteria	
nHits	> 15
nHits/nMax	> 0.52
dca	< 2 cm
transverse momentum	$0.1 < p_T < 2.0$ GeV/c

Table 4.8: Selection criteria for flow tracks used in the event plane reconstruction

For a given n the corresponding Fourier coefficient v_n can be evaluated using the reaction planes determined from any harmonic m, with $n \geq m$, if n is a multiple of m. For the event plane evaluated from the m^{th} harmonic the Fourier expansion is

$$\frac{d(wN)}{\phi - \Psi_m} = \frac{wN}{2\pi}(1 + \sum_{k=1}^{\infty} 2v_{km}^{\text{obs}} \cos[km(\phi - \Psi_m)]). \tag{4.7}$$

When a particle has been used in the calculation of an event plane, the auto-correlation effect in its distribution with respect to this plane is removed by recalculating that plane without this particle. This method of removing autocorrelations assumes that contributions from conservation of momentum are small.

At ultra-relativistic energies, the second order event plane Ψ_2 has the highest resolution. Elliptic flow and the higher order even harmonics estimated with respect to the Ψ_2 are denoted as $v_2\{\text{EP}_2\}, v_4\{\text{EP}_2\}$ etc.

4.4.3 Detector effect

The event plane angle is random in the laboratory frame, thus its distribution should be flat if the detector is perfect. A straightforward detector induced bias is non-uniform azimuthal coverage which can be corrected for as long as the non-uniformities are small. Several procedures aiming at flattening the event plane angle distribution have been developed. One of most commonly used methods is to use the distribution of the particles themselves as a measure of the acceptance. We use the inverting the ϕ distributions of detected tracks for a large event sample, which is called "ϕ weight". The ϕ weights are folded into the weight w_i in Equation 4.4 and 4.5.

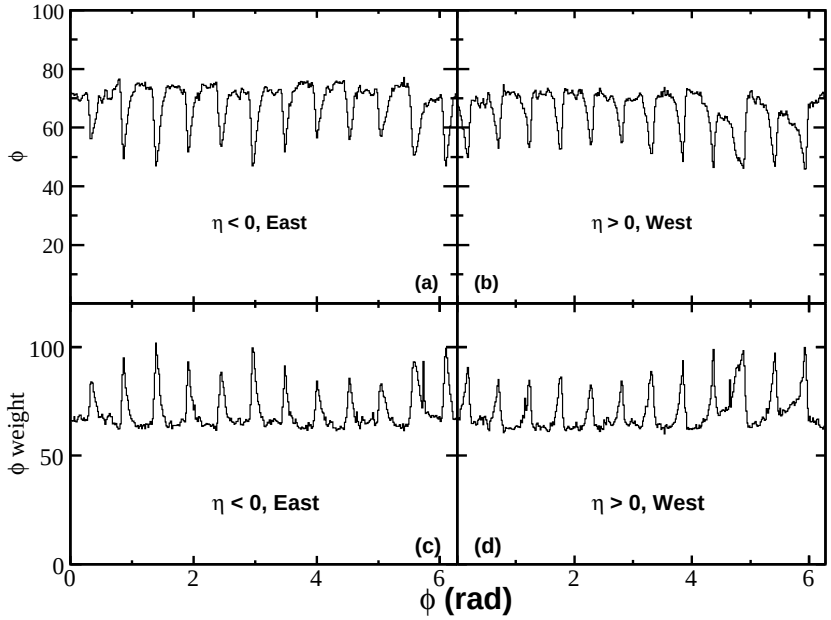

Figure 4.8: ϕ and the corresponding ϕ weight distributions in east and west TPC for $0-5\%$ centrality in Au + Au collisions at $\sqrt{s_{NN}} = 200$ GeV.

Fig. 4.8 (a) and (b) show the ϕ distribution of east TPC ($\eta < 0$) west TPC ($\eta > 0$) for $0-5\%$ centrality data in Au + Au collisions at 200 GeV. The corresponding ϕ weights are shown on Fig. 4.8 (c) and (d).

After used ϕ weight, the 2^{nd} order event plane distribution is shown in Fig. 4.9 as red curve. The black curve shows a constant fit to the event plane azimuthal distribution.

We also use both the Forward Time Projection Chambers (FTPCs) to determine

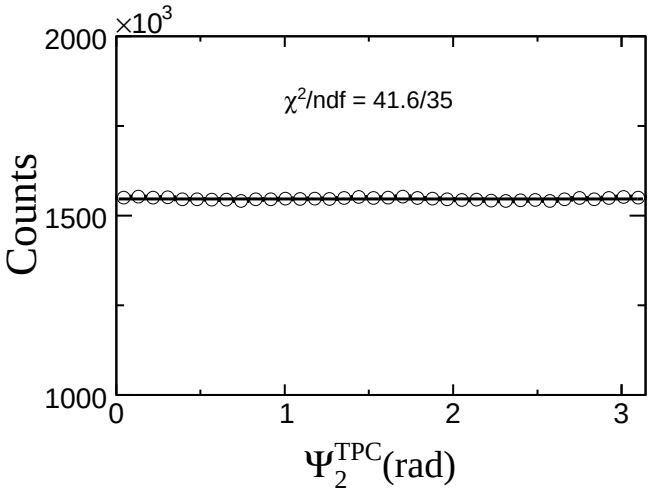

Figure 4.9: The distribution of 2nd harmonic event plane angle (Ψ_2) from TPC in Au + Au collisions at $\sqrt{s_{NN}} = 200$ GeV.

an event plane for each event. The FTPCs cover pseudo-rapidity $|\eta|$ from 2.5 to 4.0. This rapidity gap helps to reduce non-flow contributions. Non-flow effects refer to the correlations that are not associated with the reaction plane. Included in non-flow effects are jets, resonance decay, short-range correlations such as the Hanbury-Brown Twis (HBT) effect, and momentum conservation.

Due to the several acceptance loss for FTPCs, ϕ weight method is not enough to generate the flat event plane distribution. Thus, the shifting method [**?**] is applied to force the event plane distribution to be flat. The corrected new angle is defined as

$$\Psi^{'} = \Psi + \Delta\Psi, \tag{4.8}$$

where $\Delta\Psi$ is written in the form

$$\Delta\Psi = \sum_{n}[A_n \cos(n\Psi) + B_n \sin(n\Psi)]. \tag{4.9}$$

Requiring the vanishing of the n^{th} Fourier moment of the new distribution, the coefficients A_n and B_n can be evaluated by the original distribution

$$\begin{aligned} A_n &= \frac{2}{n}\langle\cos(n\Psi)\rangle, \\ B_n &= -\frac{2}{n}\langle\sin(n\Psi)\rangle, \end{aligned} \tag{4.10}$$

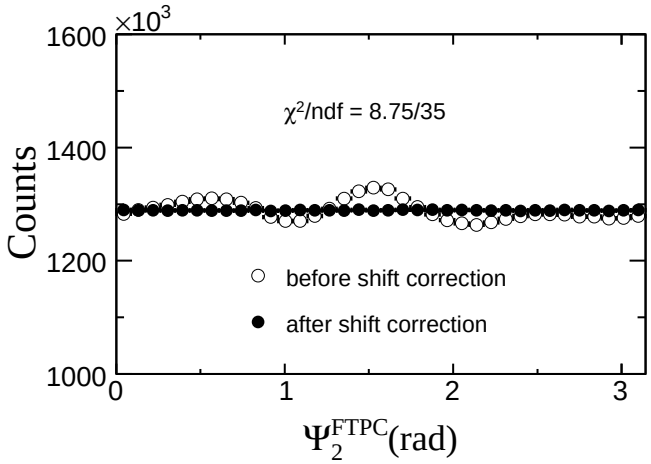

Figure 4.10: The distribution of 2nd harmonic event plane angle (Ψ_2) from FTPC in Au + Au collisions at $\sqrt{s_{NN}}$ = 200 GeV. The black curve is the const fitting of the FTPC event distribution after shift correction.

$\langle \cdots \rangle$ is the average over the whole event sample

It gives the Equation 4.11 which shows the formula for the shift correction. The average in Equation 4.11 goes over a large sample of events. The higher harmonic you apply, the flatter the event plane distribution is. In case of infinite order, the event plane distribution will be perfectly flat. In the analysis, the correction is done up to 20th harmonic. The distributions of Ψ_2^{East} and Ψ_2^{West} are flatten separately and then the full-event plane distributions are flattened. Accordingly, the observed v_2 and resolution are calculated using the rotated (sub)event plane azimuthal angle

$$\Psi' = \Psi + \sum_n \frac{1}{n}[-\langle \sin(2n\Psi)\rangle \cos(2n\Psi) + \langle \cos(2n\Psi)\rangle \sin(2n\Psi)]. \quad (4.11)$$

Figure 4.10 shows the second harmonic event plane azimuthal distribution after shift correction are applied in FTPC. The black curve shows a constant fit to the event plane azimuthal distribution.

The finite number of detected particles produces limited resolution in the angle of the measured event plane, so the coefficients in the Fourier expansion of the azimuthal distributions with respect to reaction plane must be corrected up to what they would be

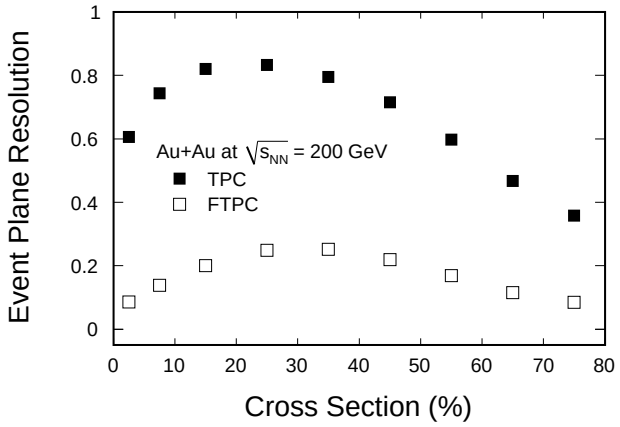

Figure 4.11: The 2nd order TPC event plane and FTPC resolution for v_2 in Au + Au collisions at $\sqrt{s_{NN}} = 200$ GeV for 9 different centrality intervals.

relative to the real reaction plane

$$v_n = \frac{v_n^{\rm obs}}{\langle \cos[km(\Psi_m - \Psi_r)] \rangle}, \tag{4.12}$$

where v_2, $v_2^{\rm obs}$, Ψ_2 and Ψ_r refer to the real v_2, observed v_2, the event plane angle and the real reaction plane angle. $\langle \cdots \rangle$ is the average over the whole event sample. It is found that $< \cos[2(\Psi_2 - \Psi_r)] >$ is the reaction plane resolution. To calculate it, we divide a full event into two sub-sets of tracks (sub-events). According to Equation 4.6, we calculate the event plane of two sub-events separately. The event plane resolution for the sub-event is given by Equation 4.13.

$$\langle \cos[2(\Psi_2^A - \Psi_r)] \rangle = \sqrt{\langle \cos[2(\Psi_2^A - \Psi_2^B)] \rangle} \tag{4.13}$$

Since we have two independent event plane from west and east FTPC, we can estimate the event plane resolution by measuring the relative azimuthal angle $\Delta\Psi_2^{\rm FTPC} \equiv 2(\Psi_2^{\rm West} - \Psi_2^{\rm East})$. This is based on the assumption that there are no other correlations except flow effects. Taking into account that the multiplicity of the full event is twice as large as that of the sub-event, the full event plane resolution is given by Equation 4.14

$$\langle \cos[2(\Psi_2 - \Psi_r)] \rangle = \sqrt{2} \langle \cos[2(\Psi_2^A - \Psi_r)] \rangle. \tag{4.14}$$

Figure 4.11 shows the 2nd harmonic TPC and FTPC event plane resolution of v_2 determined in Au + Au collisions at $\sqrt{s_{NN}} = 200$ GeV for 9 different centrality intervals.

The TPC resolution of v_2 is pretty good, and it is 0.75 for mini-bias data (0-80%). While the FTPC resolution of v_2 is much smaller than TPC resolution, and it is about 0.185 for mini-bias data.

4.5 Invariant Mass Method

In this section, we present invariant mass method to extract v_2 for strange hadrons since we can not directly know whether a reconstructed strange hadron candidate belongs to signal or background. The result is also compared with event plane method.

By fitting the signal and background of strange hadrons, as shown in Fig. 4.7, we can get the signal counts in small phase space. For each transverse momentum (p_T) range, we divide the azimuthal space into 9 parts, and get the signal counts in each bin. Fig. 4.13 shows an example for K^0_S at $1.8 < p_T < 2.0$ for Au + Au collisions minbias (0-80%) data.

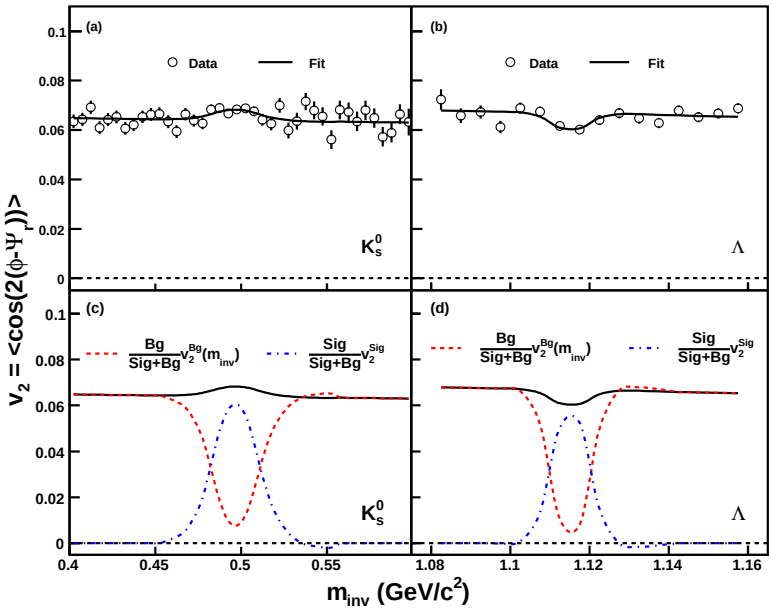

Figure 4.12: (a) K^0_S and (b) Λ candidates v_2 distributions at $1.6 < p_T < 1.8$ GeV/c for $0-80\%$ Au + Au collisions are shown. Red and blue curves refer to (c) signal and (d) background v_2 separately.

The essence of invariant mass method is based on the following Equation [**?**]:

$$v_2^{\mathrm{Sig+Bg}}(m_{\mathrm{inv}}) = v_2^{\mathrm{Sig}}\frac{\mathrm{Sig}}{\mathrm{Sig+Bg}}(m_{\mathrm{inv}}) + v_2^{\mathrm{Bg}}(m_{\mathrm{inv}})\frac{\mathrm{Bg}}{\mathrm{Sig+Bg}}(m_{\mathrm{inv}}). \tag{4.15}$$

The candidates v_2 is divided into two parts, one is the signal v_2 multiply the signal yields, and the other is the background v_2 multiply the background yields. We can get all the candidates v_2 after reconstructed event plane, which is the left side of the equation. And from the fitting shown in Fig. 4.7, we can get $\frac{\mathrm{Sig}}{\mathrm{Sig+Bg}}$ and $\frac{\mathrm{Bg}}{\mathrm{Sig+Bg}}$ ratio. If we assume that v_2^{Bg} is as a linear function of invariant mass (m_{inv}), we can extract v_2^{Sig} by fit with Equation 4.15.

To illustrate this method, Figure 4.12 shows an example for K_s^0 and Λ. Panel (a) and (b) show invariant mass distribution. A 4^{th} order polynomial fit to describe the background distribution is shown as solid line. $\frac{\mathrm{Bg}}{\mathrm{Sig+Bg}}(m_{\mathrm{inv}})$ is calculated by dividing fit line by data. $\frac{\mathrm{Sig}}{\mathrm{Sig+Bg}}$ is calculated by $(1 - \frac{\mathrm{Sig}}{\mathrm{Sig+Bg}})$. v_2 of K_S^0 candidates represented by open circles are calculated and plotted in panel (b). The fit to v_2 of K_S^0 candidates with Equation 4.15 is shown in solid line. The background contributions and the signal contributions are shown as dashed line and dot-dashed line in (c) along with the total fit.

The data points are fitted over a wide m_{inv} region. Data points which are far from the mass peak region come from background contributions, thus $\frac{\mathrm{Bg}}{\mathrm{Sig+Bg}}$ is equal to 1. $v_2^{\mathrm{Sig+Bg}}$ data points in this region have strong constraints on v_2^{Bg} when doing the fit. $v_2^{\mathrm{Sig+Bg}}$ data points in the mass region under peak constraint v_2^{Sig} with given $\frac{\mathrm{Sig}}{\mathrm{Sig+Bg}}$ and $\frac{\mathrm{Bg}}{\mathrm{Sig+Bg}}$ ratios. A large variation of v_2^{Sig} would lead to an strong disagreement of the fit curves with the measured data. Thus the shape of dip or bump of $v_2^{\mathrm{Sig+Bg}}$ in the mass region under peak is not necessary to measure v_2. The systematic uncertainty of this method lies in the estimate of $\frac{\mathrm{Sig}}{\mathrm{Sig+Bg}}$ and $\frac{\mathrm{Bg}}{\mathrm{Sig+Bg}}$ ratio as a function of m_{inv}. This systematic uncertainty is studied by using different functions to fit the background, which will be discussed in systematics section.

We can also use event plane method to get v_n^{obs} of V0. The azimuthal space with respect to event plane $(\phi - \Psi_2)$ is divided in to 9 bins, and the signal and background of V0 is fitted in each bin as shown in Fig. 4.7. By subtracting background, we can get the

signal counts in each bin. The observed v_2 and v_4 is extracted by fitting $dN/d(\phi - \Psi_2)$ distribution with Fourier expansion of azimuthal distribution

$$\frac{dN}{d(\phi - \Psi_2)} = N(1 + 2v_2^{\rm obs}\cos(2(\phi - \Psi_2)) + 2v_4^{\rm obs}\cos(4(\phi - \Psi_2))), \tag{4.16}$$

where N, $v_2^{\rm obs}$ and $v_4^{\rm obs}$ are free parameters. The fitting is shown as black curve in Fig. 4.13.

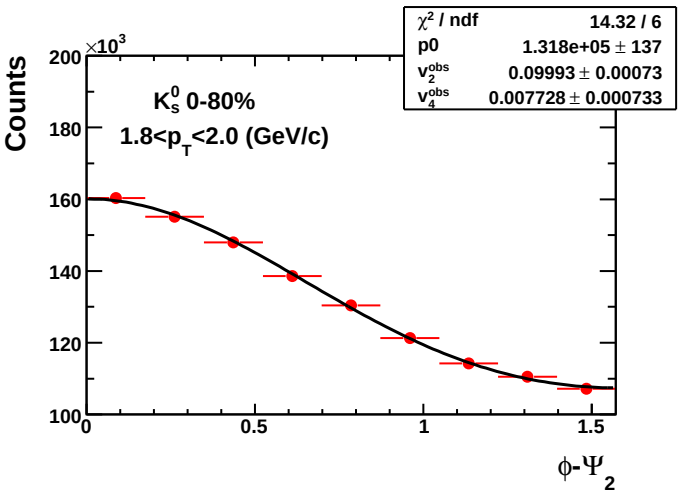

Figure 4.13: $dN/d(\phi - \Psi_2)$ distribution for K_S^0 at $1.8 < p_T < 2.0$ GeV/c for $0-80\%$ Au + Au collisions. Black curve is the fitting of data.

The observed $v_2^{\rm obs}$ ($v_4^{\rm obs}$) need to be corrected with event plane resolution by Eq. 4.12 for both of the methods.

4.6 Cumulant Method

In this section, we introduce the cumulant method which is base on a cumulant expansion of multi-particle azimuthal correlations.

4.6.1 Integral v_2

The principle of the cumulant method is that when cumulant of higher order is considered, the contribution of non-flow effects from lower order correlations will be eliminated.

In the following we take a four-particle correlations as an example to illustrate how this approach works.

Assuming a perfect detector, the measured two-particle correlations can be expressed as flow and non-flow components

$$\langle e^{in(\phi_1-\phi_2)}\rangle = \langle e^{in(\phi_1-\Psi_r)}\rangle\langle e^{in(\Psi_r-\phi_2)}\rangle + \delta_n = v_n^2 + \delta_n, \tag{4.17}$$

where n is the harmonic. The average is taken for all pairs of particles in a certain rapidity and transverse momentum region (typically corresponding to the acceptance of a detector) and for all events in a event sample. The δ_n denotes the non-flow contributions to two-particle correlation. The measured four-particle correlations can be decomposed as below:

$$\langle e^{in(\phi_1+\phi_2)-\phi_3-\phi_4}\rangle = v_n^4 + 2\cdot 2\cdot v_n^2\delta_n + 2\delta_n^2. \tag{4.18}$$

In this expression, two factors of "2" in front of the term $v_n^2\delta_n$ correspond to the two ways of pairing (1,3)(2,4) and (1,4)(2,3) and account for the possibility to have non-flow effects in the first pair and flow in the second pair or vice versa. The factor "2" in front of δ_n^2 is from two ways of airing. The four-particle non-flow correlation is omitted in the expression.

From this it follows that the flow contribution can be obtained by subtracting the two-particle correlation from the four-particle correlation:

$$\langle\langle e^{in(\phi_1+\phi_2)-\phi_3-\phi_4}\rangle\rangle = \langle e^{in(\phi_1+\phi_2)-\phi_3-\phi_4}\rangle - 2\langle e^{in(\phi_1-\phi_3)}\rangle^2 = -v_n^4, \tag{4.19}$$

where the notation $\langle\langle\cdots\rangle\rangle$ is used for the cumulant. The cumulant of order two is just $\langle\langle e^{in(\phi_1-\phi_2)}\rangle\rangle = \langle e^{in(\phi_1-\phi_2)}\rangle$.

In practice, the various quantities of interest are constructed from the real-valued generating function

$$\begin{aligned} G_n(z) &= \prod_{j=1}^{M}[1 + \frac{w_j}{M}(z^* e^{in\phi_j} + z^* e^{-in\phi_j})] \\ &= \prod_{j=1}^{M}[1 + \frac{w_j}{M}(2x\cos(n\phi_j) + 2y\sin(n\phi_j))], \end{aligned} \tag{4.20}$$

where the product runs over M particles detected in a single event and $z = x + iy$ is an arbitrary complex number. This generating function has no physical meaning in itself, but after averaging over events, the coefficients of its expansion in powers of z and $z^* \equiv x - iy$ yield multiparticle azimuthal correlations of arbitrary orders.

In order to obtain the cumulants, one first averages $G_n(z)$ over events, which yields an average generating function $\langle G_n(z)\rangle$, we define

$$C_n(z) \equiv M[\langle G_n(z)\rangle^{1/M} - 1]. \tag{4.21}$$

The cumulant of 2k-particle correlations $c_n\{2k\}$ is the coefficient of $z^k z^{*k}/(k!)^2$ in the power-series expansion of $C_n(z)$.Once the values $C_n(z_{p,q})$ have been computed, they must be averaged over the phase of z:

$$C_p \equiv \frac{1}{q_{max}} \sum_{q=0}^{q_{max}-1} C_n(z_{p,q}), \quad p = 1, 2, 3. \tag{4.22}$$

The cumulants of 2-, 4- and 6-particle correlation are then give respectively by

$$\begin{aligned} c_n\{2\} &= \frac{1}{r_0^2}(3C_1 - \frac{3}{2}C_2 + \frac{1}{3}C_3), \\ c_n\{4\} &= \frac{2}{r_0^4}(-5C_1 - 4C_2 - C_3), \\ c_n\{6\} &= \frac{6}{r_0^6}(3C_1 - 3C_2 + C_3). \end{aligned} \tag{4.23}$$

From the measured $c_n\{2k\}$, we can obtain an estimate of the integral flow, which is denoted by $V_n\{2k\}$:

$$\begin{aligned} V_n\{2\}^2 &= c_n\{2\}, \\ V_n\{4\}^2 &= -c_n\{4\}, \\ V_n\{6\}^2 &= c_n\{6\}/4. \end{aligned} \tag{4.24}$$

Given an estimate of the n^{th} order integrated flow V_n, the estimate of differential flow v_p' (flow in a restricted phase-space window) in any harmonic $p = mn$, where m in an integer. For instance, the 4^{th} order differential flow v_4' can be analyzed using the integrated V_1, V_2, V_3 and V_4 as reference.

4.6.2 Differential v_2

The generating function of the cumulants for studying differential flow is given by

$$D_{p/n}(z) - \frac{e^{ip\psi G_n(z)}}{\langle G_n(z)\rangle}, \tag{4.25}$$

where ψ refers to the azimuth of the particle of interest. In the numerator, the average is performed over all particles of interest. On the other hand, the denominator is averaged over all events. Following the same procedure as in the case of the integrated flow, the cumulant $d_p\{2k+m+1\}$ involving $2k+m+1$ particles is computed. After this the differential flow $v'_p\{2k+m+1\}$ is estimated.

For instance, the differential flow estimated from the lowest order cumulant is shown for two cases($m=1$ or $m=2$):

$$\begin{aligned} v'_{n/n}\{2\} &= d_{n/n}\{2\}/V_n, & v'_{n/n}\{4\} &= d_{n/n}\{4\}/V_n^3, \\ v'_{2n/n}\{3\} &= d_{2n/n}\{3\}/V_n^2, & v'_{2n/n}\{5\} &= -d_{2n/n}\{5\}/2V_n^4, \end{aligned} \tag{4.26}$$

The advantage of the generating functions is that they automatically involve all possible k particle correlations when building the k-particle cumulants. Moreover, the formalism removes the non-flow correlations arising from detector inefficiencies. However, in practice, the use of higher order cumulants is often limited by statistics.

4.7 Mixed Harmonics method

An event plane determined from harmonic m can be used to study the flow of harmonics $n = km$, where k is an integer. The case of $k > 1$ is called the mixed harmonics method. This method allow us to choose biggest flow signal with largest resolution to reconstruct event plane according to the detectors. At the AGS and SPS, the fixed target setting the detectors usually cover well the region of rapidity where directed flow is large. While at RHIC, we mostly use the method to study higher ($n \geq 4$) harmonics relative to elliptic flow since it is so strong near midrapidity.

Higher order Fourier coefficient v_4 is expected to become as large as 5% and should be clearly measurable. We used both TPC event plane method and FTPC event plane

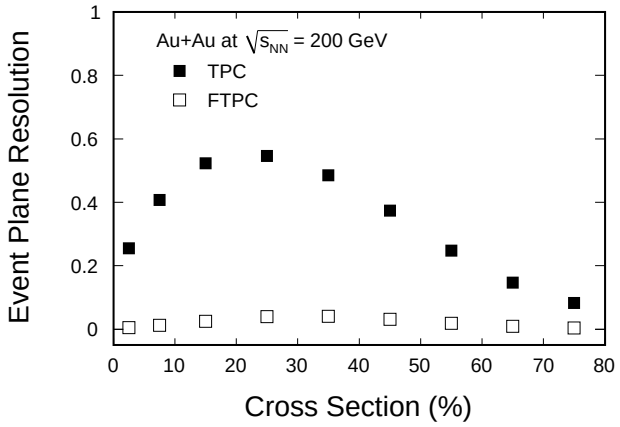

Figure 4.14: The 2$^{\text{nd}}$ order TPC event plane resolution and FTPC event plane resolution for v_4 in Au + Au collisions at $\sqrt{s_{NN}} = 200$ GeV for 9 different centrality intervals.

method to measure v_4. Figure 4.14 shows the 2$^{\text{nd}}$ harmonic TPC event plane resolution and FTPC event plane resolution of v_4 determined in Au + Au collisions at $\sqrt{s_{NN}} = 200$ GeV for 9 different centrality intervals. The TPC resolution of v_4 is pretty good, and it is 0.42 for mini-bias data (0-80%). While the FTPC resolution of v_4 is much smaller than TPC resolution, and it is about 0.023 for mini-bias data.

CHAPTER 5

Results I: Transverse azimuthal anisotropy

In this chapter, we present the result of elliptic flow v_2 and the higher harmonic v_4 in Au + Au collisions at $\sqrt{s_{NN}} = 200$ GeV. The results from TPC event plane method, FTPC event plane method and four-particle cumulant method are compared. Dependences of the flow coefficients on transverse momentum, centrality and particle species are also presented.

5.1 Elliptic flow v_2

5.1.1 Centrality dependence and non-flow effect

Elliptic flow, v_2, has been measured by different methods [**?**]. The previous study [**?**] shows that the major systematic uncertainty of v_2 measurement is the non-flow effect which has nothing to do with reaction plane, i.e., HBT, jet, resonance decay, etc. Therefore, it is important to study the non-flow effect to precise the measurement for flow study.

Here, the charged particle v_2 is calculated by TPC event plane method, FTPC event plane method and four-particle cumulant method. With large statistic data sample obtained in Au+Au collisions at $\sqrt{s_{NN}} = 200$ GeV during RHIC Run VII, anisotropic flow coefficients can be measured to higher p_T range for different centralities.

Figure 5.1 shows charged particle v_2 in centrality $20\% - 60\%$ at mid-rapidity ($|\eta| < 1$) for Au + Au collisions at $\sqrt{s_{NN}} = 200$ GeV as a function of transverse momentum p_T. The error bars are statistical only. The v_2 values are obtained with the TPC event plane

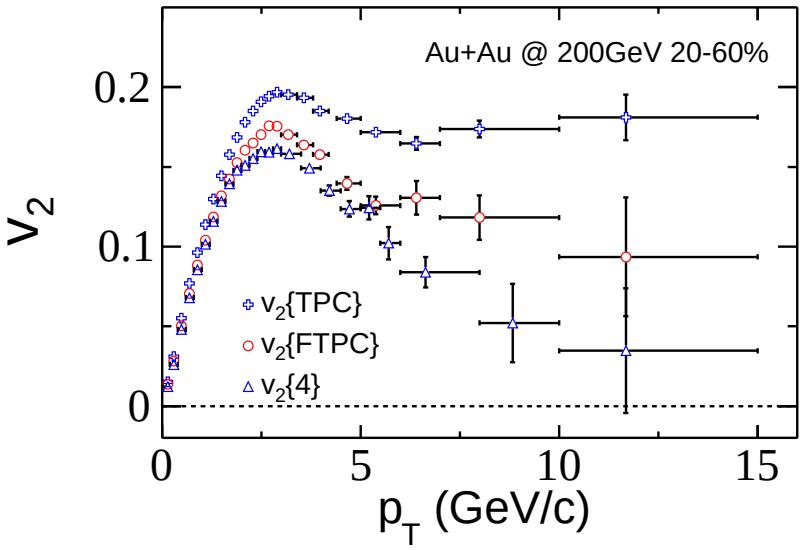

Figure 5.1: Charged particle elliptic flow (v_2) as a function of transverse momentum (p_T) for centrality $20\% - 60\%$ in Au + Au collisions at $\sqrt{s_{NN}} = 200$ GeV from the TPC event plane method (crosses), FTPC event plane method (circles) and four-particle cumulant method (triangles).

method (denoted by $v_2\{\text{TPC}\}$), FTPC event plane method (denoted by $v_2\{\text{FTPC}\}$) and four-particle cumulant method (denoted by $v_2\{4\}$). A systematic difference is observed for the values obtained from the three methods, especially between the TPC event plane method and four-particle cumulant method. v_2 obtained from TPC event plane method which includes non-flow effect shows the biggest value compared with other methods. v_2 obtained from FTPC event plane method, in which non-flow effect can be significant reduced by the large η gap, shows smaller value than $v_2\{\text{TPC}\}$. $v_2\{4\}$ can be considered as lowest bound of v_2 since it is not sensitive to non-flow and flow fluctuation. There are also some differences between $v_2\{\text{FTPC}\}$ and $v_2\{4\}$, which may caused by both non-flow effect and v_2 fluctuation [**?**]. It is clear that the difference increases with transverse momentum, and it is significant when p_T is larger than 3 GeV/c, where non-flow effect plays an important role.

The plot shows that v_2 firstly increases with p_T, then begins decreasing after gets the maximum value at about 3 GeV/c. At low p_T region, v_2 can be well described by

hydrodynamics [?, ?]. However, the data starts to deviate from ideal hydrodynamics at about 1 GeV/c. The position of the onset of the deviation from ideal hydrodynamics and its magnitude are thought to constrain the shear viscosity of the fluid [?]. Particle production at $p_T > 2$ GeV/c will be dominated by hard or semi-hard process. It is believed that fragmentation of high energy partons (jets) coming from initial hard scattering begins to dominate the particle production. Perturbative calculation predicts that high energy partons traversing nuclear matter lose energy through induced gluon radiation [?]. The energy loss called "jet quenching" is expected to depend strongly on the color charge density of the created system and the transversed path length of the propagating parton. In non-central collisions, the initial geometry of the overlap region has an almond shape as shown in Fig. 2.4. Partons emit to different directions may experience different path lengths and therefore different energy loss. And this will cause azimuthal anisotropy in the hadron production. Thus, the turning point of v_2 signals the onset of contribution of hard processes and the magnitude of parton energy loss [?, ?]. Being consistent with scenario of parton energy loss [?], the estimated elliptic flow from the four-particle cumulant method, which is not sensitive to non-flow effect, shows a decreasing trend at high p_T and it is sizable up to 10 GeV/c.

Figure 5.2 shows charged v_2 as a function of p_T for centrality $70\% - 80\%$, $60\% - 70\%$, $50\% - 60\%$, $40\% - 50\%$, $30\% - 40\%$, $20\% - 30\%$, $10\% - 20\%$, $5\% - 10\%$ and $0 - 5\%$ in Au + Au collisions at $\sqrt{s_{NN}} = 200$ GeV. As before, v_2 obtained from the TPC event plane method (crosses), FTPC event plane method (circles) and four-particle cumulant method (triangles) are compared. As p_T increases, $v_2\{\text{TPC}\}$ continues increasing in most peripheral collisions, i.e., centrality $70\% - 80\%$ and $60\% - 70\%$, while it reaches the maximum value at 3 GeV/c in other centralities. $v_2\{\text{FTPC}\}$ and $v_2\{4\}$ have similar trend except the most central collisions, i.e., $0 - 5\%$. We failed to get the value of $v_2\{4\}$ in most central collisions because $2\langle(v_2)^2\rangle^2 - \langle(v_2)^4\rangle$ is negative. This indicates that $\langle(v_2)^4\rangle/\langle(v_2)^2\rangle^2 > 2$. It is suggested that if $2\langle(v_2)^2\rangle^2 - \langle(v_2)^4\rangle$ is scaled by $v_2\{2\}^4$, the ratio should be around -1, if $\langle(v_2)^4\rangle/\langle(v_2)^2\rangle^2 \simeq 3$. This would give invaluable information on the mechanism driving elliptic flow fluctuations.

Comparing v_2 obtained from different methods, we can see that the non-flow effect

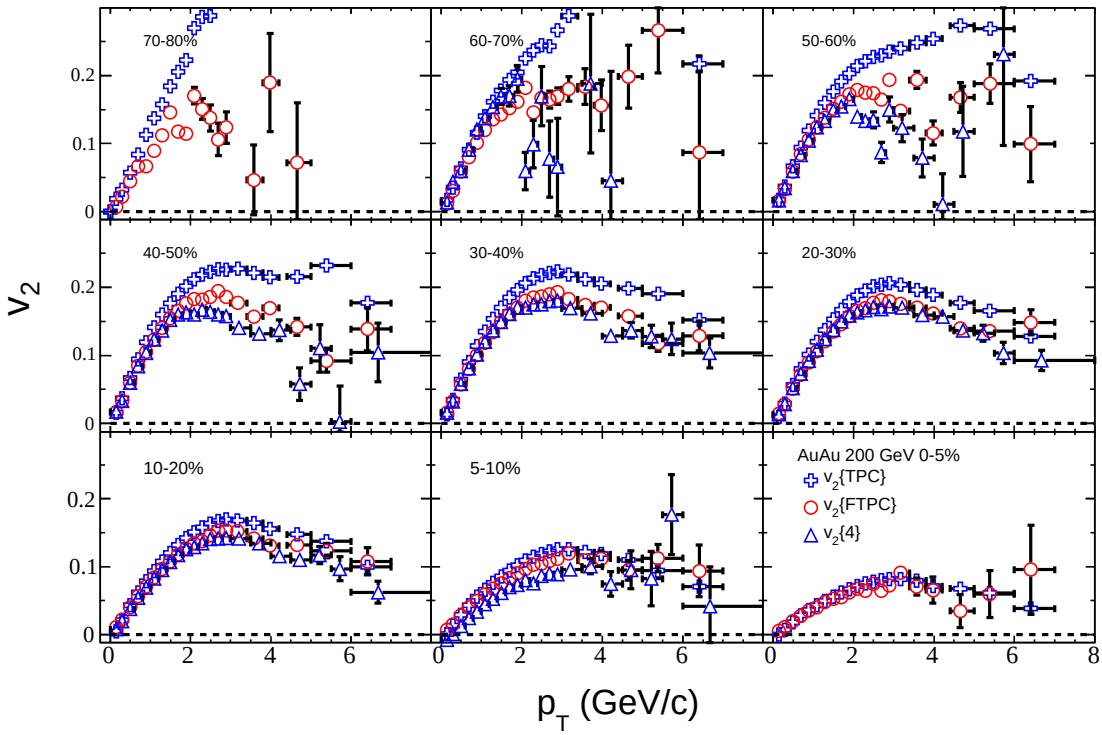

Figure 5.2: Charged particle elliptic flow (v_2) as a function of transverse momentum (p_T) for centrality $70\% - 80\%$, $60\% - 70\%$, $50\% - 60\%$, $40\% - 50\%$, $30\% - 40\%$, $20\% - 30\%$, $10\% - 20\%$, $5\% - 10\%$ and $0 - 5\%$ in Au + Au collisions at $\sqrt{s_{NN}} = 200$ GeV from the TPC event plane method (crosses), FTPC event plane method (circles) and four-particle cumulant method (triangles).

is significant in high p_T region than in low p_T region. And in different centralities, the non-flow effect is more important in peripheral collisions than in central collisions.

5.1.2 Particle species dependence

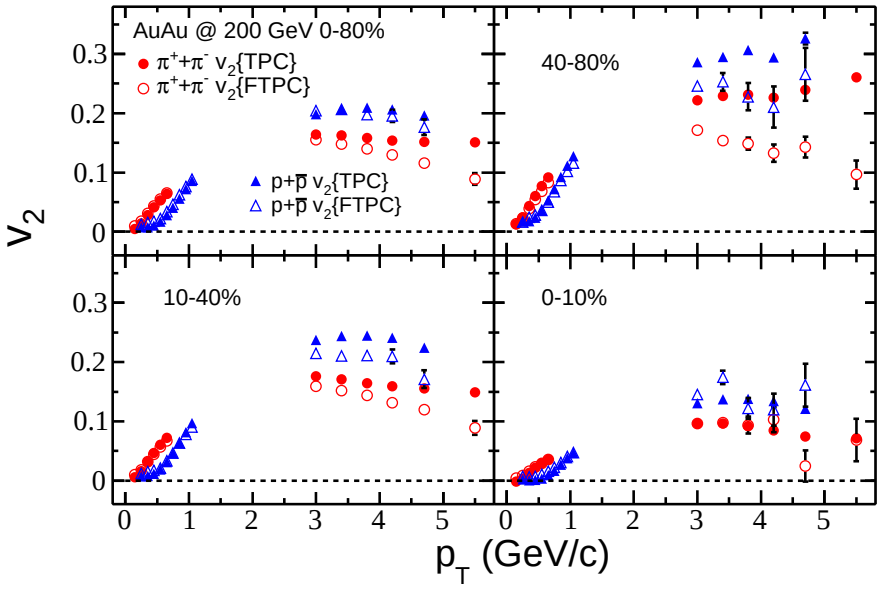

Figure 5.3: Charged pions and (anti)protons v_2 as a function of p_T for centrality $0-80\%$, $40\%-80\%$, $10\%-40\%$ and $0-10\%$ in Au + Au collisions at $\sqrt{s_{NN}} = 200$ GeV. Solid points are the results from TPC event plane while open points are the results from FTPC event plane.

Figure 5.3 shows v_2 of charged pions and (anti)protons as a function of p_T in centrality bins $0-80\%$, $40\%-80\%$, $10\%-40\%$ and $0-10\%$ in Au + Au collisions at $\sqrt{s_{NN}} = 200$ GeV, and the errors are statistical only. In $p_T < 1$ GeV/c region, v_2 of (anti)proton is smaller than v_2 of pion which can be explained by hydrodynamics. The collective radial motion boosts particles to higher average momenta, heavier particles gain more momentum than lighter ones. This leads to a flattening of the spectra at low transverse momenta. This flattening reduces v_2 at low p_T, and therefore the heavier the particle the more the rise of $v_2(p_T)$ is shifted towards at larger p_T [?]. While in large p_T region, v_2 of proton is larger than v_2 of pion which can be explained by coalescence or recombination model [?, ?, ?, ?]. In those models, hadron v_2 (v_2^h)at intermediate p_T ($2 < p_T < 5$ GeV/c)

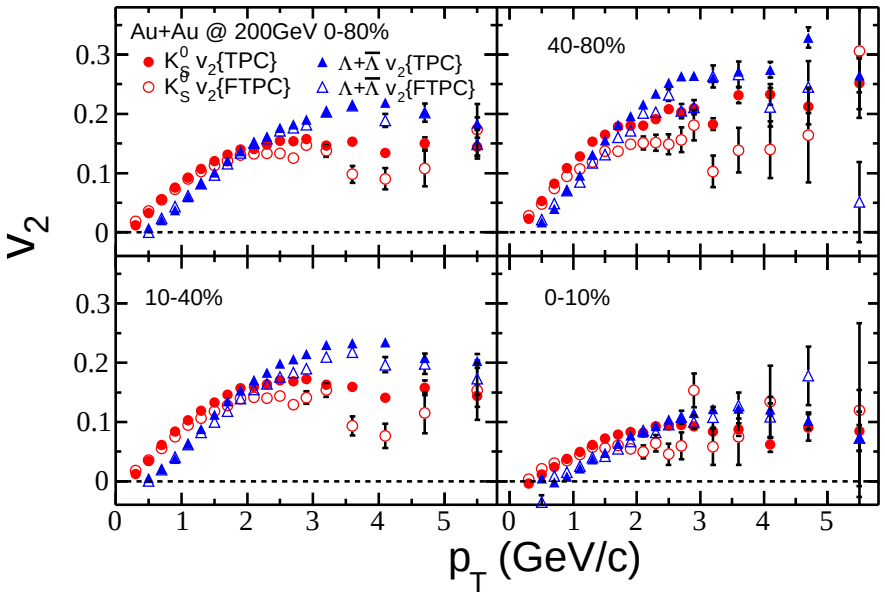

Figure 5.4: K^0_S and Λ v_2 as a function of p_T for centrality $0-80\%$, $40\%-80\%$, $10\%-40\%$ and $0-10\%$ in Au + Au collisions at $\sqrt{s_{NN}} = 200$ GeV. Solid points are the results from TPC event plane while open points are the results from FTPC event plane.

is related to the v_2 of quarks v_2^q in QGP by the relationship: $v_2^h(p_T) \approx n_q v_2^q(p_T/n_q)$.

Also, the v_2 values from from the TPC event plane method and FTPC event plane method are compared. It is clear that FTPC result is significant smaller than TPC result in high p_T region, because FTPC can reduce the non-flow effect by large η gap. And the non-flow effect is larger in peripheral collisions than in central collisions for both charged pions and (anti)protons.

Figure 5.4 shows v_2 of K^0_S and Λ as a function of p_T in centrality bins $0-80\%$, $40\%-80\%$, $10\%-40\%$ and $0-10\%$ in Au + Au collisions at $\sqrt{s_{NN}} = 200$ GeV. The mass ordering is also observed at low p_T, while v_2 of Λ is larger than v_2 of K^0_S at intermediate and high p_T range. The v_2 values from from the TPC event plane method and FTPC event plane method are compared. It is clear that FTPC result is significant smaller than TPC result in high p_T region since the non-flow effect is reduced by large η gap between two FTPCs. And the non-flow effect is larger in peripheral collisions than in central collisions for both K^0_S and Λ.

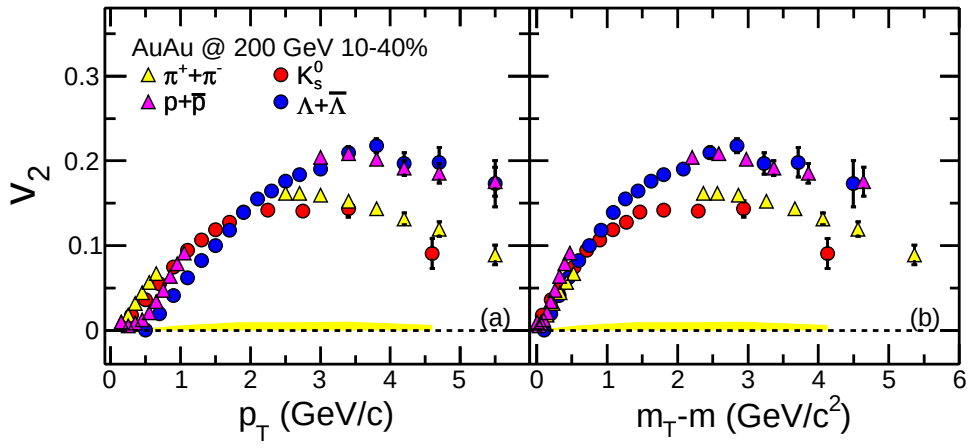

Figure 5.5: v_2 of $\pi^{\pm}$ (solid triangle), p ($\bar{p}$) (solid circle), K^0_S (open triangle) and $\Lambda(\bar{\Lambda})$ (open circle) with FTPC event plane for centrality $10-40\%$ in Au + Au collisions at $\sqrt{s_{NN}} = 200$ GeV. The errors are statistical only, and the systematic uncertainty of nonflow is shown as shaded band at bottom.

The results for $\pi^{\pm}$, p ($\bar{p}$), K^0_S and Λ ($\bar{\Lambda}$) at mid(pseudo)rapidity $|\eta| < 1$ are shown in Fig. 5.5 for $10-40\%$ centrality. At low p_T, the hadron mass ordering of v_2 (for a given p_T , the heavier the hadron, the smaller v_2) is observed (left panel). During the process of a hydrodynamic expansion, the radial flow plays an important role [**?**], and the pressure gradient that drives elliptic flow is directly linked to the collective kinetic energy of the emitted particles. Thus one expects v_2 for different particle species should scale with $m_T - m$ [**?**], where $m_T = \sqrt{m^2 + p_T^2}$. Following [**?**], in the right panel we present v_2 as a function of $m_T - m$. Good scaling is observed up to $m_T - m = 1$ GeV/c^2, beyond that, v_2 of different particles becomes diverged. Noticeably, v_2 from all particles species showing signs of decrease after reaching their maximum around $2 - 2.5$ GeV/c^2 in $m_T - m$. It is argued that jet conversion may cause a large number of extra strange quarks to be produced throughout the out-of-plane direction, thus the v_2 of kaons is systematically smaller than v_2 of pions and the difference between strange and non-strange baryons is much smaller than that between strange and non-strange mesons [**?**]. However, we can not get the conclusion due to the large statistic errors of identified particles v_2 at large p_T for this dataset.

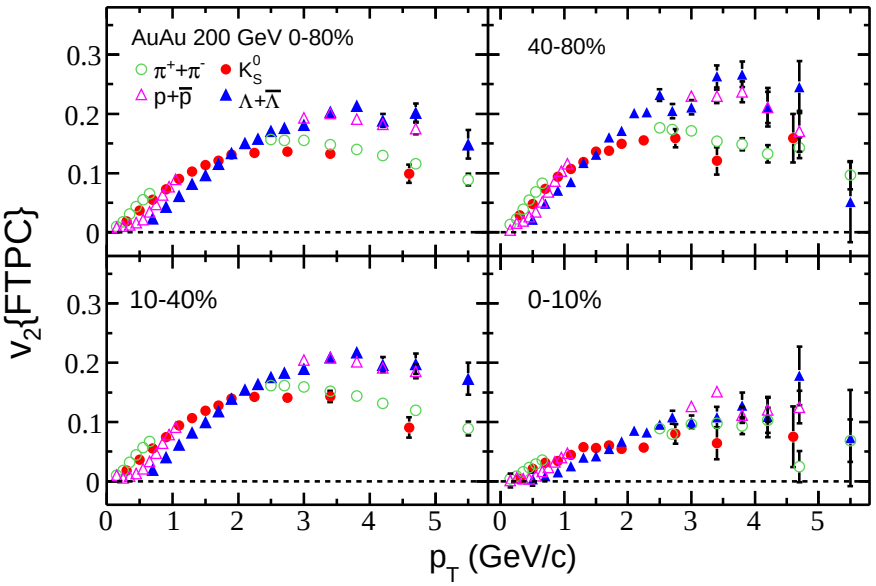

Figure 5.6: Charged pions (open triangles), (anti)protons (solid triangles), K^0_S (open circles) and Λ (solid circles) v_2 from FTPC event plane as a function of p_T for centrality $0-80\%$, $40\%-80\%$, $10\%-40\%$ and $0-10\%$ in Au + Au collisions at $\sqrt{s_{NN}} = 200$ GeV.

The major systematic uncertainty in this analysis comes from "nonflow", which are correlations not related to reaction plane. We take advantage of the large η gap between the two FTPCs to reduce the short-range correlations between particles interest and particles used to reconstruct the event plane. The remaining nonflow correlations, along with event-by-event flow fluctuations, are estimated by the difference between v_2 obtained from FTPC event plane (v_2\{FTPC\}) and v_2 obtained from the multi-particle cumulant method (v_2\{LYZ\}). The Lee-Yang Zero method is supposed to suppress the known non-flow effects such as jets, resonances [**?**]. However, the Lee-Yang Zero method yields larger statistical errors [**?**]. Such nonflow effect is about 7% of v_2 value for strange hadrons as shown by shaded band at the bottom. Our estimation of systematic error stops at $m_T - m = 3$ GeV/c^2, because v_2\{LYZ\} analysis is more statistics hungry and cannot reach the same p_T as that reached by v_2\{FTPC\} method.

Figure 5.6 shows all the identified particles v_2 (Charged pions (open triangles), (anti)protons (solid triangles), K^0_S (open circles) and Λ (solid circles)) from FTPC event

plane as a function of transverse momentum (p_T) for centrality $0-80\%$, $40\%-80\%$, $10\%-40\%$ and $0-10\%$ in Au + Au collisions at $\sqrt{s_{NN}} = 200$ GeV.

5.1.3 Number of constituent quark scaling of v_2

One of the major findings from previous studies is that, at intermediate p_T (from $p_T \sim 1.5$ GeV/c to roughly 4 -5 GeV/c), baryon and meson elliptic flow, if scaled by their corresponding number of constituent quarks (n_q) and plotted against (p_T/n_q), converges. It is so called the Number of Constituent Quark (NCQ) scaling, and it implies that hadrons are produced out of a deconfined partonic state by coalescence [**?**, **?**] or recombination [**?**]. More importantly, as underlying quark flow is needed to explain the data, it provides the strongest evidence for the partonic collectivity.

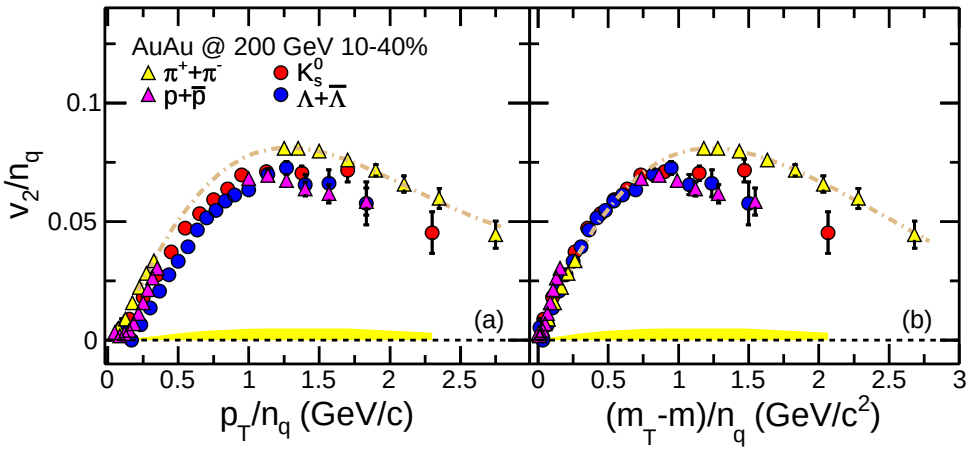

Figure 5.7: The v_2/n_q of charged pions (open triangles), (anti)protons (solid triangles), K^0_S (open circles) and Λ (solid circles)from FTPC event plane as a function of p_T/n_q for centrality $0-80\%$, $40\%-80\%$, $10\%-40\%$ and $0-10\%$ in Au + Au collisions at $\sqrt{s_{NN}} = 200$ GeV.

It is expected that such scaling will eventually break down at large p_T, at which the hard process begin to kick in and particles are no longer produced by quark coalescence. Thus it is desirable to locate the p_T range where it starts to break down – that will allow us to understand the transition of particle production mechanisms. It is as well important to examine the pattern with which the NCQ scaling breaks for various hadrons. Such pattern will not only shed a light on the dynamics of jet fragmentation, it will also,

being served as a counter example of NCQ scaling, deepen our understanding of quark coalescence.

In order to test the NCQ scaling at large p_T, we plot v_2/n_q as a function of p_T/n_q and $(m_T - m)/n_q$ in Figure 5.7 in centrality $10\% - 40\%$ in Au + Au collisions at $\sqrt{s_{NN}} = 200$ GeV. The latter works at low p_T because the mass effect has been taken into account. The remaining systematical error in $v_2\{\text{FTPC}\}$, which is common for different particle species, is represented by the shaded band at bottom. This error is estimated by studying the difference between $v_2\{\text{FTPC}\}$ and $v_2\{\text{LYZ}\}$ for reconstructed particles K^0_S and Λ ($\bar{\Lambda}$). Since we can not identify charged pions at intermediate p_T, a phenomenologically motivated function [**?**]

$$v_2/n_q = \frac{a + bx + cx^2}{1 + \exp[\frac{-(x-d)}{e}]} - \frac{a}{2} \tag{5.1}$$

is used to fit the v_2 of pions. Here x refers to p_T/n_q or $(m_T - m)/n_q$. There is no physical meaning to the function or the five fit parameters but simply be used as a convenient reference.

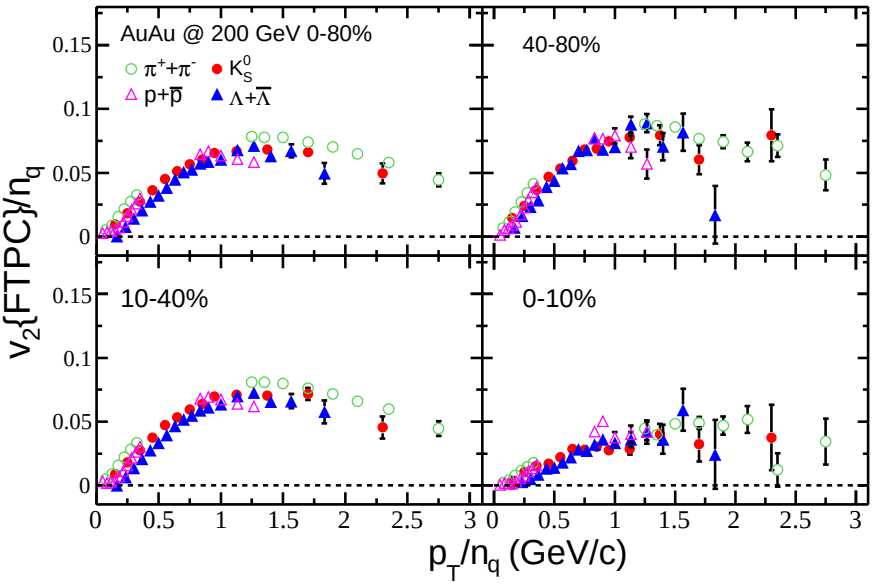

Figure 5.8: The v_2/n_q of charged pions (open triangles), (anti)protons (solid triangles), K^0_S (open circles) and Λ (solid circles)from FTPC event plane as a function of p_T/n_q for centrality $0 - 80\%$, $40\% - 80\%$, $10\% - 40\%$ and $0 - 10\%$ in Au + Au collisions at $\sqrt{s_{NN}} = 200$ GeV.

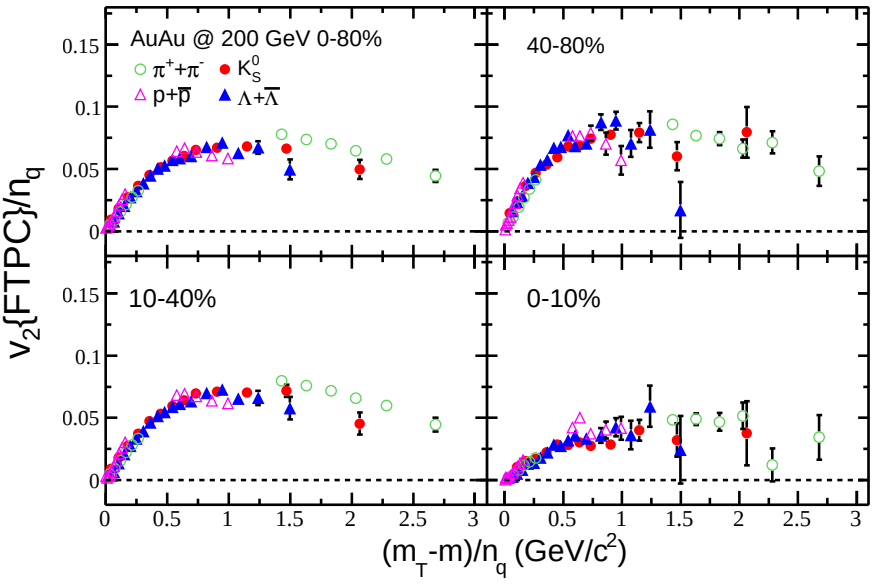

Figure 5.9: The v_2/n_q of charged pions, (anti)protons, K^0_S and Λ from FTPC event plane as a function of $(m_T - m)/n_q$ for centrality $0-80\%$, $40\%-80\%$, $10\%-40\%$ and $0-10\%$ in Au + Au collisions at $\sqrt{s_{NN}} = 200$ GeV.

The plot shows that NCQ scaling works well at low p_T range, while the scaling breaks down at $(m_T - m)/n_q > 1$ GeV/c^2. It seems that baryons and mesons follow their own group again after break down for $(m_T - m)/n_q > 2$ GeV/c, however considering the errors from our current measurements we cannot make a definite conclusion.

The centrality dependence of NCQ scaling is plotted in Fig. 5.10 and Fig. 5.9 as function of p_T/n_q and $(m_T - m)/n_q$, respectively. From the plot we can see that, at intermediate p_T range, NCQ scaling works well for all the centralities. However, due to the large statistical errors of the dataset, the breaking of NCQ scaling is inconclusive for most central and most peripheral collisions.

To quantify the divergence from NCQ scaling, in Fig. 5.10 we present the difference between v_2/n_q for baryons and mesons, then divided by their average: ((B - M)/(B + M)/2). The deviation of v_2/n_q for lambda (proton) from the fitted formula of pions as shown in Fig. 5.10 is calculated point by point, and scaled by the sum of v_2/n_q of lambda (proton) and the corresponding value from the fitted formula as a function of

(a) p_T/n_q and (c) $(m_T - m)/n_q$. The deviation is about 20% from 0.5 up to $p_T/n_q \simeq 1.5$ GeV/c, while it is close to 0 from 0.5 up to $m_T - m \simeq 1$ GeV/c^2. Although the statistical error is large, we still can see the decreasing trend of data as p_T increases. The similar calculation is done with kaon as a reference in Fig. 5.10(b) and (d); similar trend but smaller difference between baryons and kaons is observed. The shaded boxes are the systematic uncertainty due to nonflow, which is mostly canceled in the numerator but is enhanced in the denominator, thus the magnitude of the ratio would be even larger if the nonflow could be completely removed. Note that NCQ scaling is not expected to be a perfect scaling, as evidence by 5% from zero for models that take account realistic effects. However, our data shows much larger deviation than this value for the pions. This indicates that further theoretical work is needed in order to understand the details of the species dependence of v_2 at intermediate p_T.

Model predictions are also shown in the plot for comparison. Two of these models attempt to improve the naive NCQ scaling by introduction of realistic effects. The model that takes into account finite width in the hadron wave function [**?**] describes the data reasonably well in the region $0.5 < p_T/n_q < 1.5$ GeV/c when compared with kaons (panel (b)), but not as well when pions are chosen to represent the mesons (panel (a)). The model that adds sea quarks and gluons to the hadron structure is also shown. In this model, the lowest fock state [**?**] refers to the recombination of constituent quarks $|q\bar{q}\rangle$ or $|qqq\rangle$ only, while higher fock states ($C_2 = 0.3$) refers to moderate $|q\bar{q}g\rangle$ or $|qqqg\rangle$ contribution. The ratio of this model is slightly larger than data points. Both of the two models try to improve the naive NCQ scaling at intermediate p_T, and they are not expected to explain the difference at large p_T, as seen in this plot. A similar difference between data and models is observed (lower panels) if we assume mesons and baryons to be pions and protons (lambdas) and plotted as a function of $(m_T - m)/n_q$, respectively, in these two models. The model that includes a resonance decay effect [**?**] describes data slightly better than other models in the low p_T region, and beyond that region, it gives almost identical results as that given by the same model without resonance decay effect. This is understood as that the resonance effect is mostly relevant at low p_T [**?**].

In Fig. 5.10, we also compare our data with models predicting NCQ violation at

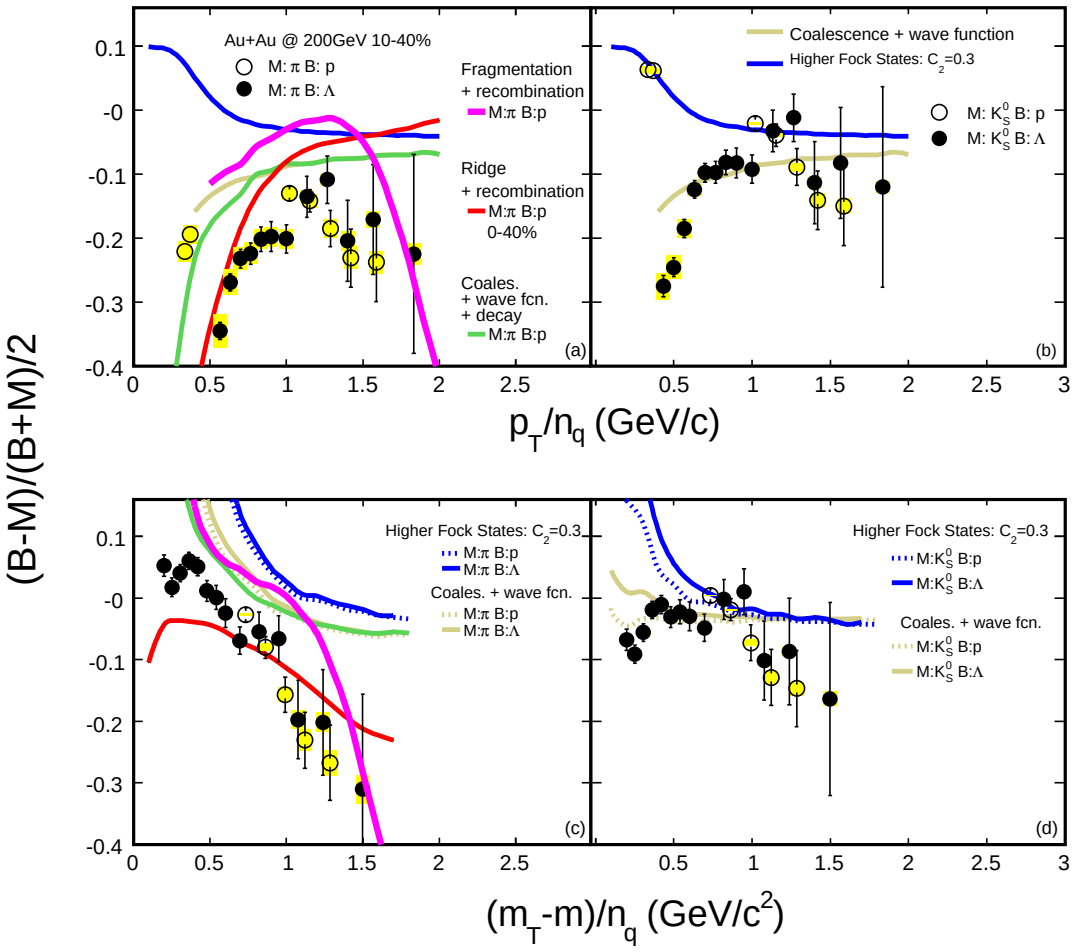

Figure 5.10: The v_2/n_q of charged pions (open triangles), (anti)protons (solid triangles), K^0_S (open circles) and Λ (solid circles)from FTPC event plane as a function of p_T/n_q for centrality $0-80\%$, $40\%-80\%$, $10\%-40\%$ and $0-10\%$ in Au + Au collisions at $\sqrt{s_{NN}} = 200$ GeV.

large p_T. In the Ridge + recombination model [?], partons are divided into two groups: soft thermal partons and shower partons created by hard partons. The formation of ridges due to weak jets will affect the azimuthal distribution, thus in the range from intermediate to large p_T, the thermal and shower partons contribute to v_2 differently which will cause the breaking of NCQ scaling. This effect looks prominent if viewed with $(m_T - m)/n_q$ but much less significant with p_T/n_q. The p_T/n_q is believed to be a more relevant quantity to address the NCQ scaling, and has been used in most of coalescence models [?, ?, ?, ?]. Our analysis illustrates that the choice of $m_T - m$ versus p_T can change the conclusions drawn from a study of NCQ scaling. In the Fragmentation + Recombination model [?], the competition between recombination of thermalized partons and fragmentation from perturbatively scattered partons is discussed. A violation of NCQ scaling is predicted coming from the perturbative QCD. It shows a decreasing trend for both p_T/n_q and $(m_T - m)/n_q$. From the model discussions above, only the Fragmentation + Recombination model can explain the trend, as well as the magnitude, at large p_T/n_q and $(m_T - m)/n_q$ which may indicate that the hard process is the most responsible cause for the possible deviation from NCQ scaling for this region.

5.2 The 4^{th} harmonic v_4

5.2.1 Centrality dependence and non-flow effect

Higher order Fourier coefficient v_4 is consider to be significant for intermediate to large transverse momenta. To study the non-flow effect on $v-4$, the charged particle v_4 is calculated by both TPC event plane method and FTPC event plane method.

Figure 5.11 shows charged particle v_4 in centrality $0-80\%$ at mid-rapidity ($|\eta| < 1$) for Au + Au collisions at $\sqrt{s_{NN}} = 200$ GeV as a function of transverse momentum p_T. Here the 2^{nd} harmonic reconstructed the event plane is used. The so-called "mixed-harmonic" method can reduce the non-flow effect. The v_4 values obtained from the TPC event plane method (denoted by $v_4\{\text{TPC}\}$) and FTPC event plane method (denoted by $v_4\{\text{FTPC}\}$) are compared. v_4 increases with p_T until about 3 GeV/c, and then decreases

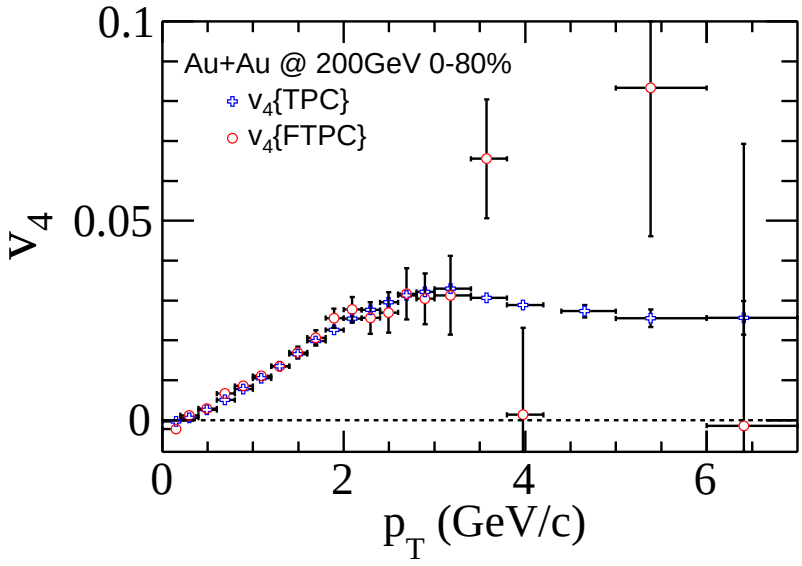

Figure 5.11: Charged particle v_4 as a function of transverse momentum (p_T) for centrality $0-80\%$ in Au + Au collisions at $\sqrt{s_{NN}} = 200$ GeV from the TPC event plane method (crosses) and FTPC event plane method (circles).

a little bit at intermediate and high p_T region. No significant difference is observed between $v_4\{\text{TPC}\}$ and $v_4\{\text{FTPC}\}$ for p_T lower than 3 GeV/c region since some of the non-flow effects are removed by mixed-harmonic method and is not significant for low p_T region. The low FTPC v_4 resolution as shown in Fig 4.14 causes large errors for $v_4\{\text{FTPC}\}$. Therefore, the non-flow effect is inconclusive at high p_T region due to the errors.

Figure 5.12 shows charged particle v_4 as a function of transverse momentum (p_T) for centrality $70-80\%$, $60-70\%$, $50-60\%$, $40-50\%$, $30-40\%$, $20-30\%$, $10-20\%$, $5-10\%$ and $0-5\%$ in Au + Au collisions at $\sqrt{s_{NN}} = 200$ GeV. As before, v_4 is obtained from the TPC event plane method (crosses) and FTPC event plane method (circles). We can see that the centrality dependence of v_4 is quite similar as that of v_2. For peripheral collisions, as centrality $70\%-80\%$ and $60\%-70\%$, $v_4\{\text{TPC}\}$ continues increasing which may caused by non-flow effect or v_4 fluctuation. While for other centralities, v_4 gets maximum value and begins to decrease at about at 3 GeV/c. By comparing the v_4 values in mid-central centralities, i.e., $40-50\%$, $30-40\%$, $20-30\%$, we can also see that

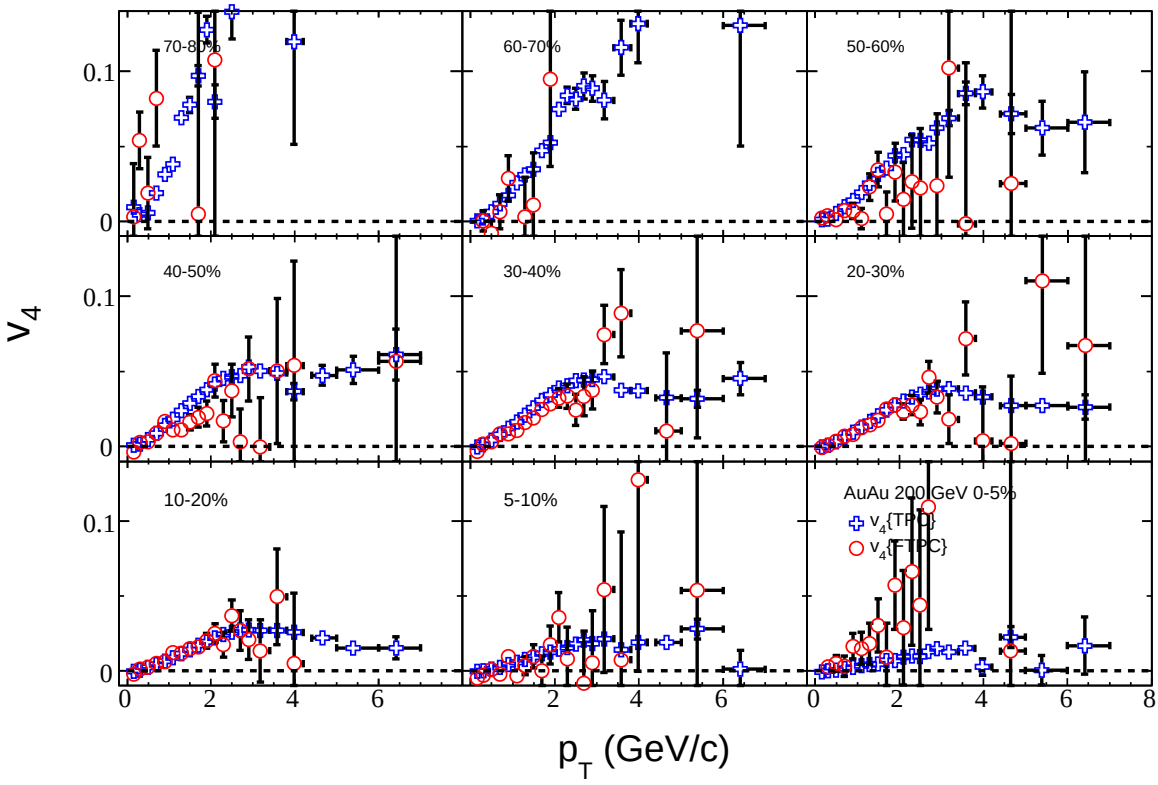

Figure 5.12: Charged particle v_4 as a function of transverse momentum (p_T) for centrality $70-80\%$, $60-70\%$, $50-60\%$, $40-50\%$, $30-40\%$, $20-30\%$, $10-20\%$, $5-10\%$ and $0-5\%$ in Au + Au collisions at $\sqrt{s_{NN}} = 200$ GeV from the TPC event plane method (crosses) and FTPC event plane method (circles).

the non-flow effect is larger in peripheral collisions than in central collisions although the errors are large.

5.2.2 Particle species dependence

v_4 of reconstructed particles K^0_S and Λ ($\bar{\Lambda}$) is shown in Figure 5.13 as a function of transverse momentum p_T for centrality $0\% - 80\%$ at mid-rapidity ($|\eta| < 1$) in Au + Au collisions at $\sqrt{s_{NN}} = 200$ GeV. At low p_T, the v_4 for K^0_S is larger than for Λ ($\bar{\Lambda}$). This mass ordering effect is similar as that of v_2. Both v_2 for K^0_S and v_2 for Λ increase with p_T until reach their peak values at intermediate p_T (~ 3 GeV/c). When p_T is larger than 3 GeV/c, the heavier baryon (Λ) is larger than that of the lighter mesons (K^0_S).

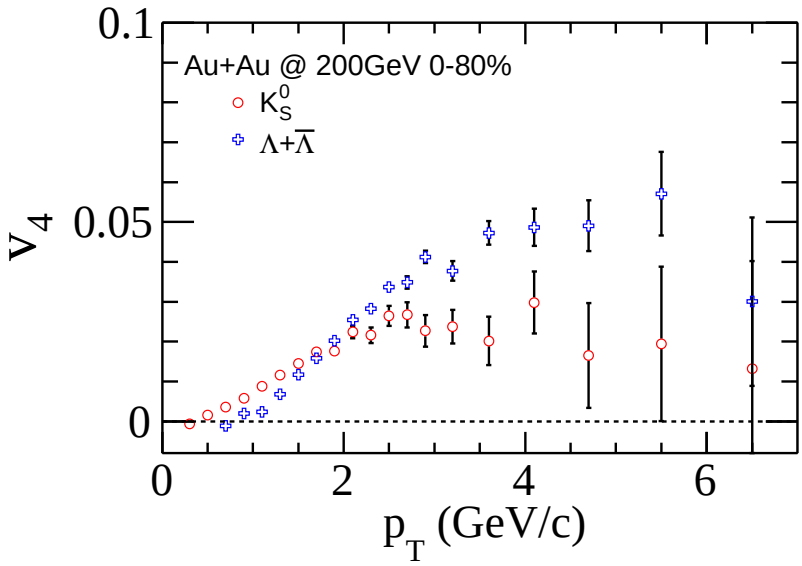

Figure 5.13: K^0_S and $\Lambda + \bar{\Lambda}$ v_4 as a function of transverse momentum (p_T) for centrality $0 - 80\%$ in Au + Au collisions at $\sqrt{s_{NN}} = 200$ GeV from the TPC event plane method.

The centrality dependence of v_4 for K^0_S and Λ ($\bar{\Lambda}$) is shown in Figure 5.14. Similar centrality dependence as charged particles is observed for both K^0_S and Λ ($\bar{\Lambda}$). The largest v_4 amplitude is observed in peripheral collisions while the smallest amplitude is observed in central collisions. The particle type dependence is similar as v_2 in all centralities. At low p_T, v_2 for K^0_S is larger than for Λ, while v_2 for K^0_S is smaller than for Λ at intermediate and large p_T.

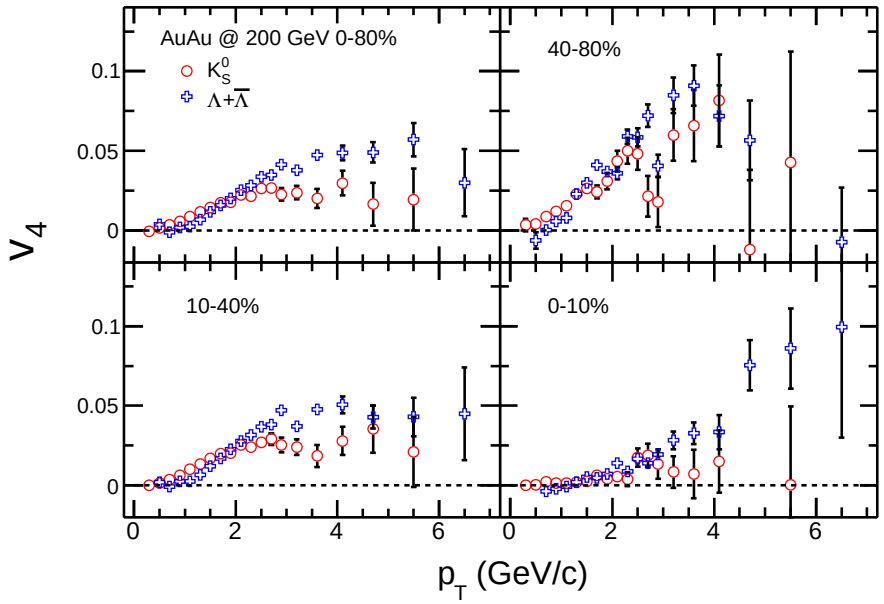

Figure 5.14: K^0_S (circles) and Λ (squares) v_4 as a function of transverse momentum (p_T) for centrality $0-80\%$, $40-80\%$, $10-40\%$ and $0-10\%$ in Au + Au collisions at $\sqrt{s_{NN}} = 200$ GeV from the TPC event plane method.

5.2.3 Number of constituent quark scaling of v_4

In hydrodynamic calculation [**?**], particle v_2 is related to fluid 4-velocity. The ϕ dependence of particle distribution results from a similar ϕ dependence of the fluid 4-velocity:

$$u(\phi) = U(1 + 2V_2 \cos 2\phi + 2V_4 \cos 4\phi + \cdots), \tag{5.2}$$

where ϕ is the azimuthal angle of the fluid velocity with respect to the participant plane. And the second (fourth) coefficient V_2 (V_4) can be related to particle v_2 and v_4 as

$$\begin{aligned} v_2(p_T) &= \frac{V_2 U}{T}(p_T - m_T v) \\ v_4(p_T) &= \frac{1}{2}v_2(p_T)^2 + \frac{V_4 U}{T}(p_T - m_T v), \end{aligned} \tag{5.3}$$

where $v = U/\sqrt{1+U^2}$. Thus v_4 is the the sum of two contributions: an "intrinsic" v_4 proportional to the $\cos 4\phi$ term in the fluid velocity distribution, V_4, and a contribution induced by elliptic flow itself, which turns out to be exactly $\frac{1}{2}(v_2)^2$. The latter contribution becomes dominant as p_T increases.

Therefore, it is interesting to check the NCQ scaling of higher harmonic v_4. Figure 5.15 shows the v_4/n_q^2 of K_S^0 and Λ as a function of p_T/n_q for centrality $0-80\%$ in Au + Au collisions at $\sqrt{s_{NN}} = 200$ GeV from the TPC event plane method. It is clear to see that after divided by n_q^2, v_4 for K_S^0 and Λ coincide with each other very well until 1.5 GeV/c. It confirms that v_4 behaves like v_2^2 when $p_T > 1$ GeV/c as in hydrodynamic calculation.

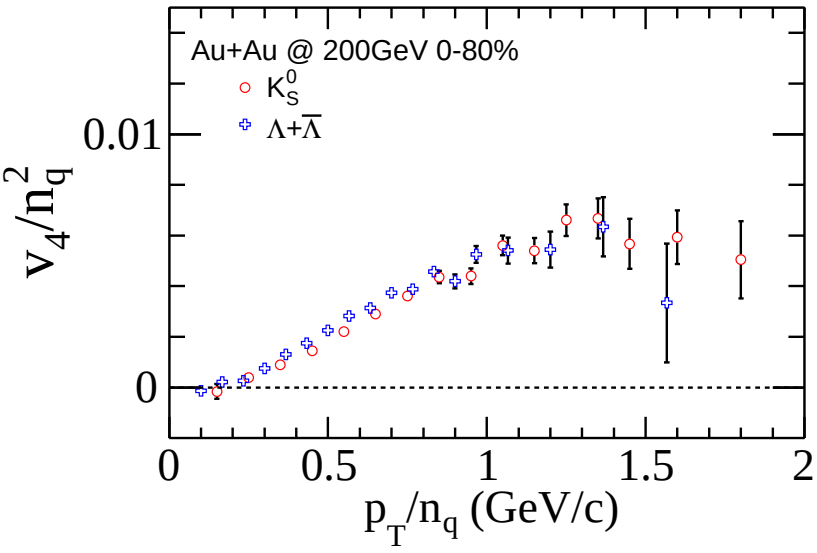

Figure 5.15: v_4/n_q^2 of K_S^0 and $\Lambda + \bar{\Lambda}$ as a function of p_T/n_q for centrality $0-80\%$ in Au + Au collisions at $\sqrt{s_{NN}} = 200$ GeV from the TPC event plane method.

5.3 Ideal hydrodynamic comparison

In ideal hydrodynamic calculation as shown in Eq. 5.3, the ratio v_4/v_2^2 is expected to reach 0.5 when p_T increases. Therefore, it is important to check whether the ratio v_4/v_2^2 of data to see whether our system behaves like ideal hydro.

Figure 5.16 shows charged particle v_4/v_2^2 as a function of transverse momentum (p_T) for centrality $70-80\%$, $60-70\%$, $50-60\%$, $40-50\%$, $30-40\%$, $20-30\%$, $10-20\%$, $5-10\%$ and $0-5\%$ in Au + Au collisions at $\sqrt{s_{NN}} = 200$ GeV. The ratio v_4/v_2^2 is very sensitive to the non-flow effect. As mentioned previously, the non-flow effect contributes

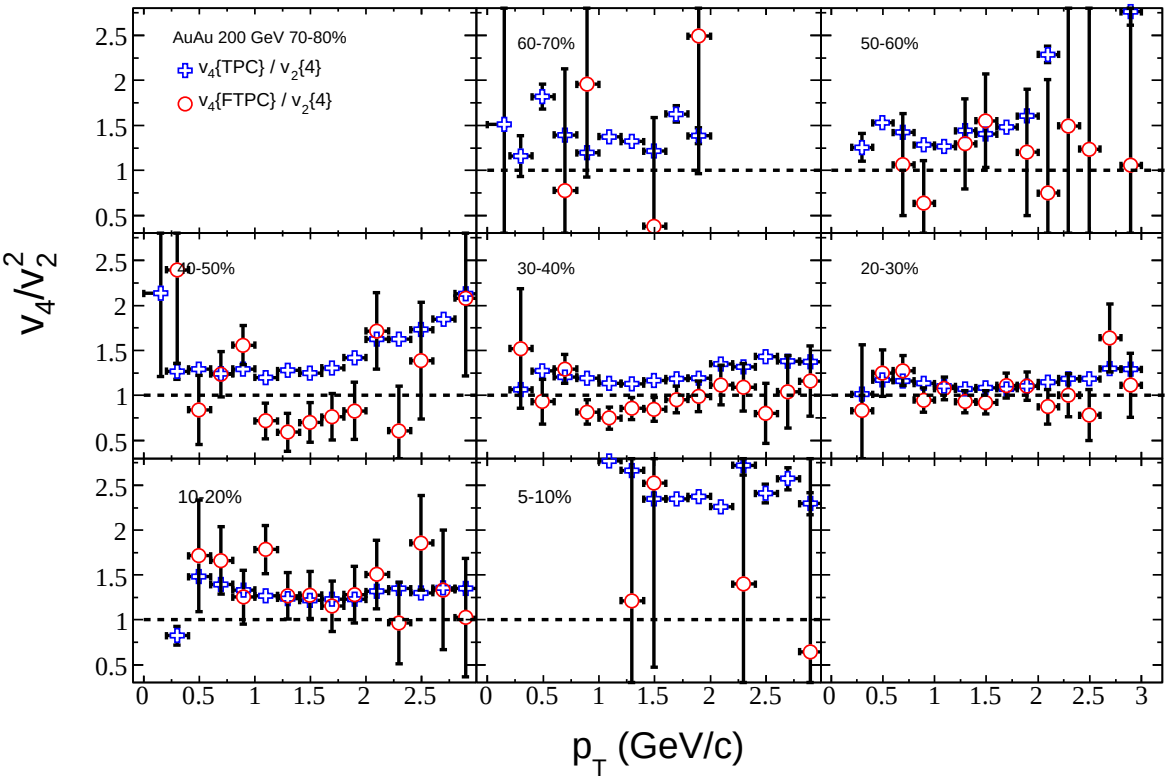

Figure 5.16: Charged particle v_4/v_2^2 as a function of p_T for centrality $70-80\%$, $60-70\%$, $50-60\%$, $40-50\%$, $30-40\%$, $20-30\%$, $10-20\%$, $5-10\%$ and $0-5\%$ in Au + Au collisions at $\sqrt{s_{NN}} = 200$ GeV. v_2 is from 4-particle cumulant method while v_4 is from TPC event plane (crosses) and FTPC event plane (circles).

to the estimation of bot v_2 and v_4. Since $v_2\{4\}$ is not sensitive to the non-flow effect, we use $v_2\{4\}$ as the denominator of v_4/v_2^2. Then the main non-flow effect contributing to the measurement v_4/v_2^2 is from v_4. It is clear that the non-flow effect would enhance the value of v_4 and also v_4/v_2^2. Here v_4 is measured from both TPC event plane (crosses) and FTPC event plane (circles). From the plot we can see that the ratio $v_4\{\text{TPC}\}/v_2^2$ is around 1 or larger for all the centralities. $v_4\{\text{FTPC}\}/v_2^2$ is a little smaller than $v_4\{\text{TPC}\}/v_2^2$, however, it is still larger than the ideal hydro predictions. One of the explanation is that interactions among the produced particles are not strong enough to produce local thermal equilibrium, so that the hydrodynamic description breaks down, the resulting value of v_4/v_2^2 is higher [**?**]. It is also argued that elliptic flow fluctuations may enhance the value of v_4/v_2^2 [**?**].

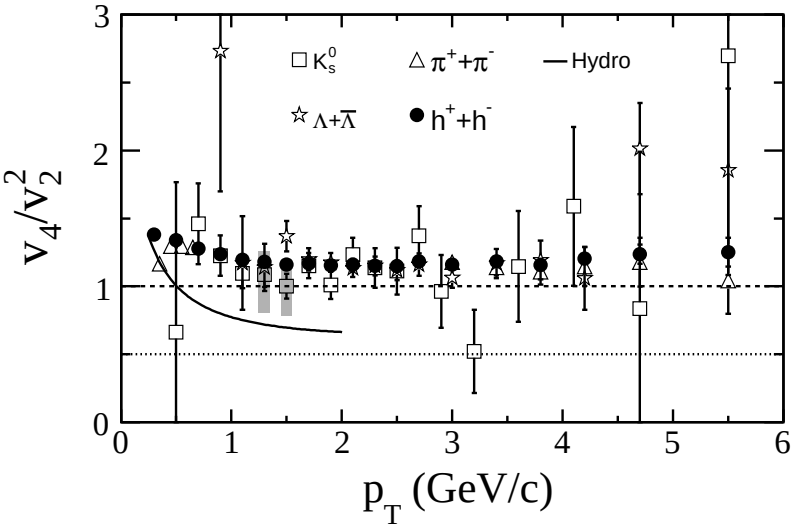

Figure 5.17: v_4/v_2^2 of $\pi^{\pm}$, p ($\bar{p}$), K_S^0 and $\Lambda(\bar{\Lambda})$ with TPC event plane as a function of transverse momentum for centrality $0-80\%$ in Au + Au collisions at $\sqrt{s_{NN}} = 200$ GeV. The solid curve is from hydro calculation [**?**].

The effects of v_2 fluctuations on the value of v_4/v_2^2 can be estimated as follow. The v_2 from two-particle correlations is denoted by $v_2\{2\}$ and defined by $v_2\{2\} \equiv \langle\cos(2\phi_1 - 2\phi_2)\rangle$. If v_2 fluctuates within the sample of events, $\langle\cos(2\phi_1 - 2\phi_2)\rangle = \langle(v_2)^2\rangle$. Similarly,

if v_4 and v_2 fluctuate, $\langle\cos(4\phi_1 - 2\phi_2 - 2\phi_3)\rangle = \langle v_4(v_2)^2\rangle$. We thus obtain

$$\frac{v_4\{3\}}{v_2\{2\}^2} = \frac{\langle v_4(v_2)^2\rangle}{\langle(v_2)^2\rangle^2} = \frac{1}{2}\frac{\langle(v_2)^4\rangle}{\langle(v_2)^2\rangle^2} \tag{5.4}$$

where, in the last equality, we have assumed that the prediction of hydrodynamics, $v_4 = (v_2)^2/2$ holds for a given value of v_2. If v_2 fluctuates, $\langle(v_2)^4\rangle > \langle(v_2)^2\rangle^2$, which shows that elliptic flow fluctuations increase the observed v_4/v_2^2.

Figure 5.17 shows v_4/v_2^2 of charged hadron, $\pi^{\pm}$, p ($\bar{p}$), K_S^0 and $\Lambda(\bar{\Lambda})$ as a function of transverse momentum for centrality $0-80\%$ in Au + Au collisions at $\sqrt{s_{NN}} = 200$ GeV. Both v_2 and v_4 are from TPC event plane. The ideal hydrodynamic calculation [**?**] is shown as the black curve. The shaded band is the systematic uncertainty of charged hadron, the non-flow effect is calculated by Eq. 5.4. The values of v_4/v_2^2 for charged hadron and identified particles are close to unity when p_T is larger than 1 GeV/c, no obvious particle type dependence is observed. It means that even take the flow fluctuations into account, the value of v_4/v_2^2 of our data is still larger than ideal hydrodynamic prediction.

5.4 Summary

We analyze 60,000,000 minimum bias events from Au + Au collisions at $\sqrt{s_{NN}} = 200$ GeV collected from STAR experiment during RHIC Run VII. The two largest anisotropic flow coefficients, elliptic flow v_2 and the forth harmonic v_4 are measured for charged particles as well as charged pions, (anti)protons, K_S^0 and Λ ($\bar{\Lambda}$). The flow coefficients are studied as function of transverse momentum, transverse energy and centrality. The main systematic uncertainty comes from so-called non-flow contributions and from the unknown fluctuations in the observables. Therefore, the TPC event plane method, FTPC event plane method and four-particle cumulant method are applied to study the anisotropic flow coefficients and estimate the systematic uncertainty based on the differences between the methods.

Elliptic flow v_2

Elliptic flow for charged particles is shown up to 15 GeV/c for different centralities using the TPC event plane method ($v_2\{\text{TPC}\}$), FTPC event plane method ($v_2\{\text{FTPC}\}$) and the four-particle cumulant method ($v_2\{4\}$) in this thesis. v_2 firstly increases with p_T, and then reaches its peak value at about 2 GeV/c. As p_T continues increasing, v_2 decreases significantly, and non-flow effect plays an important role in this region. $v_2\{4\}$ gives the low boundary of v_2. The sizable v_2 has been observed up to $p_T = 10$ GeV/c, which is consistent with the scenario of parton energy loss. And it is also the evidence for the formation of very dense matter.

Elliptic flow of identified particles (π, p ($\bar{p}$), K^0_S, Λ ($\bar{\Lambda}$)) are measured up to 6 GeV/c using both the TPC event plane and the FTPC event plane. At $p_T < 2$ GeV/c region, the mass ordering is observed as previous study. We find a deviation from exact Number of Constituent Quark Scaling (NCQ) of pions compared to baryons by approximately 20% from 0.5 up to $p_T/n_q \simeq 1.5$ GeV/c, while models with realistic effects included can only explain a deviation up to 5% from a meson-baryon difference. The deviation from NCQ scaling between kaons and baryons are less prominent and less than 10%. The Coalescence models require a significant fragmentation contribution to account for the large deviation from scaling at the upper end of the measured p_T/n_q and $(m_T?m)/n_q$ range. This suggests that fragmentation may kick in and becomes more dominant in this region.

The fourth harmonic v_4

Since v_4 signal is relative small, we use the 2^{nd} harmonic reconstructed event plane. v_4 for charged particles is shown up to 7 GeV/c for different centralities using the TPC event plane method and FTPC event plane method, and v_4 for K^0_S and Λ ($\bar{\Lambda}$) is shown up to 7 GeV/c using the TPC event plane method. v_4 first increases with p_T at low p_T range and then becomes saturate at intermediate p_T. v_4 for K^0_S is larger than for Λ ($\bar{\Lambda}$) at low p_T while smaller at intermediate p_T, this behavior is similar to the behavior observed for identified particle v_2.

The ratio v_4/v_2^2 is proposed as a probe of ideal hydrodynamic behavior, and it is directly related to the degree of thermalization. The measured ratio v_4/v_2^2 as a function of p_T is studied for both charged particle and identified particles. It is found that the ratio v_4/v_2^2 is about 1 when p_T is about 2 GeV/c for all the particles, which is larger than the ideal hydrodynamic prediction. This may be due to the fluctuation of the measured v_2 and v_4, but also may indicate the incomplete thermalization of the system.

CHAPTER 6

Results II: Longitudinal property of Charge Balance Function

In this chapter, we present the results of charge balance function in π^+p and K^+p collisions from NA22 experiments and Au+Au collisions from STAR experiments. The dependences on (pseudo)rapidity windows, transverse momentum, colliding energy and system size are studied. The longitudinal property and the width of charge balance function are also investigated in Monte Carlo models.

6.1 Boost invariance of charge balance function

Conventionally, boost invariance, as originally assumed [**?**], refers to single particle density being independent of rapidity. It has been applied in hydrodynamic model [**?**, **?**] to simplify the equation of state. In heavy ion collisions, there is a plateau of the single particle density distribution in mid-rapidity which can satisfy the requirement of the assumption. However, the boost invariance of the balance function only requires that the charge correlation between final state particles be the same in any longitudinally-Lorentz-transformed frame. Therefore, it is interesting to check the longitudinal property of BF in whole phase space.

6.1.1 Hadron-hardon collisions

The boost invariance of the charge balance function is firstly studied on π^+p and K^+p data at 250 GeV/c ($\sqrt{s_{NN}}$ =22 GeV) of the NA22 experiment. This experiment was

equipped with a rapid cycling bubble chamber as an active vertex detector, had $\Delta p/p = 1.5\%$ momentum resolution and 4π acceptance. The latter feature allows, for the first time, to study the properties of the balance function in full phase space.

Since no statistically significant differences are seen between the results for π^+ and K^+ induced reactions, the two data samples are combined for the purpose of this analysis. A total of 44,524 non-single-diffractive events is obtained after all necessary selections (all tracks well reconstructed, exclusion of elastic and single-diffractive events), as described in detail in [**?**, **?**]. In particular, possible contamination from secondary interactions is suppressed by a double visual scan with 99.5% efficiency and the requirement that overall charge balance be satisfied within the whole event; γ conversions near the primary vertex are removed by electron identification.

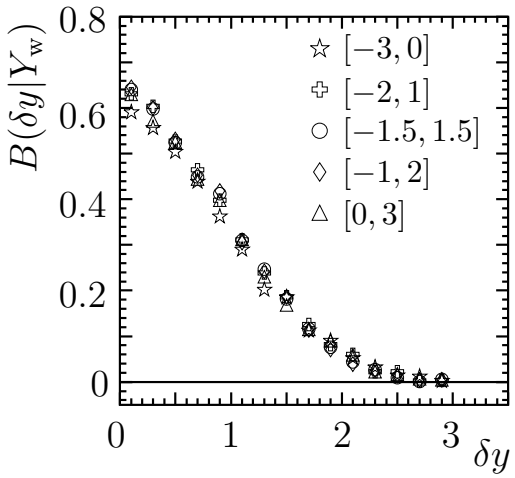

Figure 6.1: The balance function for five different positions of a rapidity window of size $Y_w = 3$.

In Figure 6.1, the balance function is shown for five rapidity windows of width $Y_w = 3$, located at different positions, $[-3, 0]$, $[-2, 1]$, $[-1.5, 1.5]$, $[-1, 2]$, and $[0, 3]$. In this and the following figures, the errors are statistical only and some of them are smaller than the size of the symbols. The five functions coincide within the experimental errors, except that a few points in $[-3, 0]$ are somewhat lower than the others. This is caused by very low multiplicities in the rapidity region $[-3, -2]$, where unidentified protons contribute and where the rapidity distribution is not completely symmetric to the rapidity region $[+2, +3]$. The figure demonstrates that, despite a strong rapidity dependence of the

particle density given in Figure 6.2, the balance function is largely independent of the position of the rapidity window, i.e., the charge correlation is essentially the same in any longitudinally-Lorentz-transformed frame.

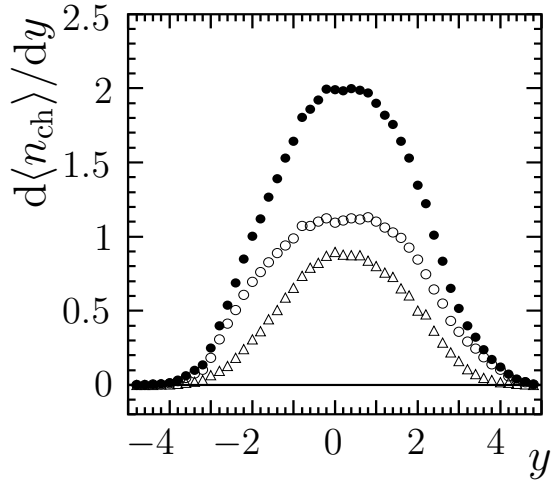

Figure 6.2: The rapidity distributions of positively (open circles), negatively (open triangles), and all (solid circles) charged particles.

Since boost invariance of the BF is found to be valid over the whole rapidity region, it is now interesting to verify if the BF in a limited rapidity window can be deduced from that in the full rapidity region by Eq. 2.11, and vice versa. In Figure 6.3, the balance function, $B(\delta y|Y_{\mathrm{w}})$ (solid points), for four rapidity windows (central in Fig. 6.3a, non-central in Fig. 6.3b), is compared to $B(\delta y|\infty)(1-\frac{\delta y}{Y_{\mathrm{w}}})$ (open points) obtained for the corresponding window from the BF in the full region. The data confirm that the relation Eq. 2.11 is indeed approximately satisfied, independently of size or position of the window. This result is especially important for experiments with limited acceptance, in particular for the current heavy ion experiments. It further illustrates that the BF becomes narrower with decreasing Y_{w}, in agreement with Eq. 2.11.

6.1.2 Nuclear-nuclear collisions

Since the boost invariance property of balance function has been observed in hadron-hadron collisions, it is also interested to see whether such property is holding in heavy ion collisions. Here we analyze about 25 M mini-bias events in Au + Au collisions from

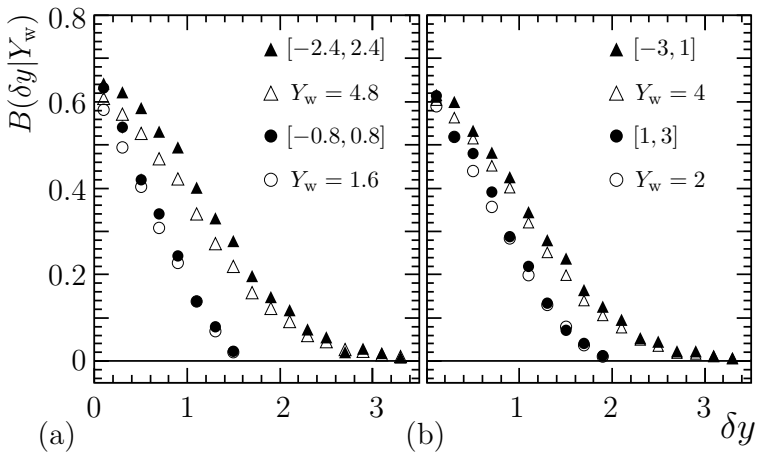

Figure 6.3: The balance functions $B(\delta y|Y_w)$ (solid symbols) (a) for two central rapidity windows, $[-2.4, 2.4]$ and $[-0.8, 0.8]$ and (b) two asymmetric rapidity windows $[-3, 1]$, and $[1, 3]$, compared with the corresponding $B(\delta y|\infty) \cdot (1 - \frac{\delta y}{Y_w})$ (open symbols).

STAR during RHIC Run IV.

Figure 6.4(a) displays BF distributions obtained with five different pseudorapidity windows, located at various positions, and with sizes ranging from $|\eta_w| = 0.6$ to 2.6. Vertical bars shown in this and following figures correspond to statistical errors only. Statistical errors are smaller than the symbol sizes in Fig. 6.4. Systematic errors are of the order of 5% and due to uncertainties in the track reconstruction efficiency associated with the track cuts, and event-by-event variations of the vertex position. The BF is strongly dependent on the width of the pseudorapidity window.

In order to test directly whether the BF is boost-invariant under longitudinal translation within the STAR TPC, five BFs are measured in equal size ($|\eta_w| = 0.8$) pseudorapidity windows located at different positions as shown in Fig. 6.4(b). It is observed that the five BFs overlap with one another thereby indicating that the BF is independent of the position of the pseudorapidity window, i.e., $B(\delta\eta|\eta_w)$ is invariant under a longitudinal translation within the range $-1 < \eta < 1$. Note that the large BF values measured at $\delta\eta = 0.1$ arise in part from HBT and Coulomb effects [**?**, **?**].

In Fig. 6.4(c), the scaled balance functions, B_s, are calculated with Eq. 2.11, obtained from BFs measured with four distinct pseudorapidity window widths ($|\eta_w|$ =0.6, 1, 2, 2.6) and six window positions. It is found that the scaled balance functions have equal

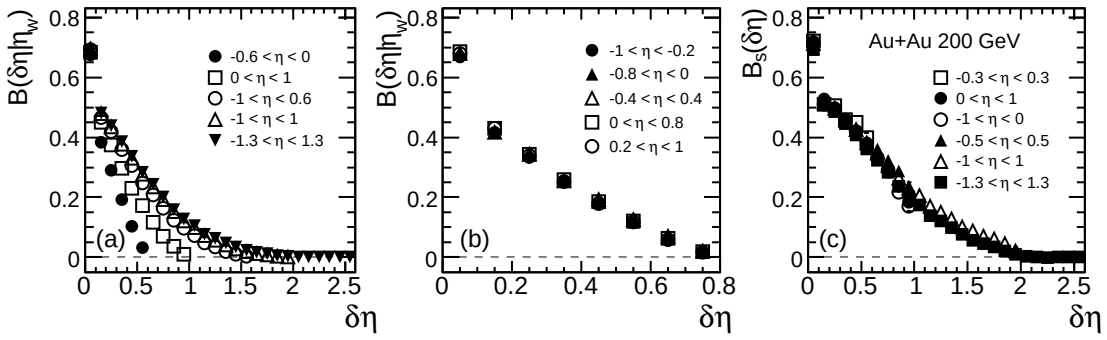

Figure 6.4: (a) Balance functions in five pseudorapidity windows of different width; (b) Balance functions observed at five different positions of pseudorapidity windows with $|\eta_{\rm w}| = 0.8$; (c) Scaled balance function, $B_s(\delta\eta)$, obtained for various pseudorapidity window widths and positions. Where $0 - 80\%$ centrality are selected and particle p_T range is $0.15 < p_T < 2$ GeV/c for Au+Au collisions at 200GeV. Statistical errors are smaller than the symbol sizes. Systematic errors are of the order of 5%.

shape and magnitude, and are identical within experimental errors. Therefore B_s is independent of the size and position of the window $\eta_{\rm w}$ in the pseudorapidity range $-1 < \eta < 1$. A similar invariance of B_s was observed in hadron-hadron interactions over the whole rapidity range of produced particles [**?**].

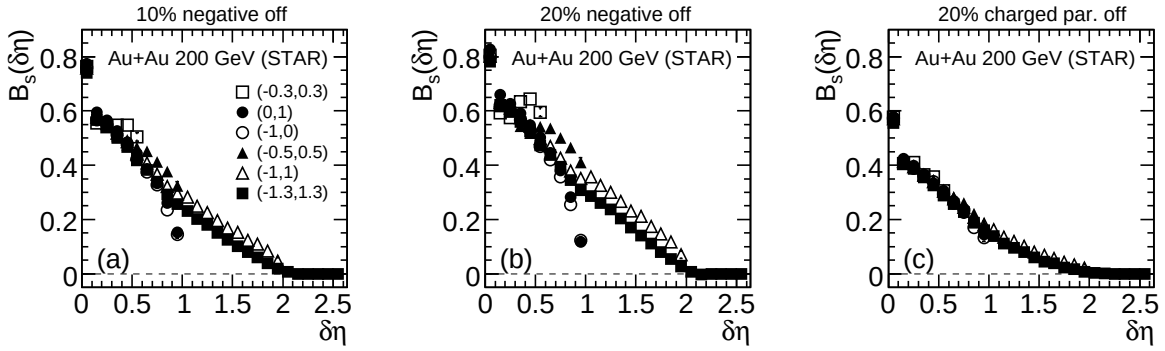

Figure 6.5: $B_s(\delta\eta)$ for three subsamples, in which (a) 10% negative, (b) 20% negative and (c) 20% charged particles are randomly thrown away, respectively..

This longitudinal property of BF comes from the special longitudinal interaction of charged particles under the constraint of global electric charge balance. In order to see that the global charge balance is a necessary condition for the observed longitudinal property of BF, we construct two subsamples by randomly throwing 10% and 20% neg-

ative particles respectively away from each of the minimum bias events. It is clear that global net charge is out of balance in each event of these two samples, and longitudinal charge correlation in the whole phase space is uniformly changed. The scaled BF for these two samples are shown in Figure 6.5(a) and (b), respectively. We can see from the figure that the farther the charge is out of balance, the more seriously the longitudinal property of BF is violated. Therefore, the longitudinal property of balance function is sensitive to the global charge balance.

In addition, if charged particles are randomly thrown off from each events, e.g., 20% charged particles off as shown in Fig 6.5(c), the longitudinal property of BF keeps well. This is what to be expected, as the global electric charge balance maintains more or less in each event in the case. It is the same as what we deal with data reconstruction. So, the observed longitudinal property of BF also shows that the global charge conservation are well taken into account in the data reconstruction in STAR TPC.

6.1.3 Transverse momentum dependence

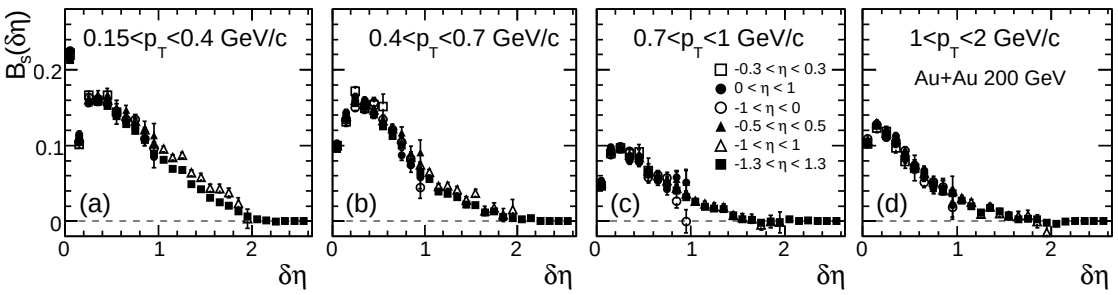

Figure 6.6: $B_s(\delta\eta)$ based on $B(\delta\eta|\eta_{\rm w})$ values measured in different pseudorapidity windows for particles in four p_T bins. Where $0-80\%$ centrality are selected and particle p_T range is $0.15 < p_T < 2$ GeV/c for Au+Au collisions at 200GeV. Error bars are statistical only. Systematic errors are of the order of 5%.

It is also investigated whether the scaling property of the BF holds for particles in different p_T ranges. Fig. 6.6 displays B_s distributions obtained for four p_T ranges: (0.15, 0.4), (0.4, 0.7), (0.7, 1) and (1, 2) GeV/c and the same pseudorapidity windows used in Fig. 6.4(c). It is clear that the scaled BFs in the same p_T bin but different positions

of pseudorapidity window are consistent with each other very well. It means that such longitudinal boost invariance doesn't have p_T dependence . Comparing the distributions shown in Fig. 6.6(a) to Fig. 6.6(d), it is clear that the scaled balance function, $B_s(\delta\eta)$, changes significantly in shape and amplitude with the p_T of final state particles.

6.1.4 Centrality dependence

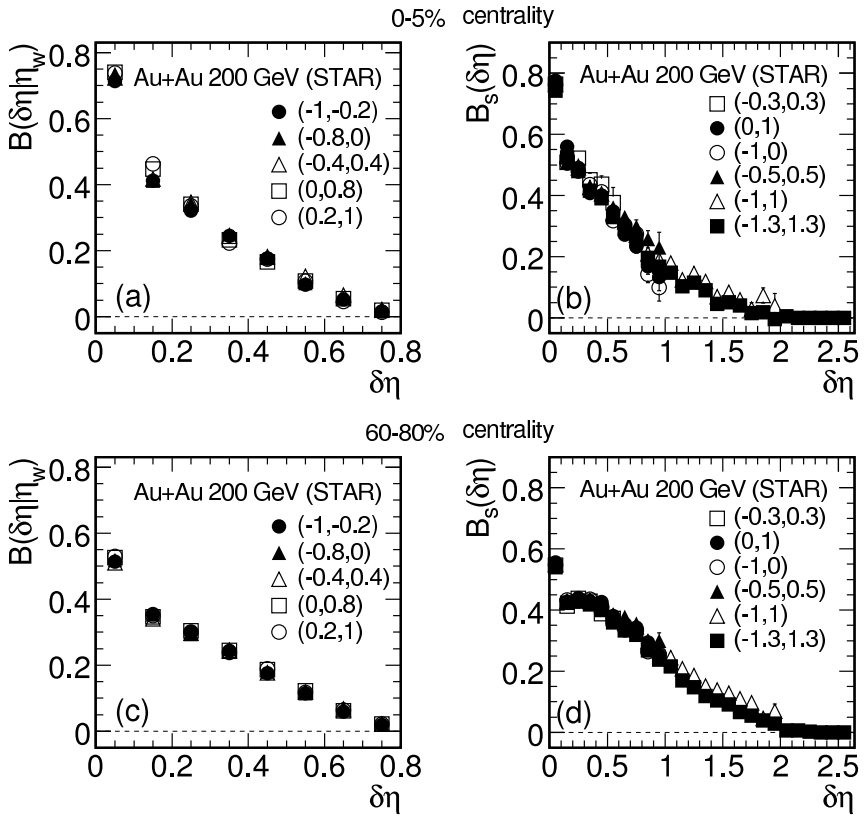

Figure 6.7: $B(\delta\eta|\eta_{\rm w})$ and scaled balance function, $B_s(\delta\eta)$, in central collisions $(0-5\%)$ and peripheral collisions $(60-80\%)$, respectively.

The centrality dependence of Balance Function is show in Figure 6.7. BFs with same width but different positions in (a) central collisons $(0-5\%)$ and (c) peripheral collisions are shown. We can see that BFs still overlap with each other in the same centrality, although their shapes and widths are different in different centralities. BFs in five pseudorapidity windows of different width in central collision $0-5\%$ is shown in Fig. 6.7(a). The scaled balance function, $B_s(\delta\eta)$, obtained from six pseudorapidity

windows is shown in Fig. 6.7 for (b) central and (d) peripheral collisions. As shown in minbias data in Fig. 6.4(c), the scaled balance functions are almost identical in the same centrality. It indicates that there is little centrality dependence for the charge compensate mechanism described by Balance Function.

6.1.5 Model investigation

The results from both hadron-hadron and nuclear-nuclear collisions indicate that charge balance of produced particles in strong interactions is boost-invariance in longitudinal phase-space, in contrary with the single particle density. Therefore, it is interesting to check whether those properties are taken into account in the models which are successfully described hadron-hadron and nuclear-nuclear collisions. And more important, how they associate with the mechanisms of particle production in the models.

In order to demonstrate directly whether the BF is invariant under a longitudinal Lorentz transformation over the whole rapidity in hadron-hadron collisions, we choose four equal size ($|\eta_{\rm w}| = 3$) pseudorapidity windows locating at different positions $(-3, 0)$, $(-2, 1)$, $(-1, 2)$ and $(0, 3)$. The results for $p+p$ collisions at $\sqrt{s} = 22$ GeV and $\sqrt{s} = 200$ GeV are shown in Figure 6.8 (a) and (b) respectively. The statistic errors are smaller than the markers. It is clear that the BF measured in four windows are approximately identical to each other at two incident energies. This indicates that the charge compensation is essentially the same in any longitudinally-Lorentz-transformed frame for $p + p$ collisions in the PYTHIA model, consistent with the data from NA22 experiment. These results show that the string fragmentation mechanism implemented in PYTHIA well describes the production mechanisms of charge particles and their charge balance in longitudinal phase space.

Fig. 6.8 (c) and (d) are the scaled balance function $B_s(\delta\eta)$ at two incident energies. They are deduced from directly measured $B(\delta\eta|\eta_{\rm w})$ at six different pseudorapidity windows, $(-0.8, 0.8)$ (open circles), $(1, 3)$ (open triangles), $(-3, 1)$ (open squares), $(-2.4, 2.4)$ (open diamonds), $(0, 3)$ (open crosses), and $(-2, -1)$ (open stars). From the figures we can see that all the $B_s(\delta\eta)$ deduced from different windows are coincide with each other

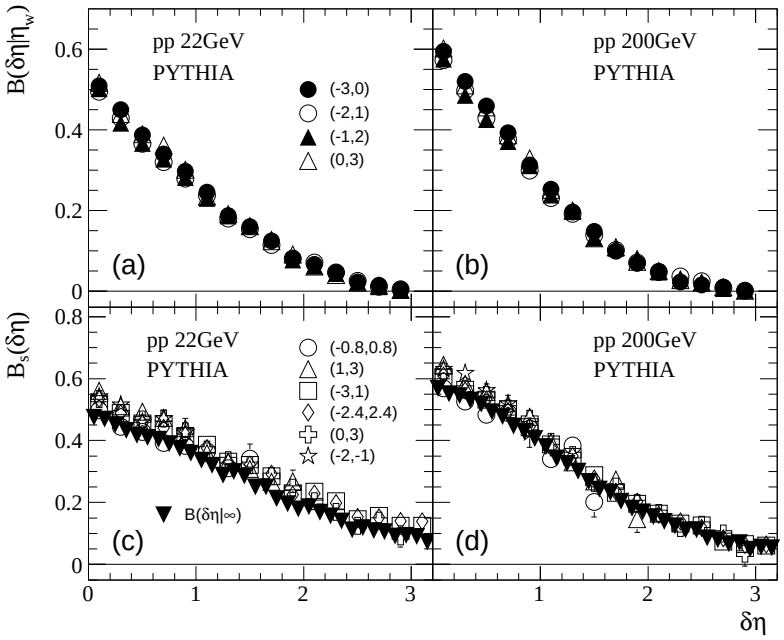

Figure 6.8: Upper panel: the $B(\delta\eta|\eta_{\rm w})$ in four pseudorapidity windows with equal size $|\eta_{\rm w}| = 3$ at the different positions for $p+p$ collisions at (a) $\sqrt{s} = 22$ GeV and (b) $\sqrt{s} = 200$ GeV by PYTHIA model. Lower panel: the scaled balance function, $B_s(\delta\eta)$, deduced from the directly measured BF at six different sizes and positions of pseudorapidity windows for $p+p$ collisions at (c) $\sqrt{s} = 22$ GeV and (d) $\sqrt{s} = 200$ GeV by PYTHIA model. The solid down triangle is the BF of the whole η range.

within errors, as expected from boost-invariance of the BF [**?**]. The solid down triangles in the same figures are the BF of the whole pseudorapidity range, $B(\delta\eta|\eta_\infty)$. It is close to the scaled balance function $B_s(\delta\eta)$. These results indicate that the scaled BF is in fact corresponding to the BF of the whole pseudorapidity range $B(\delta\eta|\infty)$ [**?**].

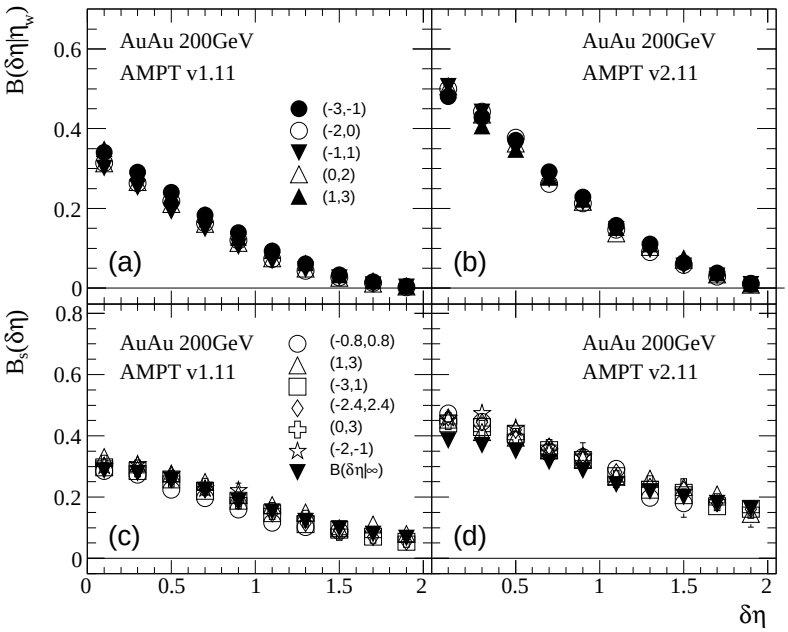

Figure 6.9: Upper panel: the $B(\delta\eta|\eta_{\rm w})$ in five pseudorapidity windows with equal size $|\eta_{\rm w}| = 2$ at the different positions for Au+Au collisions at $\sqrt{s} = 200$ GeV by (a) the AMPT default and (b) the AMPT with string melting. Lower panel: the scaled balance function, $B_s(\delta\eta)$, deduced from the directly measured BF at various pseudorapidity windows with different sizes and positions for Au+Au collisions at $\sqrt{s} = 200$ GeV by (c) the AMPT default and (d) the AMPT with sting melting.

It is then interesting to see whether the boost-invariance of the BF is held in nucleus-nucleus collisions. STAR experiment only observe the boost-invariance of BF in central pseudorapidity range $-1 < \eta < 1$ [**?**], where the single particle distribution is almost flat, or boost-invariance. Now in model investigation, we can carefully examine the property in the whole pseudorapidity range.

The upper panel of Figure 6.9 is the BF in five pseudorapidity windows with equal size $\eta_{\rm w} = 2$ at different positions $(-3,-1)$, $(-2,0)$, $(-1,1)$, $(0,2)$ and $(1,3)$. Where the Fig. 6.9 (a) and (b) are the results from the AMPT default (v1.11) and the AMPT with

string melting (v2.11), respectively. Both figures show that the BF is boost-invariance in pseudorapidity range (-3, 3) in two versions of the AMPT.

The lower panel of Fig. 6.9 is the scaled balance functions, which are obtained from directly measured BF at six different windows as indicated at legend of the figure, where the solid down triangles are the BF in pseudorapidity range (-4, 4). It shows that the scaled BF does not depend on the size and position of the windows, and corresponds to the BF of the whole pseudorapidity in two versions of the AMPT, consistent with the results of $p+p$ collisions in the PYTHIA model.

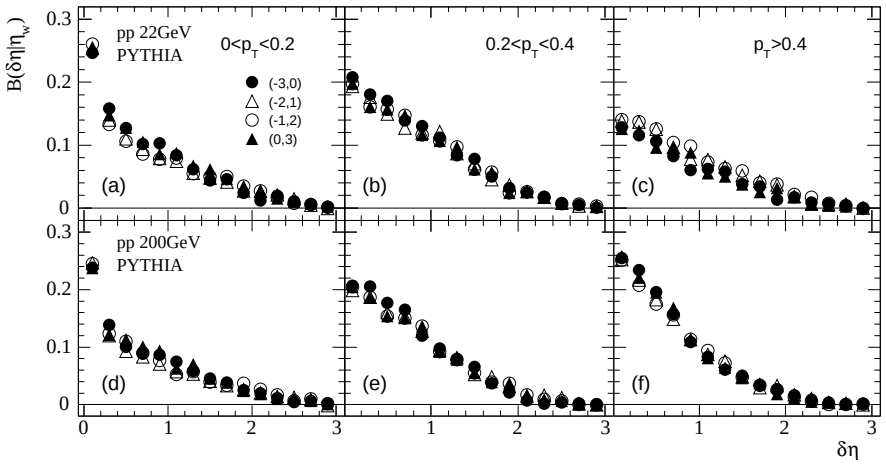

Figure 6.10: For each of three p_T ranges, the $B(\delta\eta|\eta_{\rm w})$ in four pseudorapidity windows with equal size $|\eta_{\rm w}| = 3$ at the different positions for $p+p$ collisions at $\sqrt{s} = 22$ GeV and $\sqrt{s} = 200$ GeV in upper and lower panels, respectively.

The longitudinal property of boost invariance of BF comes from the special longitudinal interaction of charged particles under the constraint of global electric charge balance. Global electric charge conservation not only applies to all final-state charged particles, but also constrains particles which are produced at the same proper time of evolution. It is argued that the transverse-momentum of final-state particles may be roughly used as a scale of the proper time of their production in the expansion of nuclear collisions [**?**, **?**, **?**, **?**]. Examining the p_T dependence of longitudinal property of the BF will provide direct access on whether particles in specified p_T range are consistent to be produced simultaneously with well balanced electric charge.

So we turn to check whether the boost-invariant of BF holds for particles in different

p_T ranges. Figure 6.10 shows the BF for $p+p$ collisions at $\sqrt{s} = 22$ GeV and $\sqrt{s} = 200$ GeV from PYTHIA in three transverse momentum bins $(0 < p_T < 0.2)$, $(0.2 < p_T < 0.4)$, and $(p_T > 0.2)$ GeV/c, respectively. These p_T bins are selected to make the multiplicity in each bin comparable. The result shows that the points at a given $\delta\eta$ in a restricted p_T interval are approximately coincide with each other, i.e., the boost-invariance of the BF hold in small p_T ranges. It indicates that particles produced at different p_T ranges are also boost-invariant for hadron-hadron collisions in the PYTHIA model.

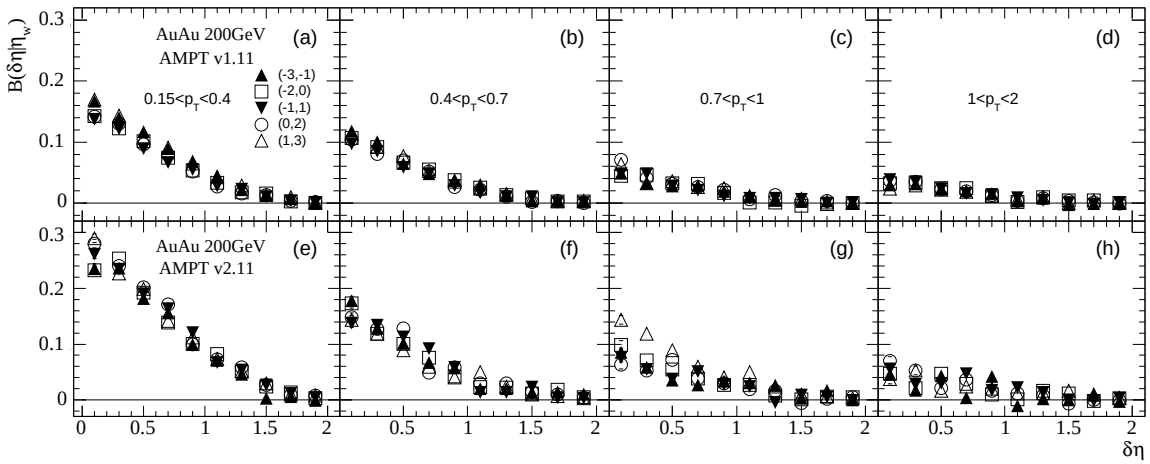

Figure 6.11: For each of four p_T ranges, the $B(\delta\eta|\eta_{\rm w})$ in five pseudorapidity windows with equal size $|\eta_{\rm w}| = 2$ at the different positions for Au+Au collisions at $\sqrt{s} = 200$ GeV from the AMPT default (in upper panel) and the AMPT with string melting (in lower panel).

The same study for Au+Au 200 GeV collisions from the two versions of the AMPT are presented in the upper and lower panels of Figure 6.11, respectively. Where four p_T bins are, $(0.15, 0.4)$, $(0.4, 0.7)$, $(0.7, 1)$ and $(1, 2)$ GeV/c. From the upper panel of the figure, we can see that the BF of different pseudorapidity windows in each p_T bin are close to each other, in consistent with the data from STAR experiment [**?**]. However, in the AMPT with string melting, as shown in the lower panel of the figure, where the BF of different pseudorapidity windows are not as close to each other as those in the upper panel.

This is because in the AMPT with string melting, each parton in the evolution of nuclear collision has its own freeze-out time, which last a very long period after the interaction of two nucleus [**?**]. The particles in the same transverse-momentum range are

not freezed-out simultaneously with well balanced charge, and therefore the longitudinal boost-invariance of the BF in small p_T ranges is violated. In the AMPT default, the partons recombined with their parent strings immediately after they stop interacting, and converted to hadrons. So the charge balance of the produced particles in the same p_T ranges is preserved and boost-invariance of the BF keeps.

6.2 The width of charge of balance function

The width of charge balance function is considered at a probe of QGP for clocking hadronization [**?**], however, the BF itself has multiplicity dependence. Thus, it is important to study the multiplicity dependence of BF to understand experimental result.

6.2.1 Multiplicity dependence

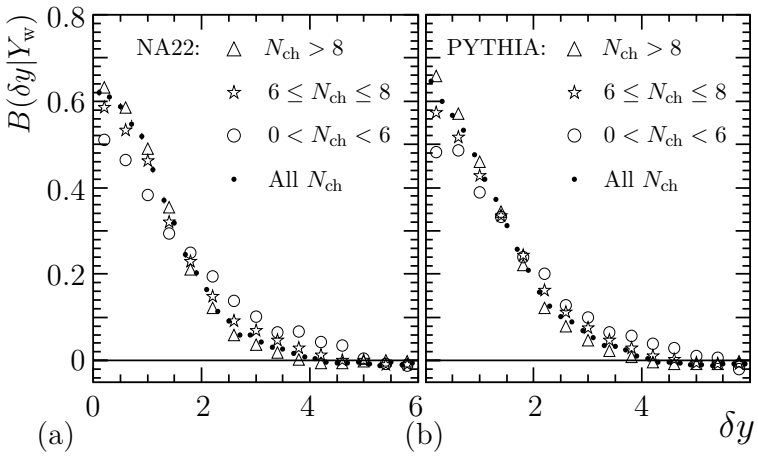

Figure 6.12: The balance function for all charged particles and for three multiplicity intervals from NA22 and PYTHIA.

In Figure 6.12(a), the full-rapidity BF, is presented for all charged particles as well as for three multiplicity intervals in π^+p and K^+p data at $\sqrt{s_{NN}}$ =22 GeV from the NA22 experiment. The width of the BF, for the corresponding multiplicity intervals and for all charged particles is listed in Table I. The width decreases with increasing multiplicity, which is, at least qualitatively, consistent with the narrowing of the BF with increasing centrality observed in current heavy ion experiments [**?**, **?**]. The corresponding results

Table 6.1: The width of the BF in three multiplicity intervals and for all charged particles.

Multiplicity	$\langle \delta y \rangle_{\mathrm{NA22}}$	$\langle \delta y \rangle_{\mathrm{PYTHIA}}$
$n_{ch} > 8$	0.957 ± 0.011	0.755± 0.010
$6 \leq n_{ch} \leq 8$	1.096 ± 0.014	0.929±0.011
$0 < n_{ch} < 6$	1.359 ± 0.026	1.159±0.023
all n_{ch}	0.991 ± 0.008	0.816±0.007

from PYTHIA 5.720 [**?**] are given in Figure 6.12(b) and Table 6.1. The hadronization scheme with string fragmentation implemented in PYTHIA qualitatively reproduces the trend of the data. Therefore, before a narrowing of the BF with increasing centrality and increasing mass number of the colliding nuclei can be interpreted as due to delayed hadronization connected to the possible formation of a QGP, the multiplicity effect observed here, which has nothing to do with the formation of a new state of matter, should be properly taken into account. This will relax the apparent contradiction between the narrowing of BF and the charge-fluctuation measurement in current heavy ion experiments.

6.2.2 Energy Dependence

From the previous experimental study, we know that the BF also becomes narrower as the increasing of multiplicity in hadron-hadron collisions at $\sqrt{s_{NN}} = 22$ GeV [**?**]. It is also interesting to see the how significant the multiplicity dependence is. Here, we study the width of BF in $p + p$ collisions from PYTHIA Monte-Carlo generator at four energy at $\sqrt{s_{NN}} = 22$, 64, 130 and 200 GeV with full rapidity space.

It can be seen from the Fig. 6.13 that for $p + p$ collision in this model, where no quark-parton phase is expected, the width of BF decreases with the increase of multiplicity, i.e., the width of BF is narrower for higher multiplicity. It is expected that the hadronization in hadron-hadron collisions is almost instantaneous, thus this effect has nothing to do with hadronization time. Also, the width of BF depends on collision energy. For the

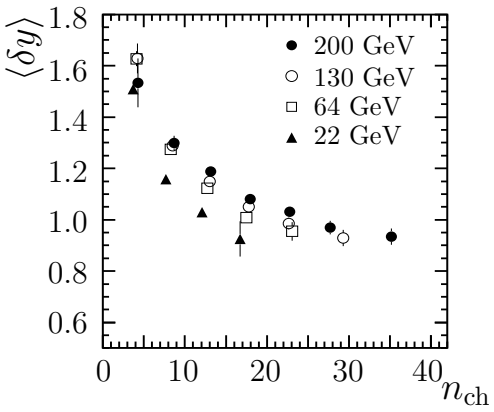

Figure 6.13: The width of full-phase-space balance function for different multiplicity in $p + p$ collisions at $\sqrt{s_{NN}} = 22$, 64, 130 and 200 GeV.

same multiplicity, the higher the collision energy is, the wider the width of balance function.

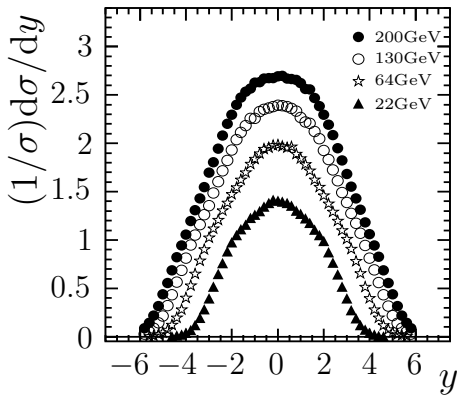

Figure 6.14: The rapidity distribution of all charged particles in $p + p$ collision at $\sqrt{s_{NN}} =$ 22, 64, 130, 200 GeV.

However, it also should be noticed that the BF is sensitive to the size of observed window [**?**], and the full rapidity region is wider for higher energy, as shown in Fig. 6.14. To remove the influence of the width of rapidity region, we choose a fixed-size observation window $-3 \leq y \leq 3$ to calculate the width of BF for all four energies. The results, presented in Fig. 6.15, show that when the (average) rapidity density dN/dy is the same, the width of balance function is almost independent of energy, especially for high dN/dy. From the plot we can conclude that in hadron-hadron collisions, the width of BF becomes narrower as multiplicity increases when the multiplicity is small (about

Table 6.2: The widths $\langle\delta\eta\rangle$ of the $B_s(\delta\eta)$ for four p_T bins. The first and second errors are statistic and systematic, respectively.

p_T(GeV/c)	$\langle\delta\eta\rangle$
(0.15, 0.4)	$0.652 \pm 0.006^{+0.081}_{-0.029}$
(0.4, 0.7)	$0.609 \pm 0.008^{+0.049}_{-0.037}$
(0.7, 1)	$0.536 \pm 0.016^{+0.047}_{-0.041}$
(1, 2)	$0.487 \pm 0.014^{+0.079}_{-0.021}$

≤ 20). And as the multiplicity continue increases, the width of BF gradually reaches its low limit. Also, the width of BF is independent of energy which is consistent with instantaneous hadronization in hadron-hadron collisions.

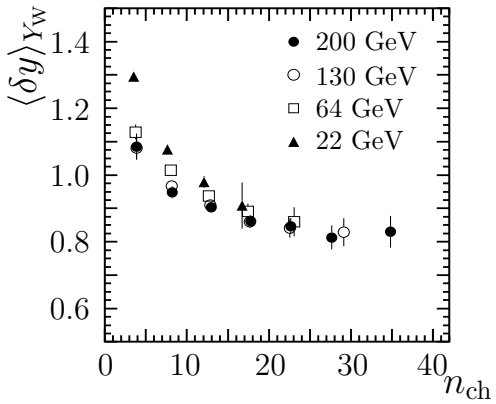

Figure 6.15: The width of balance function in the rapidity region $[-3, 3]$ for different multiplicity in $p + p$ collision at $\sqrt{s_{NN}}$ = 22, 64, 130 and 200 GeV.

6.2.3 Transverse momentum and centrality dependences

Balancing particle are separated in momentum space according to the thermal properties of the freezed-out stage of the system. As we know that the thermal velocities are determined by local temperature and particle mass, and they are related to transverse mass and transverse momentum for relativistic particles. Therefore, the BF is affected by transverse expansion (collective flow).

The widths of scaled $B_s(\delta\eta)$ are presented in Table 6.2 for Au + Au collisions at 200

GeV. The first data point in Fig. 6.6(a) is affected by HBT correlations, which result in a strong correlation at small relative p_T. On the other hand, track merging effects would deplete the balance function at small $\delta\eta$. To assess the systematic uncertainties on the extracted width, we use extrapolated values for the two lowest $\delta\eta$ data points instead of their measured ones in calculating the width. For the lower bound of systematic uncertainty estimate, the extrapolations from the larger $\delta\eta$ data are done by two functional forms. One is exponential for the p_T in (0.15, 0.4) and Gaussian for the other three p_T bins. For the upper bound of systematic uncertainty estimate, the extrapolated function is multinomial for all four p_T bins. Table 6.2 demonstrates that the width of the scaled BF becomes narrower for increasing p_T. This observation is qualitatively consistent with expectations from thermal models [**?**].

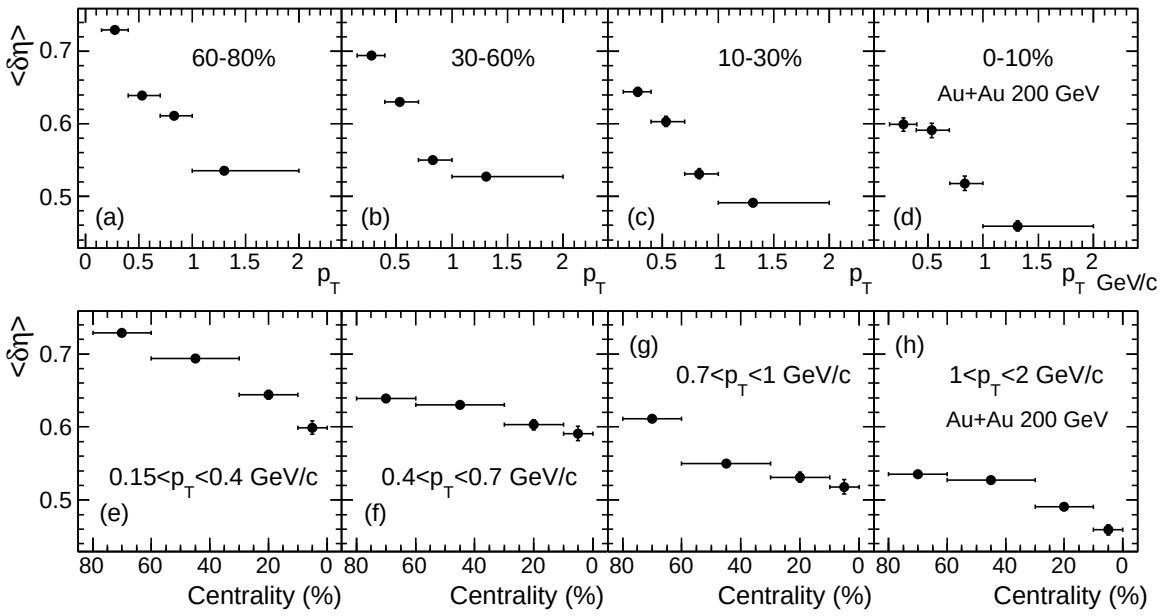

Figure 6.16: Upper panel: the p_T dependence of the width of the BF in different centrality bins; Lower panel: the centrality dependence of the width of the BF in different p_T intervals, for Au + Au collisions at 200 GeV.

As has been shown in [**?**], the width of the BF decreases with collision centrality. The decreases in the BF width with increasing p_T and increasing centrality could be associated with transverse radial flow [**?**, **?**, **?**]. In order to disentangle these effects, we further study the p_T dependence of $\langle\delta\eta\rangle$ in different centrality bins. This is shown in the upper panel of Fig. 6.16. It shows clearly that the width of the BF decreases

with the transverse momentum of final state particles in each centrality bin. We also study the centrality dependence of $\langle \delta\eta \rangle$ in different p_T intervals. This is presented in the lower panel of Fig. 6.6. It shows that the narrowing of the BF with increasing centrality is present in all p_T bins. Our results demonstrate that the BF becomes narrow with increasing p_T at all given centrality bins, and in more central collisions at all given p_T bins. The width of BF depends on both centrality and p_T. The origins of these narrowing and their possible connections should provide more insight into the particle production dynamics in relativistic heavy ion collisions.

6.3 Charge correlation and fluctuation

Balance function measures the correlation of balancing charge, and it can be related to charge correlation and fluctuation.

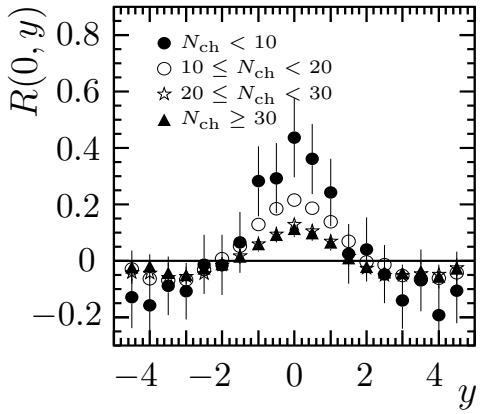

Figure 6.17: The 2-particle correlation function $R(0, y)$ as function of y for different multiplicities in $p + p$ collision at $\sqrt{s_{NN}} = 200$ GeV.

Charge balance function measures the correlation length between oppositely charged particles, and it can be related to standard two-particle correlation function [**?**]. For comparison we calculate the standard two-particle correlation function of oppositely charged particles

$$R^{+-}(y_1, y_2) = \frac{1}{2}[\frac{\rho^{(2)}(y_1^+, y_2^-)}{\rho^{(1)}(y_1^+)\rho^{(1)}(y_2^-)} + \frac{\rho^{(2)}(y_1^-, y_2^+)}{\rho^{(1)}(y_1^-)\rho^{(1)}(y_2^+)}] - 1 \tag{6.1}$$

for different multiplicities in $p + p$ collision at $\sqrt{s_{NN}} = 200$ GeV, for $y_1 = 0$, $y_2 = y$.

The results plotted in Fig. 6.17 show that the width of R is consistent with being independent of multiplicity. A possible explanation of the width of R is cluster decay. Comparing with the definition of balance function, Eq. 2.9, we see that it is the difference between the correlations of opposite- and like-charged particles that shows a clear multiplicity dependence, which is unrelated with cluster decay and is mainly due to the string fragmentation mechanism implemented in PYTHIA model.

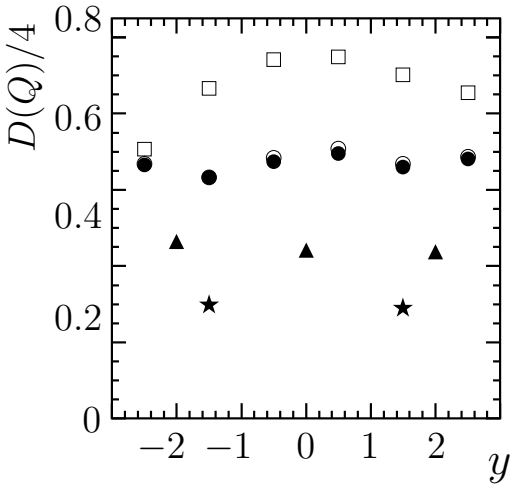

Figure 6.18: $D(Q)/4$ versus the position of a rapidity window of size $Y_{\rm w} = 1$ (circles), 2 (triangles), and 3 (stars). Open circles and open squares are, respectively, $D(Q)/4$ under the same transverse momentum and azimuthal angle cuts as used by STAR ($p_T > 0.1$ GeV/c) and PHENIX ($p_T > 0.2$ GeV/c and $\Delta\phi = \pi/2$).

Since the charge fluctuation $D(Q)$ defined in Eq. 2.12 is related to BF as Eq. 2.13, it is interesting to see how the charge fluctuation changes with position and size of a rapidity window. For this purpose, $D(Q)/4$ is presented in Figure 6.18 for different positions and sizes of a rapidity window. The results confirm that for the given window size the measured charge fluctuation is independent of the position of that window [**?**], in agreement with boost invariance of the BF. The data also show that the smaller the rapidity window the larger the fluctuation. So it is necessary to give the exact size of the rapidity region when the fluctuation is treated quantitatively [**?**, **?**].

As has been demonstrated in [**?**], $D(Q)$ also depends on the acceptance in transverse momentum and/or azimuthal angle. $D(Q)/4$ under the same cuts as used by STAR ($p_T > 0.1$ GeV/c) and PHENIX ($p_T > 0.2$ GeV/c and $\Delta\phi = \pi/2$) with $Y_{\rm w} = 1.0$ is

presented in Figure 6.18 as open points. The cut used by STAR has little influence on the result, while those used by PHENIX destroy the boost invariance of $D(Q)$. These results show that a limited acceptance can destroy the boost invariance of charge fluctuations and the effect is the larger the larger the percentage of particles lost.

6.4 Summary

We study the longitudinal property of boost invariance for charge balance function (BF) in hadron-hadron and nuclear-nuclear collisions.

In π^+p and K^+p collisions from NA22/EHS at $\sqrt{s_{NN}} = 22$ GeV, in contrast with signal particle density distribution, the BF is found to be invariant under longitudinal boost over the whole rapidity range of produced particles ($-5 < y < 5$), i.e., the ratio of $B(\delta y|y_{\rm w})$ to $(1 - \delta y/|y_{\rm w}|)$ is independent of the observed window, $|y_w|$, and corresponds to the BF of the whole rapidity range. Such longitudinal property is also observed in Au + Au collisions from STAR/RHIC at $\sqrt{s_{NN}} = 200$ GeV within a relatively wide pseudorapidity coverage ($|\eta| < 1.3$). Furthermore, we find that this scaling property has little dependence on p_T and centrality. In order to compare with experimental data, we also systematically study the longitudinal boost invariance of the BF and its p_T dependence for $p + p$ and Au + Au collisions using the PYTHIA and the AMPT Monte Carlo models. It shows that the BF is boost invariant in both hadron-hadron and nuclear interactions, in contrast to the single-particle density. As expected, this boost invariance of the BF results that the BF properly scaled by window size is independent of the window and corresponds to the BF of the whole pseudorapidity range.

Therefore, the BF can be considered as a good measurement which free from the restriction of finite longitudinal acceptance, i.e, the scaled BF, $B_s(\delta\eta)$, can be quantitively compared from different experiments with different pseudorapidity coverages. And since the BF measures how the conserved electric charge compensate in the phase space, the longitudinal property of boost invariance of BF means that production of charged particles are constrained by charge balance, and it is essentially the same in any

longitudinally-Lorentz- transformed frame.

It is argued that the width of charge balance function, $< \Delta y >$ ($< \Delta \eta >$), can be considered as a probe of late hadronization, we measure it in both hadron-hadron and nuclear-nuclear collisions.

In $\pi^+ p$ and $K^+ p$ collisions from NA22/EHS at $\sqrt{s_{NN}} = 22$ GeV, where no QGP phase space is expected, $< \Delta y >$ is found to be narrower as multiplicity increasing. To investigate this trivial effect, we studied $< \Delta y >$ in $p + p$ collisions at $\sqrt{s_{NN}} = 22$, 64, 130, 200 GeV using PYTHIA Monte-Carlo generator. The result shows that the width of BF first decreases with increasing multiplicity, and it changes little when multiplicity is about larger than 20. When the same size of observation window ($Y_{\rm w}$) is used, the width of BF is independent of colliding energy, which is consistent with expectation of instantaneous hadronization in hadron-hadron collisions. Also, $< \Delta y >$ is found sensitive to the size of observed windows, and it is consistent with charge correlation and fluctuation. In Au + Au collisions from STAR/RHIC at $\sqrt{s_{NN}} = 200$ GeV, $< \Delta y >$ decreases with increasing transverse momentum and increasing centrality. The origin of these narrowings is associated with transverse radial flow and their possible connections should provide more insight into the particle production dynamics in relativistic heavy ion collisions.

CHAPTER 7

Outlook

Presentations and publication List

Presentations

1. Study of the Number of Quark Scaling of v_2 at High Transverse Momentum (oral)
   APS April Meeting 2010, Washington DC, February 13-17, 2010.

2. Event Anisotropy at STAR (oral)
   RHIC & AGS Annual Users' Meeting, New York, USA, July 7-11, 2009.

3. PID v2 and v4 in Au+Au collisions at 200 GeV at RHIC (poster)
   Quark Matter 2009, Knoxville, TN, March 29 - April 4, 2009.

4. PID v2 and v4 in Au+Au collisions at 200 GeV at RHIC (oral)
   Winter Workshop on Nuclear Dynamics, Big Sky, Montana, USA, February 1-8, 2009.

5. Relative v_2 fluctuation in High-Energy Nuclear Collisions (poster)
   Quark Matter 2008, Jaipur, India, Feb. 4-10, 2008.

6. Longitudinal scaling property of the charge balance function in in Au+Au collisions at $\sqrt{s_{NN}} = 200$ GeV (poster)
   Quark Matter 2008, Jaipur, India, Feb. 4-10, 2008.

7. Boost-invariance and multiplicity dependence of charge balance function in π^+p and K^+p collisions at $\sqrt{s_{NN}}$ =22 GeV (oral)
   XXXV International Symposium on Multiparticle Dynamics, Czechoslovakia, August 9-15, 2005.

8. The property of Charge Balance Function (oral)
   The 9th Particle Physics Conference, Chongqing, China, May 9-13, 2005.

Publication list

1. **N. Li**, Z. M. Li, Y. F. Wu. "Longitudinal boost invariance of the charge balance function in hadron-hadron and nucleus-nucleus collisions", *Phys. Rev. C*, **80** 064910, 2009.

2. Yanping Huang, **N. Li**, Jiaxin Du, Zhiming Li and Yuanfang Wu. "Two-particle azimuthal angle correlations and azimuthal charge balance function in relativistic heavy ion collisions", *Phys. Rev C*, **79** 054912, 2009.

3. J. Du, **N. Li**, and L. Liu. "Narrowing of the charge balance function and hadronization time in relativistic heavy-ion collisions", *Phys. Rev C*, **75** 021903, 2007.

4. A. Feng, **N. Li**, J. Fu and Y. Wu. "Rapidity dependence of charge fluctuations and correlations in hadronic nuclear collisions", *International Journal of Modern Physics A*, **22** 2909, 2007.

5. Li Zhiming, **Li Na**, Liu Lianshou and Wu yuanfang. "Pseudorapidity and transverse momentum dependence of charge balance in Au + Au collisions at $\sqrt{s_{NN}} =$ 200 GeV", *International Journal of Modern Physics E*, **16** 3347, 2007.

6. Du Jiaxin, **Li Na** and Liu Lianshou. "On the relation between the width of charge balance function and hadronization time in relativistic heavy ion collision", *International Journal of Modern Physics E*, **16** 3355, 2007.

7. M.R. Atayan et al, (EHS/NA22 Collaboration). "Boost invariance and multiplicity dependence of the charge balance function in π^+p and K^+p collisions at $\sqrt{s_{NN}} =$ 22 GeV", *Phys. Lett. B*, **637** 39, 2006.
   Primary authors: **Na Li**, Yuanfang.Wu, Lianshou Liu.

8. **N. Li** and Y. Wu. "Boost Invariance and Multiplicity Dependence of the Charge Balance Function in π^+p and K^+p collisions at 22 GeV", *AIP Conf. Proc.* **828** 113, 2006.

9. B. I. Abelev *et al.*, STAR Collaboration. "Longitudinal scaling property of the charge balance function in in Au + Au collisions at $\sqrt{s_{NN}} = 200$ GeV",

Primary authors: **Na Li**, Zhiming Li and Yuanfang Wu.

Submitted to Phys. Lett. B.

10. B. I. Abelev *et al.*, STAR Collaboration. "The breaking of number of constituent quark scaling at high p_T in Au+Au collisions at $\sqrt{s_{NN}} = 200$ GeV",
Primary authors: D. Gangadharan, **N. Li**, S.S. Shi, A.H. Tang, Y.F. Wu.
STAR internal review